Thermodynamic Studies of Phase Transitions and Emerging Orders in Unconventional Superconductors

by

Xu Luo

B. S. Wuhan University, June 2009

Sc. M. Brown University, May 2011

A dissertation submitted in partial fulfillment of the requirements for the Degree of Doctor of Philosophy in the Department of Physics at Brown University

Providence, Rhode Island

May 2015

Abstract of "Thermodynamic Studies of Phase Transitions and Emerging Orders in Unconventional Superconductors." by Xu Luo, Ph.D., Brown University, May 2015

The nematic phase transition in Fe-based superconductors (FeSCs) has been a topic under intensive investigation. So far it is commonly accepted that the structural transition from tetragonal (C_4) to orthorhombic (C_2) symmetry in FeSCs has an electronic nematic origin due to the unusual anisotropy in resistivity, optical conductivity and orbital occupancy observed above the structural transition. However, recent studies of (Ba, Eu)$Fe_2(As_{1-x}P_x)_2$ by magnetic torque measurements show the existence of a "true" nematic transition well above the commonly accepted structural/nematic transition .Controversies about this "true" nematic phase transition arise as residue strains or external applied fields are known to break C_4 symmetry and render the structural transition merely a crossover.

We performed high resolution AC micro-calorimetry and SQUID magnetometry measurements of $BaFe_2(As_{1-x}P_x)_2$ (x=0, 0.3) to investigate the various phase transitions and to explore the "true" nematic phase transition. The advantageous design of our membrane calorimeter allows us to perform high resolution studies of the thermodynamic phase transitions without any symmetry breaking fields. Our results suggest that there is not a second order "true" nematic phase transition in $BaFe_2(As_{1-x}P_x)_2$ even though the Ginzburg-Landau model used to fit the magnetic torque data indicates that the expected thermal anomaly should be within our experimental resolution.

In addition to the above, we present specific heat and magnetization studies of $Ba_{1-x}Na_xFe_2As_2$ in search of the recent discovered emergent reentrant C_2 to C_4 symmetry SDW transition in this series of compound. Our results indeed locate a new phase transition in $Ba_{0.74}Na_{0.26}Fe_2As_2$ at 45K. However, the absence of the conventional SDW transition at around 80K in our data leaves doubt about the exact nature of this new phase transition. We also systematically studied the effects of

heavy ion irradiation (HII) on the anisotropy of $YBa_2Cu_3O_{7-\delta}$ single crystals by angular rotation specific heat measurements. We found that the anisotropy of $YBa_2Cu_3O_{7-\delta}$ decreases by approximately a factor of two with an irradiation dose of 6T (matching field). The dependence of anisotropy on irradiation doses agrees well with the prediction from a simple phenomenological model that takes into account the anisotropic scattering caused by columnar defects created in HII.

This dissertation by Xu Luo is accepted in its present form by the Department of Physics as satisfying the dissertation requirement for the degree of Doctor of Philosophy.

Date_____ _____
Prof. Xinsheng S. Ling, Advisor

Date_____ _____
Dr. Ulrich Welp, Co-Advisor

Recommended to the Graduate Council

Date_____ _____
Prof. John Marston, Reader

Date_____ _____
Prof. Vesna Mitrovic, Reader

Approved by the Graduate Council

Date_____ _____
Prof. Peter M. Weber, Dean of the Graduate School

Acknowledgements

First of all, I would like to thank my advisor at Argonne National Lab, Dr. Ulrich Welp, who introduced me to the field of superconductivity and taught me the art of AC specific heat measurements. Without his guidance and advice on both experiments and physics, the work that is presented in this thesis would have not been possible. His persistence and rigorousness towards research have inspired me to always think deeper and work harder. I would also like to thank Prof. Wai Kwok for giving me this great opportunity to work at Argonne and providing support for my research both financially and academically. I deeply appreciate the many mind opening talks I have had with Prof. Kwok about my career development and goals.

I would like to thank my advisor at Brown, Prof. Sean Ling for giving me this great opportunity to work with Dr. Welp and Prof. Kwok at Argonne for my thesis. I deeply appreciate Prof. Ling's kind help and moral support during the course of my thesis research. I also wish to thank Prof. Brad Marston and Prof. Vesna Mitrovic for kindly serving on my dissertation committee and careful reading of this thesis.

I am grateful to have met so many enthusiastic and helpful colleagues at the superconductivity group at Argonne. Among them, I would especially like to thank Tim Benseman for his help and training in the fabrication of devices and instrumentation. Tim's extraordinary attention to detail and patience is something I would always want to learn. Many thanks to Maxime Leroux, Matt Smylie, Carlos Chaparro and Yonglei Wang for their helpful training and assistance on various aspects of experimental work. I also appreciate and cherish the fellowship of Yang Hao, Karen Kihlstrom and Mike Miszczak, with whom I have shared one of the most important and fruitful period of my life. I sincerely wish them all the best in their future careers.

I would also like to thank our collaborators: Bing Shen, Jared Allred, Daniel Bugaris, Dr. Helmut Claus and Dr. Ray Osborn for their assistance with sample growth and characterization and helpful scientific advice; Valentin Stanev and Vivek Mishra for providing theoretical support; Dr. Ralu Divan at CNM for training me on advanced wafer fabrication tools.

My friends and classmates at Brown have been a critical part of my graduate student life. I feel lucky to have met so many smart and caring peers and have shared with them many precious moments of my life. I deeply appreciate their friendship, without which my life at Brown would have been plain and unexciting.

Without the continual support, encouragement and love from my family, none of this would have been possible. Thank you Dad and Mom for always being there to support me.

Contents

List of Figures

List of Tables

Chapter 1

Introduction

1.1 History and Evolution of Superconductivity

Superconductivity was discovered in 1911 by H. Kamerlingh Onnes at University of Leiden [1]. It was found that the resistance of mercury (Hg) dropped abruptly to zero at around T*=4.2K (Fig 1.1(a)). It was obvious that the sample had undergone a transformation into a novel, as yet unknown, state characterized by zero electrical resistance. This phenomenon was named "Superconductivity".

All attempts to find at least traces of resistance in bulk superconductors were to no avail. On the basis of the sensitivity of modern equipment, one can argue that the resistivity of superconductors is zero, at least at the level of 10^{-24} Ω*cm, which is 15 orders of magnitude smaller than the resistance of high purity copper, the best normal conductor, at L^4He temperature [2]. The temperature of the transition from normal to superconducting state is called the critical temperature T_c. Shortly after the discovery, it was found that superconductivity can be destroyed not only by heating the sample to above T_c, but also by placing it in a relatively weak magnetic field. This field is defined as the thermodynamic critical field, H_c (Note that this only applies to type I superconductivity, which has only one critical field).

Ever since its discovery, superconductivity has been one of the most actively studied fields in condensed matter physics and has attracted immense experimental and theoretical efforts. More and more superconductors have been discovered in single elements, alloys, intermetallic compounds and oxides and still more are being discovered.

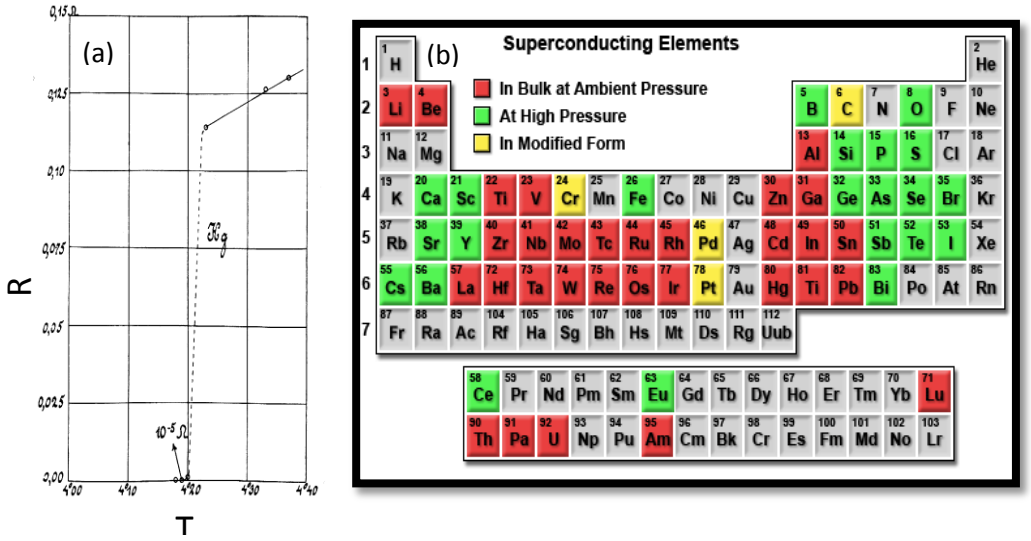

Fig 1.1 (a) Resistance versus temperature data of mercury made by Kamerlingh Onnes in his original paper [1] (b) Superconductivity in the periodic table [3].

A fact that can easily be overlooked is that superconductivity is not rare in nature. Almost half of the elements in the periodic table and hundreds of compounds have been found to be superconducting (Fig 1.1(b)). Fig 1.2 shows the milestones in the discovery of superconductors [4]. Among the elemental superconductors, Niobium (Nb) has the highest superconducting transition temperature, T_c, of 9.2 K. This record held for more than ten years, until the discovery of niobium nitride (NbN) which superconducts at 16 K. It took another thirty years for T_c to increase from 16 K in NbN to 23 K in niobium germanium (Nb_3Ge) [5]. It is worth mentioning that Nb_3Sn with a T_c of 18 K [6] has been used for making high field superconducting magnets due to high critical current density and capability of withstanding high magnetic fields [7].

Then a revolutionary breakthrough was made by Karl Muller and Johannes Bednorz in 1986 with their discovery of $La_{1-x}Ba_xCuO_4$ with a transition temperature over 30 K [8]. Nine months later, T_c rose to 93 K in $YBa_2Cu_3O_{7-\delta}$ discovered by M. K. Wu, C. W. Chu et al [9]. T_c now exceeds the boiling point of liquid nitrogen. T_c continued to dramatically increase over the next several years.

In 1988, $Bi_2Sr_2Ca_nCu_{n+1}O_{2n+6-\delta}$ was discovered to be superconducting at 95 K when n = 1 [10] and 105K when n=2 [10]. Later, thallium based cuprates $Tl_2Ba_2Ca_nCu_{n+1}O_{2n+6-\delta}$ (n=2) was discovered to have a T_c of 120 K [11]. In 1993, $HgBa_2Ca_{n-1}Cu_nO_{2n+2+\delta}$ (n=3) was found with T_c as high as 133 K [12] and with Tl substitution on Hg sites, T_c rose to 138 K which is the current record of highest T_c at ambient pressure [13]. This group of materials is named High-T_c superconductors due to their extremely high critical temperatures (above LN_2 temperature). Since they all share the same CuO_2 planes in their crystal structures which are commonly believed to be responsible for superconductivity, they are also known as High-T_c cuprates.

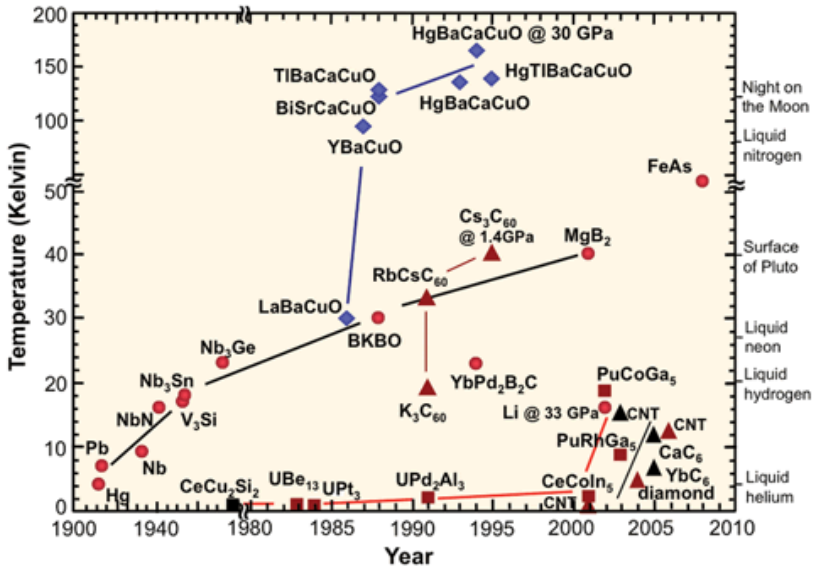

Fig 1.2 Evolution of the critical temperatures of superconductors [4].

Another breakthrough in the discovery of superconductivity was made by Hideo Hosono and co-workers in 2008 [14] with the discovery of superconductivity at 26K in $LaFeAsO_{0.9}F_{0.1}$. Soon after this discovery, the transition temperature has been raised to above 40 K by chemical substitutions with the highest Tc reported so far at 55K in $SmFeAsO_{1-x}$ [15] and $Gd_{1-x}Th_xFeAsO$ [16]. This group of materials is named Fe-based superconductors (FeSCs) due to the presence and importance of Fe_2X_2 (X=As, Se, etc.) layers in their crystal structures.

1.2 Fe-based Superconductors

The crystal structures of the 5 most common FeSC families [17] are shown in Fig 1.3. It can be seen that they all share a common layered structure based upon a planar layer of Fe atoms joined by tetrahedrally coordinated pnictogen (P, As) or chalcogen (S, Se, Te) anions arranged in a stacked sequence separated by alkali, alkaline earth or rare earth and oxygen/fluorine "blocking layers". It is widely believed that the high-T_c superconductivity originates within these iron containing layers, similar to the case of cuprates where the CuO_2 planes are thought to be responsible for superconductivity. However, there are three key differences between these two systems: (1) the arrangement of pnicitogen/chalcogen anions above and below the planar iron layer as opposed to the planar copper-oxygen structure of the cuprates; (2) the ability to dope directly into the active pairing layer in FeSCs; and (3) the metallic nature of the parent compound in Fe-based superconductor as opposed to the insulating nature of the parent compound in cuprates. It is these traits, together with the similar interplay of magnetism and superconductivity that mark FeSCs and cuprates as distinct but closely related superconducting families.

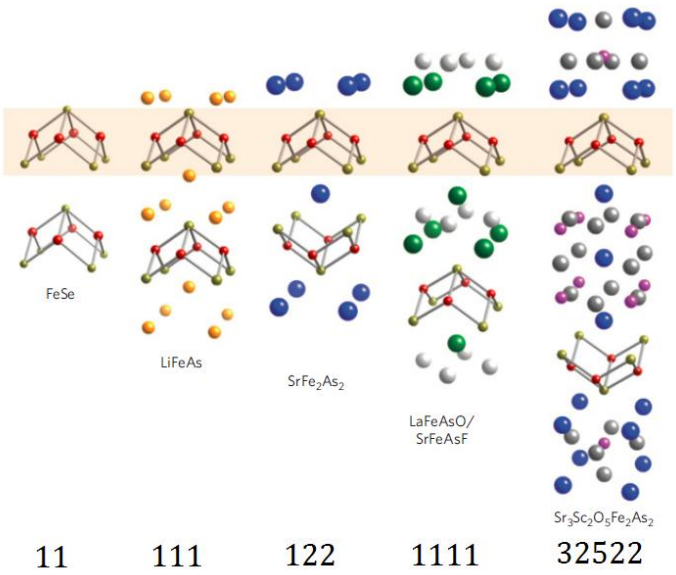

Fig 1.3 The five main structural families of Fe-based superconductors [17]

The phase diagram of FeSCs is in fact strikingly similar to many other classes of unconventional superconductors (cuprates, organics, heavy-fermion SCs), all believed to have unconventional (non-phonon-mediated) pairing mechanisms. An antiferromagnetic parent state is suppressed by either chemical doping [18-20] or applied external pressure [21-25] and superconductivity arises. Superconductivity reaches its maximum approximately at the annihilation of antiferromagnetism (AFM). A compilation of the experimental doping phase diagrams for one of the most studied FeSC systems, Ba-based "122" system, is shown is Fig 1.4 [17].

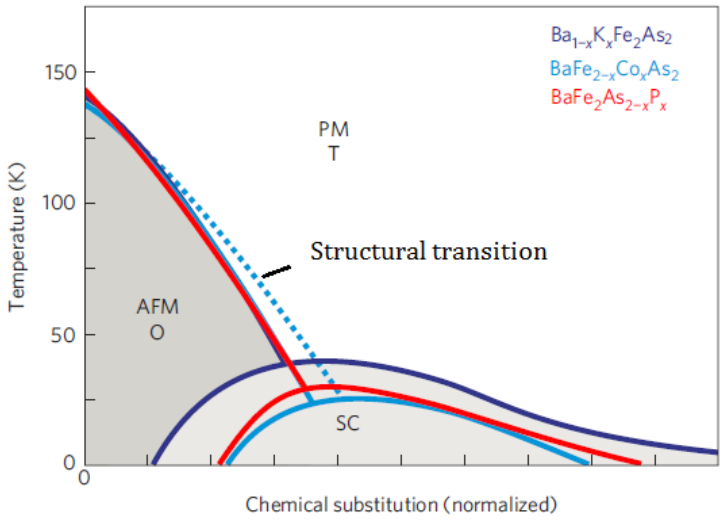

Fig 1.4 Normalized Temperature-doping phase diagram of Ba "122" system [17].

The electronic band structures of FeSCs have been calculated using local density approximation [26] and an example band structure is given in Fig 1.5 [27]. It was shown that the electronic properties are dominated by five Fe d-states at the Fermi energy, with a Fermi surface consisting of three cylindrical hole pockets at the center and two cylindrical electron pockets at the corner of the Brillouin Zone (BZ). The results agree well with angle-resolved photoemission spectroscopy (ARPES) [28-30] and quantum oscillation measurements [31, 32].

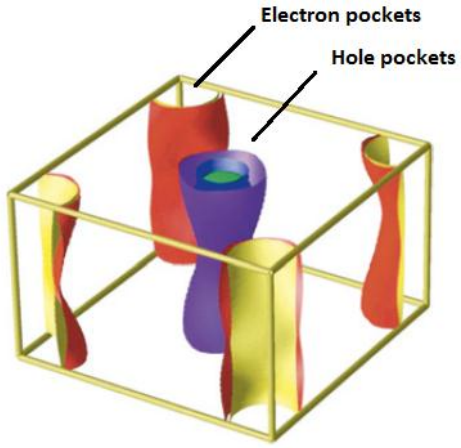

Fig 1.5 Fermi surfaces of $Ba(Fe_{0.9}Co_{0.1})_2As_2$ calculated via density functional theory [27].

The pairing symmetry in FeSCs is a topic of hot debate. While early experiments point to a fully gaped order parameter (OP) consistent with a fully symmetric s-wave symmetry [30], the OP symmetry of FeSCs was in fact predicted to have s-wave symmetry, but with a sign change that occurs between different bands in the complex multi-band electronic structure. This is the so-called "$s\pm$"symmetry [27, 33]. On the experimental side, NMR experiments on several members of the Fe-based superconductors have positively identified the parity of the superconducting state as singlet [34, 35], implying an even OP symmetry (i.e. s-wave, d-wave, etc.). Determining the nature of the orbital OP symmetry, however, is much more complex and is currently the focus of most research. Due to the multi-band nature of FeSCs and their nesting properties, anisotropic s- and d-wave states are nearly degenerate [36], making it difficult to identify the underlying symmetry even if experiments determine the presence of nodes in the gap symmetry. Phase sensitive experiments [37, 38] that have been done so far favor $s\pm$ symmetry in the FeSCs, but definitive experiments on more materials are needed to conclusively settle the case. Pairing mechanisms in FeSCs are not clear. Early calculations have shown that FeSCs have poor electron-phonon couplings and phonons alone cannot explain the high critical temperatures

observed [39]. Since superconductivity sits so close to antiferromagnetism (AFM), it is commonly believed that AFM fluctuations might play a key role in the pairing of FeSCs.

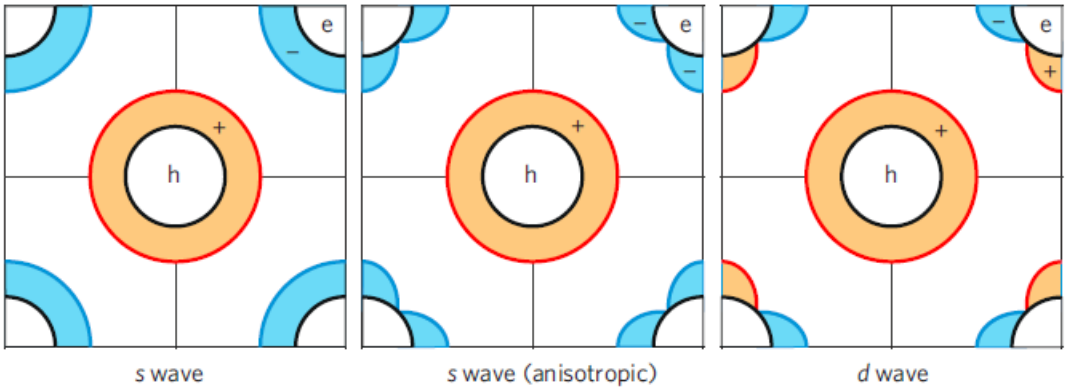

Fig 1.6 Proposed multi-band pairing gap symmetries (Note that multiple hole and electron pockets have been reduced to one each for simplicity). Left: $s\pm$ symmetry with isotropic gaps; Middle: $s\pm$ symmetry with accidental nodes on electron pockets; Right: d-wave symmetry. From Ref [17].

1.3 Nematicity in Fe-based superconductors

The role of AFM to Fe-based superconductors has been discussed extensively in the previous sections. However, another important fact that makes FeSCs so unique is that the AFM transition is almost always preceded by or coincident with a structural transition [40-42] (e.g. the dashed line in Fig 1.3) from tetragonal to orthorhombic symmetry (see Fig 1.7).

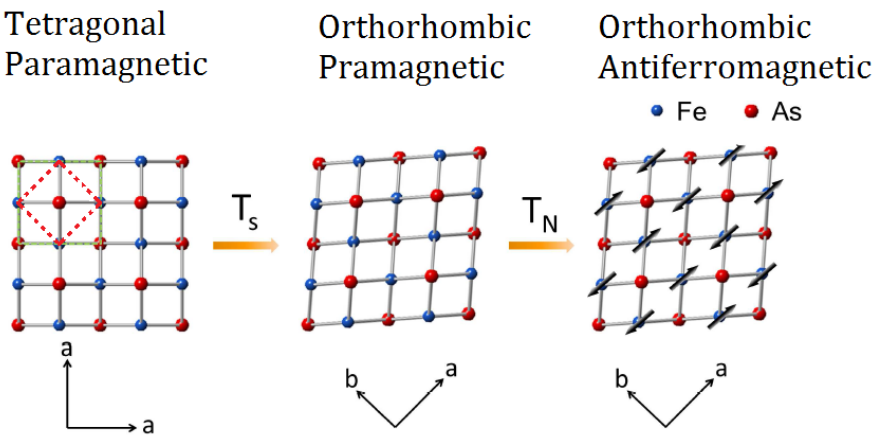

Fig 1.7 Schematics showing the structural and AFM transitions in doped (Co or P) $BaFe_2As_2$ expressed as single FeAs layer. The green and red dashed lines mark the 2-Fe and 1-Fe unit cell. From Ref [43].

The interplay of magnetic and structural transitions generates rich physics. Although a conventional phonon driven mechanism of the structural transition cannot be ruled out completely, this transition has generally been considered as a manifestation of electronic nematic order [44], which has also been inferred from the unusual anisotropy in resistivity [45, 46] (Fig 1.8), optical conductivity [47] and orbital occupancy [48] (Fig 1.9) observed at temperatures above the structural transition.

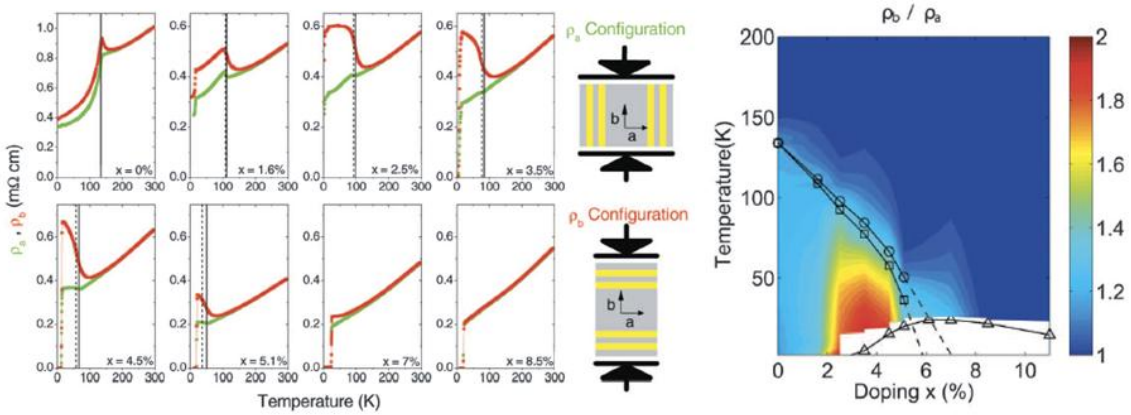

Fig 1.8 In-plane resistivity anisotropy measurements of $Ba(Fe_{1-x}Co_x)_2As_2$. The anisotropy value of ~2 cannot be explained by a conventional structural distortion in the orthorhombic phase. From Ref [45].

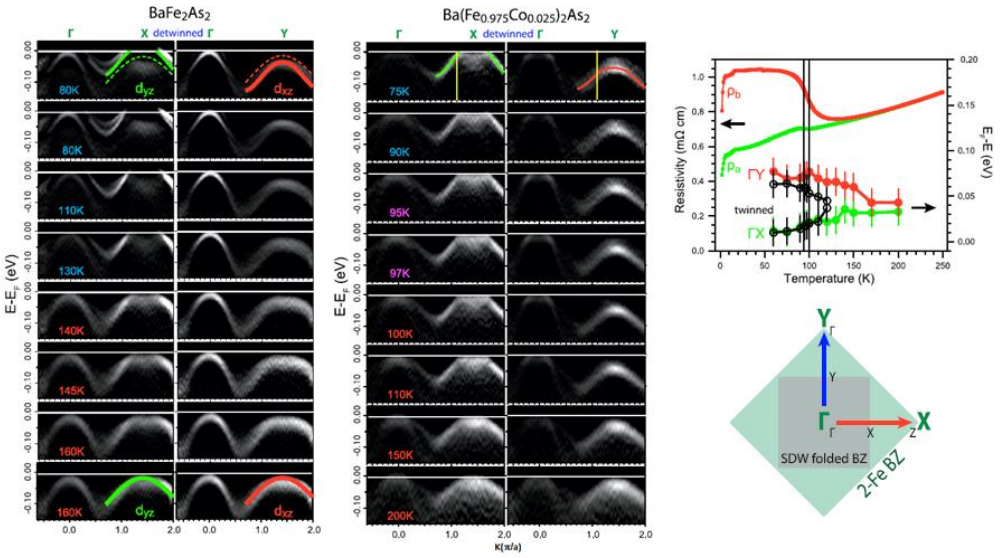

Fig 1.9 Temperature dependence of anisotropic band dispersion in $BaFe_2As_2$ and $Ba(Fe_{0.975}Co_{0.025})_2As_2$ along Γ-X and Γ-Y measured by ARPES. From Ref [48].

The origin of nematic order has been ascribed to either a spontaneous ferro-orbital order with unequal occupations between the Fe d_{xz} and d_{yz} orbitals [49-53] or an Ising spin-nematic order [54-58] where the Z_2 symmetry between the two possible SDW ordering wave vectors $\mathbf{Q_1} = (0,\ \pi)$ and $\mathbf{Q_2} = (\pi,\ 0)$ in the 1-Fe Brillouin Zone (BZ) is broken before the O(3) spin rotational symmetry [57] (Fig 1.10).

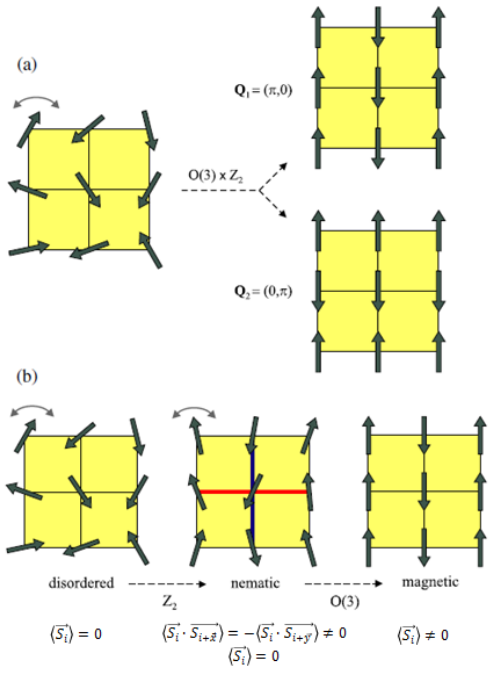

Fig 1.10 Schematic showing the spin-nematic mechanisms of the structural transition. From Ref [57]

Regardless of the exact microscopic origin of nematicity, a phenomenological treatment of the problem based on Ginzburg-Landau (GL) theory by taking into account magnetostructural coupling yields a good description of the order of the AFM and structural transitions and the possibility of a tricritical point in the phase diagram [44, 59, 60] (Fig 1.11)

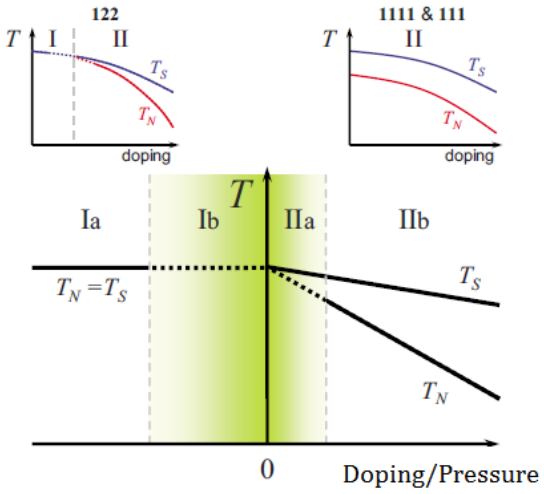

Fig 1.11 Schematic T-doping diagrams for structural and magnetic phase transitions (top panels) and general phase diagram determined from GL theory (bottom panel); Dashed and solid lines indicate 1st and 2nd order phase transitions. From Ref [60].

1.4 Research Topics and Thesis Layout

Recent magnetic torque measurements on $BaFe_2(As_{1-x}P_x)_2$ [61] and $EuFe_2(As_{1-x}P_x)_2$ [62] single crystals under in-plane magnetic field rotation revealed the onset of two fold oscillations, which break the tetragonal symmetry at a temperature T^* well above (>30K) the commonly accepted nematic/structural transition at T_S (Fig 1.12). These results were interpreted [61, 62] as signature of a "true" 2nd order nematic phase transition at T^* leading from the high-temperature tetragonal phase to a low-temperature phase with C_2-symmetry whereas the conventional structural transition at T_s ceases to be a true phase transition but is regarded as a meta-nematic transition. This "true" transition at T^* is found to persist even for doping levels in the nonmagnetic superconducting regime, which dramatically changes the phase diagrams of $BaFe_2(As_{1-x}P_x)_2$ and $EuFe_2(As_{1-x}P_x)_2$. For instance, consideration needs to be given to the number of degrees of freedom required for stabilizing a nematic state over such a wide temperature range [63] in a macroscopically tetragonal lattice.

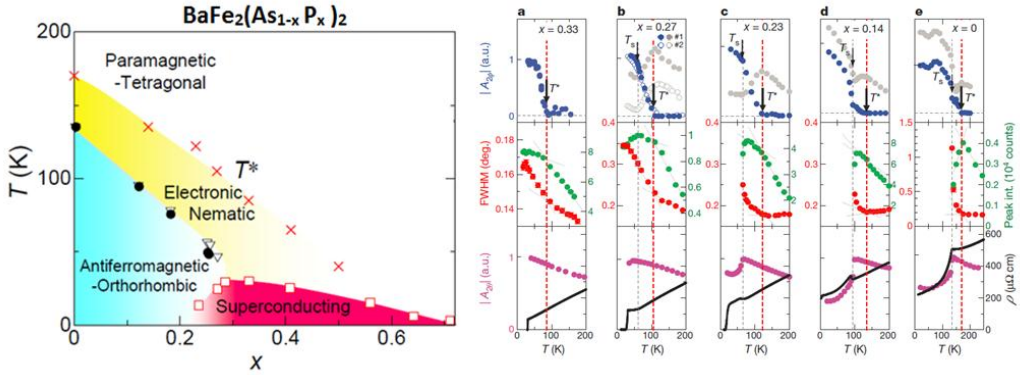

Fig 1.12 T-doping phase diagram after addition of the true nematic phase transition line (left); Measurement data from magnetic torque, high-resolution XRD and resistivity with red lines marking the true nematic phase transition temperatures for five different doping levels of $BaFe_2(As_{1-x}P_x)_2$. From Ref [61].

Measurements of the strain dependent resistivity anisotropy [46] or of the shear elastic constants [64] of $BaFe_2As_2$ (parent compound) do not yield evidence for additional phase transitions above the usual structural transition. A recent STM/STS study on NaFeAs single crystals [65] revealed the persistence of local electronic nematicity up to temperatures of almost twice T_S. In this case, residual strains in the sample in conjunction with a large nematic susceptibility were considered as possible origin of such symmetry breaking. Similarly, recent inelastic neutron scattering experiments shows change in the low energy spin excitations in uniaxially strained $BaFe_{2-x}T_xAs_2$ (T=Co or Ni) from four fold to two fold symmetry at temperatures (T^*) corresponding to the onset of in-plane resistivity anisotropy observed previously [66]. However, the authors also emphasized the effects from the uniaxial strain they applied which rendered the structural transition at T_S a crossover and T^* only marks a typical range of nematic fluctuations [66]. Nevertheless, magnetic torque is directly related to the spin nematic order parameter [57] possibly facilitating the observation of a nematic phase transition. Thus, the question whether the phenomena at T^* represent a 2^{nd} order phase transition, a cross-over associated with the onset of sizable short-range correlations and fluctuations, or spurious effects due to frozen-in or applied strains remains unresolved. Given the controversies of the true nematic transition, we propose to study the phase transitions in $BaFe_2(As_{1-x}P_x)_2$ by high resolution ac microcalorimetry and SQUID magnetometry. If such a phase transition does exist, we should be able to see it in the thermal channel, i.e. specific heat.

Another closely related topic of interest is the reentrant C_4 symmetric antiferromagnetic spin density wave (SDW) transition in underdoped $Ba_{1-x}Na_xFe_2As_2$ (x=0.24) that was recently

observed by neutron scattering experiments [67] (Fig 1.13). High resolution specific heat measurements in this case can also be used to find out about the existence of such a phase transition and to find the transition temperatures with high accuracy.

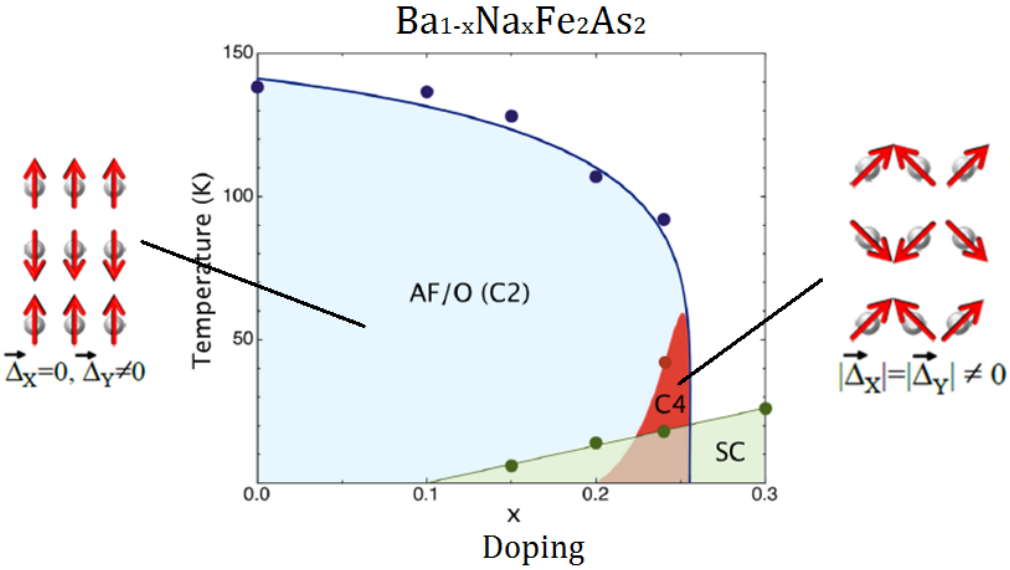

Fig 1.13 Schematic showing the phase diagram of $Ba_{1-x}Na_xFe_2As_2$ with the reentrant C_4 symmetry phase plotted as the red region. Different AFM ordering configurations for the C_2 and C_4 phases are shown in the left and right panels. From Ref [67].

Recently, the discovery of a large reduction in the thermodynamic anisotropy of a few iron based superconductors by heavy ion irradiation has attracted great interest [68-70] (See Fig 1.14). While iron based superconductors are generally known as multi-band superconductors and temperature dependent anisotropies in FeSCs have been reported [69, 71]. The effects of heavy ion irradiation on a single band d-wave superconductor, such as YBCO, have not been studied yet. In this thesis, we used angular dependent specific heat measurements to systematically study the effects of heavy ion irradiation with different doses on the thermodynamic properties of YBCO, such as anisotropy, upper critical fields, critical temperatures, emerging phases, etc.

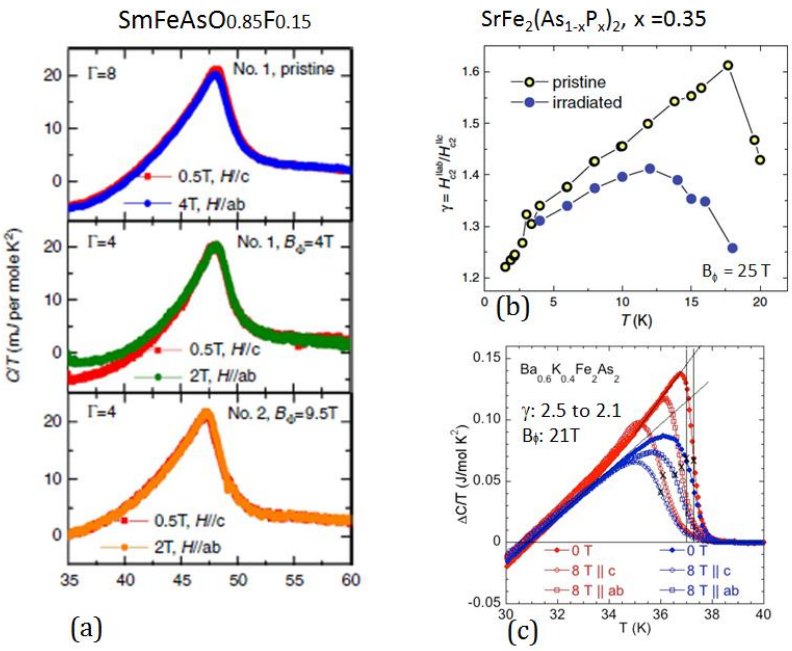

Fig 1.14 (a) anisotropy measurements of $SmFeAsO_{0.85}F_{0.15}$ after irradiation of B_Φ=4 T and 9.5 T [68]; (b) anisotropy of $SrFe_2(As_{1-x}P_x)_2$ (x=0.35) before and after irradiation of B_Φ =25 T [69]; (c) anisotropy of $Ba_{0.6}K_{0.4}Fe_2As_2$ measured by specific heat before and after an irradiation dose of B_Φ =21 T [70].

This thesis will be organized as follows:

In Chapter 2, I will give a general overview of the important advancements in superconductivity and discuss some of the fundamentals of superconductivity.

In Chapter 3, I will describe the experimental technique: membrane based high resolution AC Micro-calorimetry that was used to carry out the experimental studies of various thermodynamic properties and phase transitions of unconventional superconductors.

In Chapter 4, I will show and discuss in detail, the results from our study of the antiferromagnetic and nematic phase transitions in $BaFe_2(As_{1-x}P_x)_2$. Many of the things discussed can be found in a

recently published paper: X. Luo *et al*, Antiferromagnetic and nematic phase transitions in $BaFe_2(As_{1-x}P_x)_2$ studied by ac microcalorimetry and SQUID magnetometry, *Phys. Rev. B* 91, 094512 (2015).

In Chapter 5, I will show the results from our thermodynamic studies of the exotic reentrant C_2 to C_4 SDW transition in underdoped $Ba_{1-x}Na_xFe_2As_2$ for several different doping levels; I will also show the results from our study of the effects of heavy ion irradiation on the thermodynamic properties, especially anisotropy, of high purity detwinned $YBa_2Cu_3O_{7-\delta}$ single crystals.

In Chapter 6, I will summarize the work in this thesis and give some important conclusions that can be drawn from it.

Chapter 2

Overview of Superconductivity

2.1 Meissner effect

The discovery of Meissner effect in 1933 was another mile stone in the study of superconductivity [72]. It was then people start to realize that superconductor is not merely an ideal conductor with zero resistance. Instead, superconductors demonstrate perfect diamagnetism when the applied field is lower than H_c (H_{c1} for type II superconductors). The argument is straightforward. For an ideal conductor that is zero field cooled, applying an external field will induce a surface current according to Lenz's law which generates a magnetic field in the direction opposite to that of the external field. Therefore, the total field in the interior of the specimen is zero. Written in terms of Maxwell equations:

$$\nabla \times E = -\frac{1}{c}\frac{\partial B}{\partial t} \tag{2.1}$$

In an ideal conductor, $\rho = 0$ and $E = j\rho = 0$. It follows that $B = const$ and considering $B = 0$ before applying the external field, we arrive at $B = 0$ also after the field is applied. However, if we reverse the sequence of cooling the sample below T_c and applying an external field, we will see that there would be a difference in the results. Since we apply a field when the sample is above T_c, i.e. in the resistive state, the magnetic field will penetrate into the interior of the sample. Then when the sample is cooled below T_c into the zero resistance state, the field remains in it because the magnetic field does not change with time in an ideal conductor (see Fig

2.1(a)). However, this is not what Meissner and Ochsenfeld observed. Instead, they found the magnetic field inside a superconductor is always zero no matter which sequence was employed, as shown in Fig. 2.1 (b). Perfect diamagnetism in superconductors cannot be explained by zero resistivity and it is one of the intrinsic properties of the superconductors.

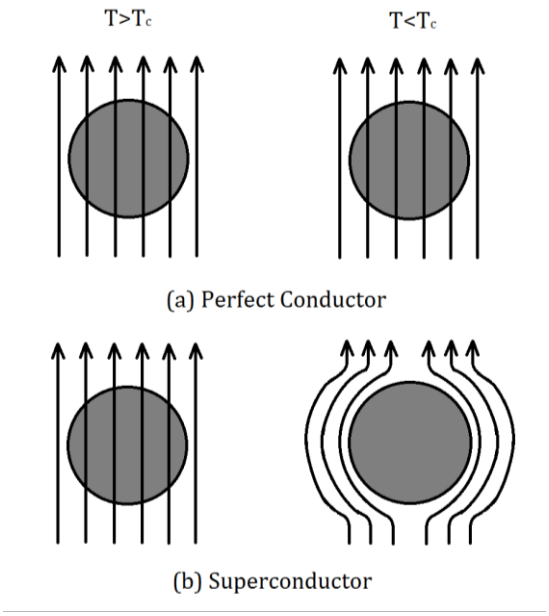

Fig 2.1 (a) Magnetic induction inside an ideal conductor when field cooled from above T_c

(b) Magnetic induction inside a superconductor when field cooled from above T_c

2.2 Type I and Type II superconductivity

We have already learned that the interior of the superconductor cannot be penetrated by a weak magnetic field (Meissner effect). When the magnetic field becomes large, superconductivity breaks down. Superconductivity can be divided into two groups depending on how this breakdown occurs. In type I superconductors, superconductivity is abruptly destroyed via a first order phase transition when the strength of the applied field rises above the critical field H_c. The dependence of magnetization and magnetic induction on applied field of type I superconductors are plotted in Fig 2.2 (a). Type I superconductivity is normally found in pure metals, e.g. Al, Pb

and Hg. The only alloy known up to now which exhibits type I superconductivity is $TaSi_2$ [73]. Depending on the demagnetization factor, one may obtain an intermediate state in type I superconductors which are characterized by macroscopic phase separation of superconducting and non-superconducting domains in the bulk of the superconductor [74].

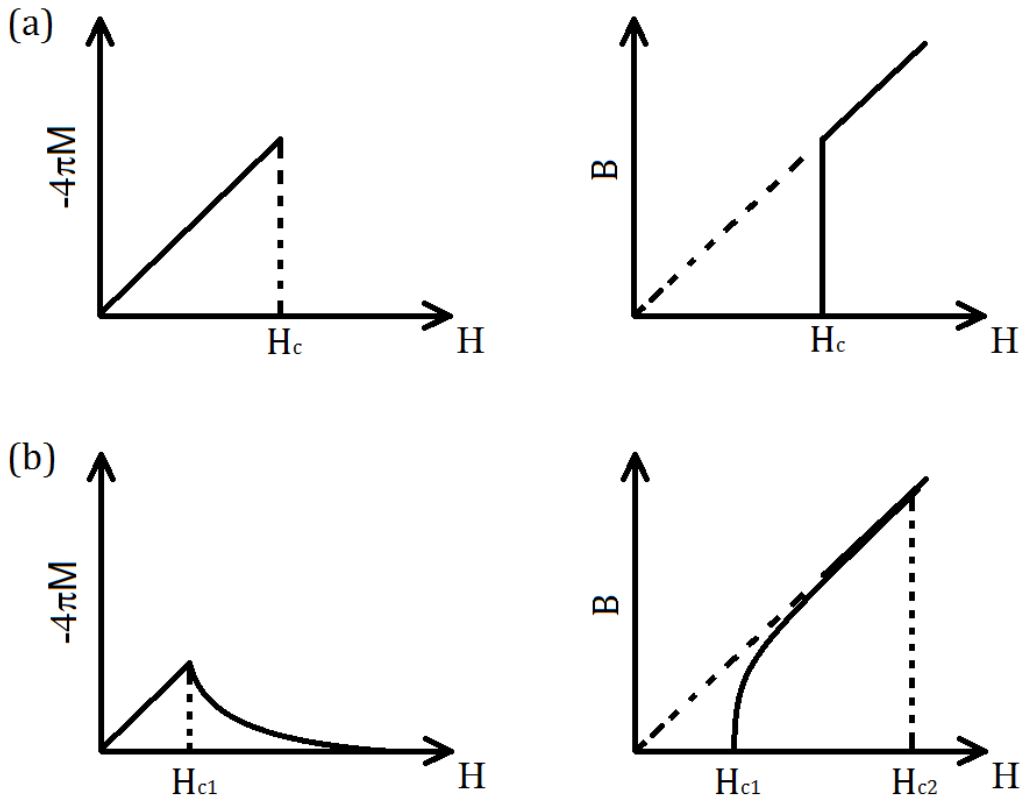

Fig 2.2 (a) Magnetization (left) and Magnetic induction (right) versus applied field for type I superconductor; (b) Magnetization (left) and Magnetic induction (right) versus applied field for type II superconductor.

The transition of type II superconductors from superconducting in externally applied magnetic fields is more gradual comparing with type I superconductors. The superconductor will exclude completely the external field up to the lower critical field (H_{c1}). The external fields then penetrate the material in the form of quantized magnetic flux lines (vortices) forming a state called the vortex state (Shubnikov phase) [75]. In this state, the material remains superconducting outside of

these microscopic vortices. With an increasing applied magnetic field, the vortex density becomes too large and the entire material becomes non-superconducting at the upper critical field (H_{c2}). The dependence of magnetization and magnetic induction on applied field of type II superconductors are plotted in Fig 2.2 (b). As will be mentioned later in the text, the Ginzburg-Landau parameter κ which is defined as the ratio of the penetration depth λ to the coherence length ξ determines whether a superconductor is type I or type II. Type I superconductor has $\kappa < \frac{1}{\sqrt{2}}$ and type II superconductor has $\kappa > \frac{1}{\sqrt{2}}$. The H-T phase diagram for type I and type II superconductors are shown in Fig 2.3.

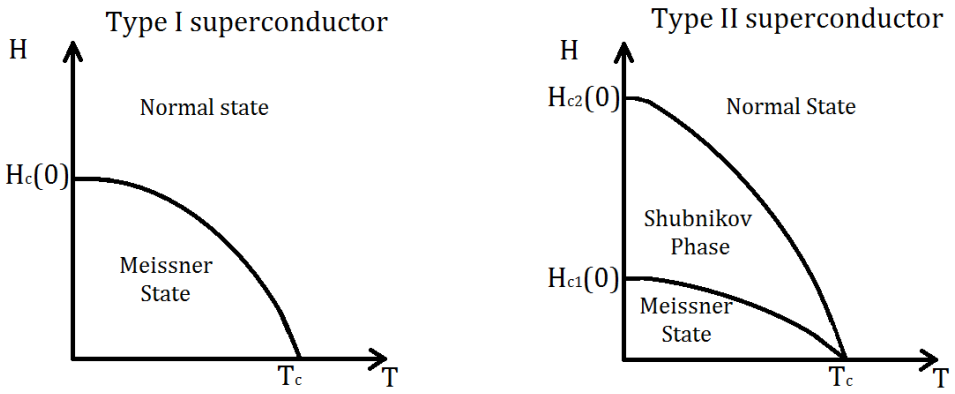

Fig 2.3 H-T phase diagram of type I (left) and type II (right) superconductors

2.3 Thermodynamics of Superconductors

Consider a long cylinder of a type I superconductor in a uniform longitudinal magnetic field H_0. We know that when $H_0 < H_c$, B is zero due to the Meissner effect. The magnetic moment per unit volume of the cylinder is then:

$$M = -H_0 / 4\pi \tag{2.2}$$

When a value dH_0 is added to the magnetic field H_0, an external source of magnetic field does a work on the superconductor, per unit volume, of:

$$-MdH_0 = H_0 dH_0 / 4\pi \tag{2.3}$$

When field changes from 0 to H_0, the work done by the field source is:

$$-\int_0^{H_0} MdH_0 = H_0^2 / 8\pi \tag{2.4}$$

This work is stored in the free energy of the superconductor placed in the field H_0. Thus, if the free energy density of a superconductor in zero magnetic field is F_{s0}, that of the superconductor in a finite magnetic field is:

$$F_{sH} = F_{s0} + H_0^2 / 8\pi \tag{2.5}$$

When the applied field reaches the thermodynamic critical field, i.e. $H_0 = H_c$, the free energy of the superconductor would be equal to that of the normal metal, thus:

$$F_n - F_{s0} = H_c^2 / 8\pi \tag{2.6}$$

We can see that the thermodynamic critical field is a measure of the extent to which the superconducting state is preferable to the normal state.

By taking the first derivative of the free energy with respect to temperature in equation (2.6), we can derive the entropy difference between the superconducting and normal states:

$$S_s - S_n = \frac{H_c}{4\pi}\left(\frac{\partial H_c}{\partial T}\right) \tag{2.7}$$

A few important conclusions can be drawn from (2.7)

(1) Since the entropy is zero at 0 *K* for both superconducting and normal states, the slope of H_c is also zero at 0 *K*. The slope of H_c is always negative from experiment results which means the entropy of the superconducting state is always lower than that of the normal state except for T = 0 *K* and T = T_c. A plot of the entropy of the superconducting and normal state is shown in Fig 2.4(a).

(2) Since $S_s = S_n$ at T = T_c, the transition at T = T_c does not involve latent heat and thus is a second order phase transition. On the other hand, all transitions at T<T_c from normal to superconducting state with a sufficiently strong applied magnetic field is accompanied by release of latent heat and thus are first order phase transitions.

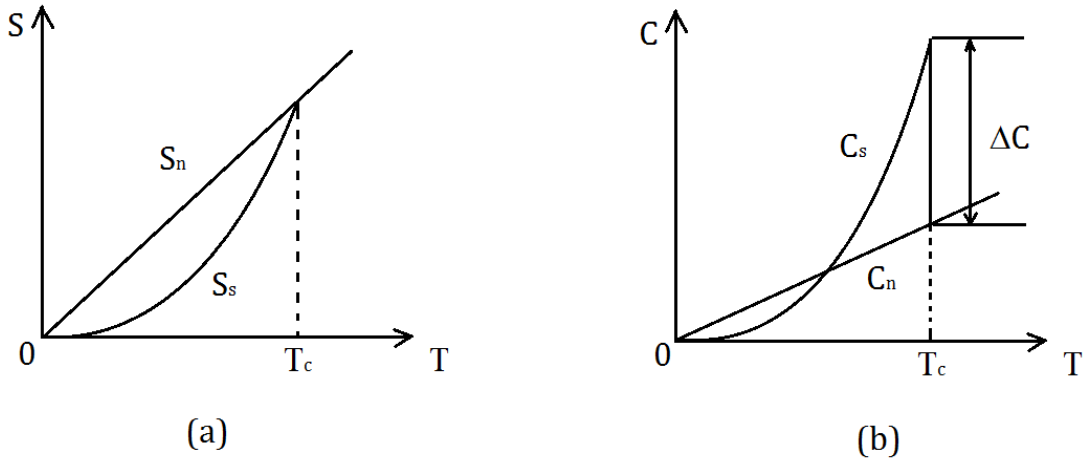

Fig 2.4 (a) Temperature dependence of the entropy of the superconducting state and normal state; (b) Temperature dependence of the specific heat of superconducting and normal states

The specific heat of matter can be defined as $C = T\left(\partial S / \partial T\right)$. Therefore, we can write the difference in specific heat between superconducting and normal states as:

$$C_s - C_n = \frac{T}{4\pi}\left[\left(\frac{\partial H_c}{\partial T}\right)^2 + H_c \frac{\partial^2 H_c}{\partial T^2}\right] \tag{2.8}$$

At T = T_c, H_c = 0, then we have:

$$\Delta C\big|_{T=T_c} = \frac{T_c}{4\pi}\left(\frac{\partial H_c}{\partial T}\right)^2\Bigg|_{T=T_c} \tag{2.9}$$

Equation (2.9) is known as the Rutgers formula. It implies there is a discontinuous jump at T = Tc in the specific heat as a function of temperature. The Rutgers formula defines the height of the jump. The temperature dependence of the specific heat is plotted in Fig 2.4(b).

2.4 London Theory

The first phenomenological theory of superconductivity was developed by London brothers in 1935 [76]. The theory is based on two-fluid model which states that in a superconductor at $T < T_c$, only a fraction $n_s(\mathrm{T})/n$ of the total number of conduction electrons are capable of participating in a supercurrent. $n_s(T)$ is known as the density of superconducting electrons. It approaches the full electronic density n as T falls well below T_c, but it drops to zero as T rises to T_c. The remaining fraction of electrons is assumed to constitute a "normal fluid" of density $n - n_s$ that cannot carry an electrical current without normal dissipation. The normal and superconducting currents are assumed to flow in parallel.

For the superconducting electrons, London proposed two equations to describe their motion in electromagnetic fields:

$$E = \frac{\partial}{\partial t}(\Lambda J_s) \tag{2.10}$$

$$H = -c(\nabla \times \Lambda J_s) \tag{2.11}$$

Here $J_s = n_s e v_s$ is the supercurrent density, and $\Lambda = \frac{m}{n_s e^2}$.

While the Maxwell equation tells us that $\nabla \times H = \frac{4\pi}{c} J$, plugging this equation into equation (2.11) gives:

$$H + \lambda^2 \nabla \times (\nabla \times H) = 0 \tag{2.12}$$

where $\lambda^2 = \frac{mc^2}{4\pi n_s e^2}$. The solution to equation (2.12) in 1D with a semi-infinite superconductor occupying the $x > 0$ half space and an external applied field of H_0 along the z axis is given by:

$$H(x) = H_0 e^{-x/\lambda} \tag{2.13}$$

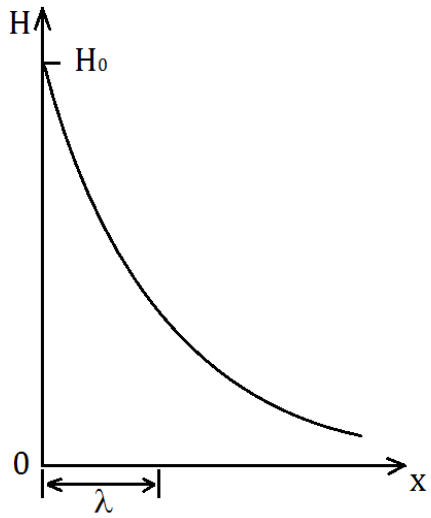

Fig 2.5 Magnetic field penetration into a bulk superconductor. The field at the surface is H_0

What this means is that the magnetic field falls off exponentially with increasing distance from the surface of the superconductor. The characteristic decay length λ which characterizes the

strength of magnetic field penetrating into the superconductor is called the London penetration depth.

London theory was successful in explaining the Meissner effect. However, it failed to take into account quantum effects and cannot explain the phenomenon of vortices.

2.5 Ginzburg-Landau theory

The Ginzburg-Laudau (GL) theory [77] is based on the theory of second-order phase transitions developed by Landau. A pseudowavefunction $\Psi(r) = |\Psi(r)|e^{i\phi}$ was introduced as a complex order parameter. $|\Psi(r)|^2$ was to represent the local density of superconducting electrons, $n_s(r)$. When temperature is close to T_c ($T_c - T \ll T_c$), the order parameter is small. According to Landau's theory of second order phase transitions, the free energy can be expanded in powers of $|\Psi|^2$ and $|\nabla\Psi|^2$. In the case of an inhomogeneous superconductor in a uniform external magnetic field near T_c, the Gibbs free energy can be written as [78]:

$$G_s(H) = G_n + \int \left[\alpha|\Psi|^2 + \frac{\beta}{2}|\Psi|^4 + \frac{\hbar^2}{2m^*}\left|\nabla\Psi - i\frac{e^*}{\hbar c}\mathrm{A}\Psi\right|^2 + \frac{(\nabla\times A)^2}{8\pi} - \frac{(\nabla\times A)\cdot \mathrm{H}_0}{4\pi}\right] dV \tag{2.14}$$

Where $|\Psi|^2 = n_s^*$ is the superfluid density; A is the vector potential; $B = \nabla\times A$ is the local magnetic field; H_0 is the external magnetic field. α and β are phenomenological expansion coefficients which are characteristics of the material.

Minimizing the above GL free energy with respect to Ψ , one can derive the first equation of Ginzburg-Landau theory and its boundary condition:

$$\begin{aligned} &\alpha\Psi + \beta\Psi\left|\Psi\right|^2 + \frac{1}{2m^*}(i\hbar\nabla + \frac{e^*}{c}\mathrm{A})^2\ \Psi = 0 \\ &(i\hbar\nabla\Psi + \frac{e^*}{c}\mathrm{A}\Psi)\cdot n = 0 \end{aligned} \tag{2.15}$$

where **n** is the unit vector normal to the surface of the superconductor. Similarly, one can minimize the free energy with respect to **A** and derive the second equation of GL theory:

$$J = \frac{c}{4\pi}\nabla\times(\nabla\times A) = \frac{e^*\hbar}{2m^* i}(\Psi^*\nabla\Psi - \Psi\nabla\Psi^*) - \frac{e^{*2}}{m^* c}\left|\Psi\right|^2\mathrm{A} \tag{2.16}$$

To simplify and help the understanding of the GL equations, two new parameters are introduced to substitute for α and β

$$\begin{aligned} \xi^2 &= \frac{\hbar^2}{2m^*\left|\alpha\right|} \\ \lambda^2 &= \frac{m^* c^2}{4\pi n_s^* e^{*2}} = \frac{m^* c^2\beta}{4\pi e^{*2}\left|\alpha\right|} \end{aligned} \tag{2.17}$$

In terms of the above new parameters and the normalized order parameter $\psi(\mathrm{r}) = \Psi(\mathrm{r})/\Psi_0$; $\Psi_0 = n_s^* = \left|\alpha\right|/\beta$, the GL equations can be written in a more concise and convenient form:

$$\xi^2(i\nabla + \frac{2\pi}{\Phi_0}\mathrm{A})^2\psi - \psi + \psi\left|\psi\right|^2 = 0 \tag{2.18}$$

$$\nabla\times\left(\nabla\times\mathrm{A}\right) = -i\frac{\Phi_0}{4\pi\lambda^2}\left(\psi^*\nabla\psi - \psi\nabla\psi^*\right) - \frac{\left|\psi\right|^2}{\lambda^2}\mathrm{A} \tag{2.19}$$

Where $\Phi_0 = \pi\hbar c / \mathrm{e}$ is the flux quantum. ξ is the coherence length which is characteristic length scale over which the order parameter varies and λ is the penetration depth. The physical meaning and importance of these two characteristic lengths will be discussed in details in the following analysis.

Consider an infinite superconductor in the x>0 semi-space with an interface to vacuum or an insulator in the x<0 semi-space. Assuming there is no applied magnetic fields or current. In this case, it is reasonable to consider the normalized order parameter $\psi(x)$ as a real term. The first GL equation can be reduced to a simple form:

$$-\xi^2 \frac{d^2\psi}{dx^2} - \psi + \psi^3 = 0 \tag{2.20}$$

The boundary conditions for this case are:

$$\psi \to 1\ ;\ \frac{d\psi}{dx} \to 0 \ \text{ when } x \to \infty$$
$$\psi = 0 \text{ at } x = 0$$

The solution to this equation is $\psi(x) = \tanh(\frac{x}{\sqrt{2}\xi})$. A plot of the order parameter $\psi(x)$ as a function of x is shown in Fig 2.6.

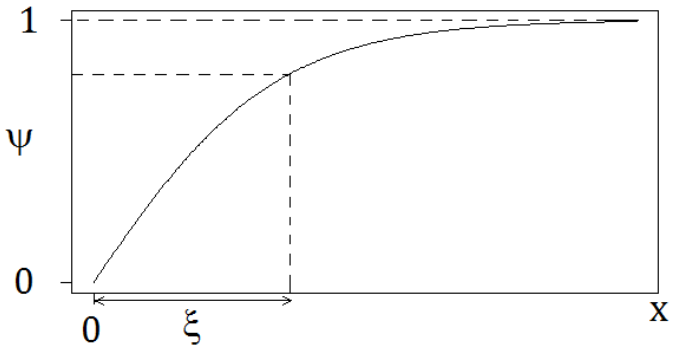

Fig 2.6 Normalized order parameter as a function of depth in a superconductor

It clearly shows that ξ is indeed the characteristic scale over which the variation of the order parameter ψ occurs. The other quantity, λ , introduced in equation (2.17) is already known to us. This is just the penetration depth for a weak magnetic field. Both λ and ξ are temperature dependent due to the temperature dependence of α and β.

In order to find a good approximation of the temperature dependence of α and β, let's consider the simplest case: a homogeneous superconductor without external applied magnetic fields. In this case Ψ does not depend on **r** and the expansion of the free energy in powers of $|\Psi|^2$ near T_c becomes:

$$F_{s0} = F_n + \alpha|\Psi|^2 + \frac{\beta}{2}|\Psi|^4 \tag{2.21}$$

Here F_{s0} is the free energy density of the superconductor in the absence of magnetic field, and F_n is its free energy density in the normal state. The sign of β is required to be positive since F_{s0} is not always favorable for any arbitrarily large value of $|\Psi|^2$. By minimizing the Helmholtz free energy with respect to $|\Psi|^2$, one gets:

$$|\Psi_0|^2 = -\alpha / \beta \tag{2.22}$$

Substituting (2.22) into (2.21), we can find the difference in free energy:

$$F_n - F_{s0} = \alpha^2 / 2\beta \tag{2.23}$$

And this difference equals $H_c^{\,2} / 8\pi$, and we have:

$$H_c^{\,2} = 4\pi\alpha^2 / \beta \tag{2.24}$$

Using the empirical formula $H_c(\mathrm{T}) = H_c(0)\left[1-\left(\frac{T}{T_c}\right)^2\right]$, to a first approximation we can assume $\alpha \propto (T - T_c)$ and $\beta = \text{const}$. Therefore, in the temperature interval close to T_c:

$$\lambda \propto (T_c - T)^{-1/2}, \qquad \xi \propto (T_c - T)^{-1/2} \tag{2.25}$$

The Ginzburg-Landau parameter κ is defined as the ratio of the penetration depth λ and the coherence length ξ: $\kappa = \lambda / \xi$ and by plugging in the expressions for ξ and λ, i.e. equation (2.17), the GL parameter can be written as $\kappa = 2\sqrt{2}\,\frac{e}{\hbar c}\lambda^2 H_c$ and from there we obtain the expression for the thermodynamic critical field H_c:

$$H_c = \frac{\Phi_0}{2\sqrt{2}\pi\lambda\xi} \tag{2.26}$$

We already know that type I and type II superconductors show entirely different responses to an external magnetic field. The reason is that the surface energy of the interface between a normal and a superconducting region, σ_{ns}, is positive for type I superconductors and negative for type II superconductors. To look into the details of this argument, let's consider a flat Normal-Superconductor (NS) interface within a superconductor in the intermediate state. From GL theory, we can derive the NS interface energy as:

$$\sigma_{ns} = \frac{H_c^2}{2\pi}\int_{-\infty}^{\infty}\left[\xi^2\left(\frac{d\psi}{dx}\right)^2 + \frac{H(H-H_c)}{2H_c^2}\right]dx \tag{2.27}$$

The first term in the integrand is nonzero over a distance x ~ ξ, since the order parameter changes from 0 to 1 in the vicinity of the NS interface over a distance of the order of the coherence length

ξ as we have discussed earlier. Thus the first term of the integral is of the order of ξ. Note that the field penetrating the superconducting region is always less than the field at the interface, that is, less than H_c. Therefore the second term is always negative. This term $\frac{H(H-H_c)}{2H_c^2}$ reaches approximately -1 at the interface and becomes zero deep in the interior of both S and N domains. The area where it is nonzero extends over a distance of the order of λ.

Consider two limiting cases:

(1) $\kappa \ll 1$, i.e., $\lambda \ll \xi$. Then, the dominant contribution to the NS interface energy comes from the first term and $\sigma_{ns} \sim H_c^2 \xi > 0$. Fig 2.7 shows how the order parameter ψ and the magnetic field **H** vary in the vicinity of the interface. We can see there is a region of thickness ~ ξ where the order parameter is already sufficiently small and the magnetic field is kept out. This result in an increase of the region's energy due to additional energy required to break the Cooper pairs with the region.

(2) $\kappa \gg 1$, i.e., $\lambda \gg \xi$. The dominant contribution to the NS interface energy comes from the second term and $\sigma_{ns} \sim -H_c^2 \lambda < 0$. Fig 2.8 shows the variation of ψ(x) and **H**(x) in this case. This time, ψ varies much more rapidly than the magnetic field so that there is a region of thickness ~ λ where the order parameter ψ is close to 1. This results in a gain of the condensation energy in the interface region.

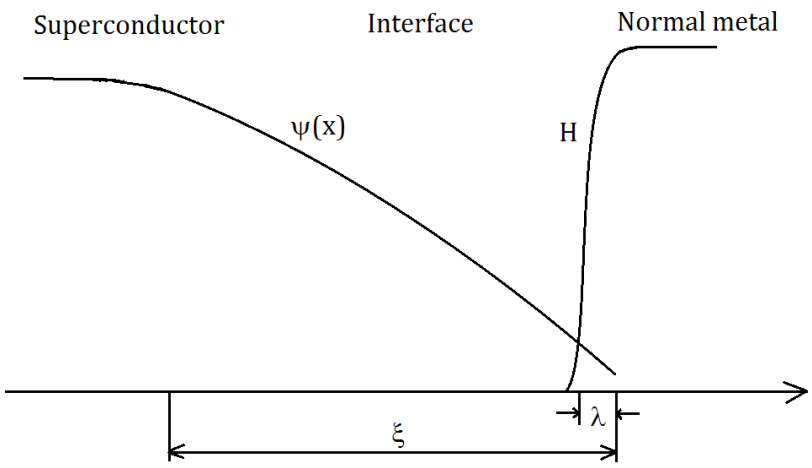

Fig 2.7 Spatial variation of the order parameter ψ and the magnetic field **H** in the vicinity of the NS interface for $\kappa \ll 1$

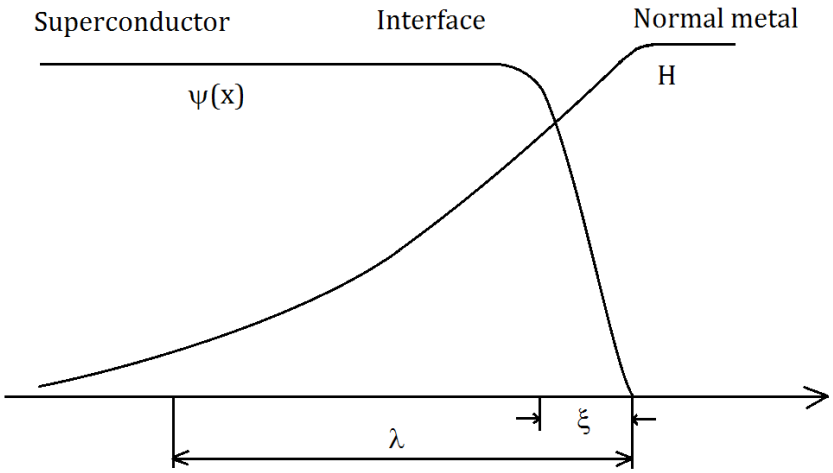

Fig 2.8 Spatial variation of the order parameter ψ and the magnetic field **H** in the vicinity of the NS interface for $\kappa \gg 1$

Thus, if $\kappa \ll 1$, then $\sigma_{ns} > 0$. Such materials are called type I superconductors. If $\kappa \gg 1$, then $\sigma_{ns} < 0$. Such materials are called type II superconductors. Exact calculations show that the

crossover from positive to negative of the interface energy occurs at $\kappa = 1/\sqrt{2}$ and this value sets the boundary between type I and type II superconductors.

In type II superconductors, when the applied field is higher than Hc1, the magnetic field begins to penetrate into the superconductor in the form of discrete vortex filaments, with each vortex consisting of a normal state core carrying a quantum of flux $\Phi_0 = 2.07 \times 10^{-7} G \cdot cm^2$. These flux tubes arrange themselves into a triangular or hexagonal pattern to achieve the lowest possible energy (Fig. 2.9). The solution to an isolated vortex in an infinite superconductor in GL theory is:

$$h(r) = \frac{\Phi_0}{2\pi\lambda^2} K_0(r/\lambda) \tag{2.28}$$

for the region of the vortex outside of the normal core. K_0 is the Hankel function of imaginary argument.

The asymptotic behavior of this function is:

$$K_0(z) \sim \begin{cases} \ln(1/z) & \text{at } z \ll 1 \\ e^{-z}/z^{1/2} & \text{at } z \gg 1 \end{cases} \tag{2.29}$$

The field at the center of the vortex can be obtained to logarithmic accuracy as:

$$H(0) \approx \frac{\Phi_0}{2\pi\lambda^2} \ln\kappa \tag{2.30}$$

The spatial variation of the magnetic field of an isolated vortex is shown in Fig 2.9.

The free energy of an isolated vortex line per unit length, or more accurately, the free energy of a superconductor containing one vortex, ε, measured relative to its free energy without the vortex can be derived in GL theory as:

$$\varepsilon = \left(\frac{\Phi_0}{4\pi\lambda} \right)^2 (\ln\kappa + 0.08) \tag{2.31}$$

In an external applied field H_0, the energy that is a minimum at equilibrium is the Gibbs free energy G. per unit length of the vortex, this energy is:

$$G = \varepsilon - \int \frac{B \cdot H_0}{4\pi} dV \tag{2.32}$$

H_0 can be taken out of the integral and recalling that the vortex carries one flux quantum Φ_0, we have:

$$G = \varepsilon - \frac{\Phi_0 H_0}{4\pi} \tag{2.33}$$

Clearly, for a sufficiently weak external field H_0, G > 0 and vortex formation is not favored. However, there exists such a field H_{c1}, starting from which G becomes negative and the formation of a vortex reduces the free energy. It follows from (2.33) and (2.31) that:

$$H_{c1} = \frac{\Phi_0}{4\pi\lambda^2} (\ln\kappa + 0.08) \tag{2.34}$$

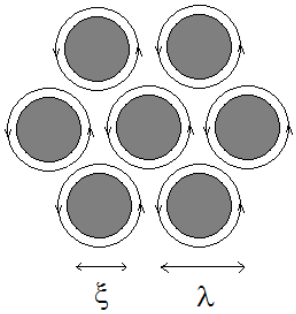

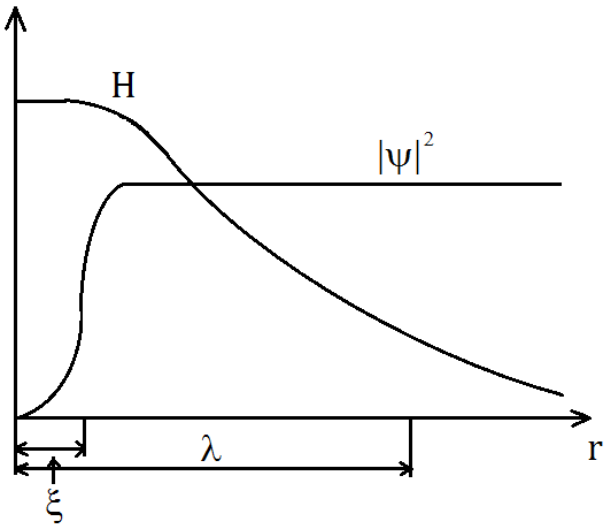

Fig 2.9 Triangular lattice arrangements of vortices in the mixed state of type II superconductor (left); Spatial distributions of the order parameter and the magnetic field of a single vortex (right).

When type II superconductor is in the mixed state and the external applied field is increased, the period of the vortex lattice decreases and when it becomes of the order of the coherence length ξ, a second order phase transition occurs from the mixed state to the normal state. This happens when the external fields reaches H_{c2}, the upper critical field.

It can then be derived from GL theory that the upper critical field is given by:

$$H_{c2} = \sqrt{2}\kappa H_c = \frac{\Phi_0}{2\pi\xi^2} \tag{2.35}$$

We can see that by measuring the upper critical field H_{c2} of a superconductor we can actually derive the coherence length, ξ.

What we have discussed above are the critical fields for a homogeneous isotropic superconductor. In the case of an anisotropic tetragonal superconductor, the upper critical fields are given by:

$$\begin{aligned} H_{c2\|c} &= \frac{\Phi_0}{2\pi\xi_{ab}^2} \\ H_{c2\|ab} &= \frac{\Phi_0}{2\pi\xi_{ab}\xi_c} \end{aligned} \tag{2.36}$$

The anisotropy of the upper critical fields stems from the anisotropy of the coherence length, which originates from the anisotropy of the effective mass since $\xi_i^2(\mathrm{T}) = \frac{\hbar^2}{2m_i|\alpha(T)|}$, where i identifies a particular principal axis. The anisotropy can be written as:

$$\gamma \equiv \left(\frac{m_c}{m_{ab}}\right)^{1/2} = \frac{\lambda_c}{\lambda_{ab}} = \frac{\xi_{ab}}{\xi_c} = \left(\frac{H_{c2\|ab}}{H_{c2\|c}}\right) = \left(\frac{H_{c1\|c}}{H_{c1\|ab}}\right) \tag{2.37}$$

The angular dependence of the H_{c2} can be worked out in the anisotropic GL approximation:

$$H_{c2}(\theta) = \frac{H_{c2\|ab}}{\left(\cos^2\theta + \gamma^2 \sin^2\theta\right)^{1/2}} \tag{2.38}$$

Where θ is the angle between the magnetic field and the ab plane.

2.6 BCS theory

The physical mechanism of superconductivity became clear only 46 years after the phenomenon had been discovered, when Bardeen, Cooper and Schrieffer published their theory (the BCS theory) [79-81]. The first hint at the origin of superconductivity came with the discovery of the isotope effect [82, 83]. It was found that different isotopes of the same superconducting metal have different critical temperatures, T_c and they obey the relation $T_c M^a = const$ where M is the mass of the isotope and the exponent **a** is close to 0.5. Thus it became clear that the lattice of ions in a metal is an active participant in creating the superconducting state.

In 1950, Frolich [84] demonstrated that electrons can indirectly interact with each other in a crystal by emitting and absorbing phonons. Electron 1 with wave vector k_1 emits a phonon and goes to state k_1', electron 2 with wave vector k_2 absorbs this phonon and goes to state k_2'. This process can be understood as the mutual scattering of two electrons in (k_1, k_2) state into (k_1', k_2') state through electron-phonon interactions. By this interaction, electrons within a thin shell of ~ $\hbar\omega_D$ in the vicinity of the Fermi surface are attractive to each other.

In 1956, Cooper considered two electrons which are attractive to each other above the Fermi surface. He solved the two-body Schrodinger equation and calculated the binding energy between

these two electrons. He found the binding energy is always negative and a bound pair with negative potential can always be formed no matter how small the attractive interaction is [79].

Combining the two facts above, Bardeen, Cooper and Schrieffer developed the microscopic theory of superconductivity. In a crystal, electron pairs (Cooper pairs) in the $\sim\hbar\omega_D$ shell near Fermi surface are formed due to attractive electron-electron interactions mediated by phonons. When such pairs of electrons are scattered from below the Fermi surface to above the Fermi surface, the potential energy is lowered while the kinetic energy is increased. If the decrease of potential energy is larger than the increase of the kinetic energy, the ground state of the system is no longer the one for the normal state where all the electrons occupy the states inside the Fermi surface, as shown in Fig. 2.10 (a), but rather one in which some states above the Fermi surface are occupied and some states below the Fermi surface are empty, as shown in Fig. 2.10 (b). To form as many pairs as possible, so that the lowest energy state can be achieved, two electrons with opposite momentum are favored to form pairs, which mean $k_1 = -k_2 = k$, and if we also consider the electron spins, antiparallel configuration of the spins often lowers the energy even more. The electron pair with momentum (k,-k) and antiparallel spins is called a Cooper pair.

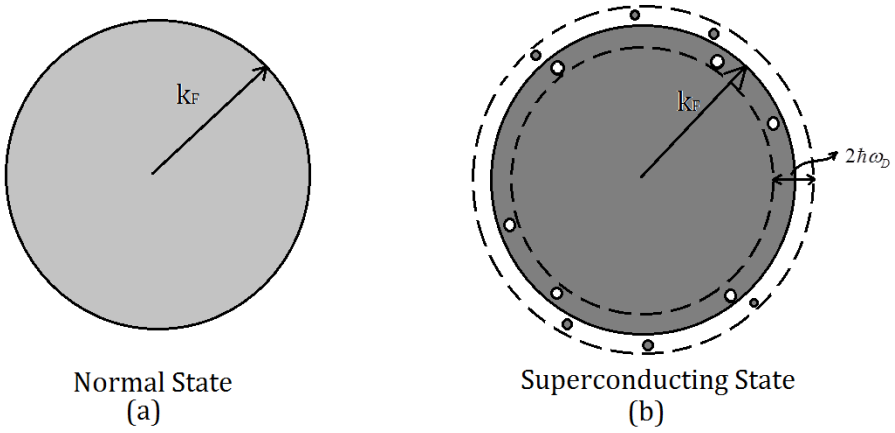

Fig 2.10 Schematic diagram of Fermi surface at (a) Normal ground state and (b) Superconducting state.

Due to Pauli Exclusion Principle, the wavefunction of the paired state should be antisymmetrical under particle exchange. If the spin of these two electrons form a spin singlet state (S=0), the spatial wavefunction would be with one of even parity, which means that the angular momentum should be L=0, 2, 4… etc. If the spins form a spin triplet state (S=1), the spatial wavefunction would have odd parity and the angular momentum should be L=1, 3 ..., etc. Except for very rare situations, such as the case of the ferromagnetic superconductor Sr_2RuO_4 [85], Cooper pairs have spin singlet configurations.

In BCS theory, to simplify the calculation, several assumptions are made. First, the Fermi surface is assumed to be a sphere. Second, the paired state is assumed to have L=0 and S = 0. Third, the electron-phonon interaction, $V_{kk'}$, is simplified as a constant:

$$V_{kk'} = \begin{cases} -V & \text{if } |\varepsilon_k| \le \hbar\omega_D, |\varepsilon_{k'}| \le \hbar\omega_D \\ 0 & \text{if } |\varepsilon_k| > \hbar\omega_D, |\varepsilon_{k'}| > \hbar\omega_D \end{cases} \tag{2.39}$$

where ε_k is the relative kinetic energy of the electron defined as:

$$\varepsilon_k = \frac{\hbar^2 k^2}{2m} - \frac{\hbar^2 k_F^2}{2m} \tag{2.40}$$

Introduce v_k^2 as the probability that paired state (k,-k) is occupied, the total energy of a superconductor in the state described by the distribution v_k^2 is:

$$E_s = \sum_k 2\varepsilon_k v_k^2 + \sum_{k,k'} V_{kk'} v_{k'} u_k v_k u_{k'} \tag{2.41}$$

where $u_k^2 = 1 - v_k^2$. Here the first term gives the total kinetic energy of the system and the second term is the mean potential energy of electron interaction. Now we can find the function v_k^2 such that the total energy E_s is a minimum. This requires:

$$\frac{\partial E_s}{\partial v_k^2} = 0 \tag{2.42}$$

Substituting (2.41) into (2.42), we obtain:

$$2\varepsilon_k - V\frac{1-2v_k^2}{v_k u_k}\sum_{k'}{}' v_{k'}u_{k'} = 0 \tag{2.43}$$

It follows that:

$$\frac{v_k u_k}{1-2v_k^2} = \frac{\Delta_0}{2\varepsilon_k}\ ,\ \Delta_0 = V\sum_k{}' v_k u_k \tag{2.44}$$

From (2.44) we can derive the following equation for v_k^2:

$$v_k^4 - v_k^2 + \frac{\Delta_0^2}{4E_k^2} = 0\ \ ,\ \ E_k = \sqrt{\varepsilon_k^2 + \Delta_0^2} \tag{2.45}$$

Then

$$v_k^2 = \frac{1}{2}(1 - \frac{\varepsilon_k}{E_k}) \tag{2.46}$$

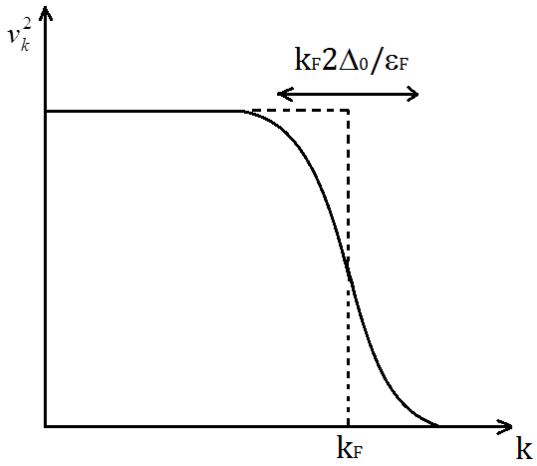

Fig 2.11 Dependence of v_k^2 on k. The region v_k^2 is smeared out is $2\Delta_0$

The dependence of v_k^2 on k is plotted in Fig 2.11. As we can see, the total energy of the system reaches its minimum when the electron distribution near the Fermi surface is "smeared out" over the energy interval ~ $2\Delta_0$. We emphasize that this happens at 0 K and this is the identity of the ground state of the superconductor.

To find the ground state energy of the superconductor, let's find Δ_0 first. Plugging (2.46) into the second expression in (2.44), we can get:

$$\begin{aligned}\Delta_0 &= V\sum\nolimits_k{}' \left[\frac{1}{2}\left(1-\frac{\varepsilon_k}{E_k}\right)\frac{1}{2}\left(1+\frac{\varepsilon_k}{E_k}\right)\right]^{1/2} \\ &= \frac{V\Delta_0}{2}\sum\nolimits_k{}' \left(\varepsilon_k^2+\Delta_0^2\right)^{-1/2}\end{aligned} \tag{2.47}$$

Changing the summation as integration, one can derive that:

$$1 = N(0)V\int_0^{\hbar\omega_D}\left(\varepsilon^2+\Delta_0^2\right)^{-1/2}d\varepsilon \tag{2.48}$$

where N(0) is the density of states at the Fermi energy. After integration we get:

$$\Delta_0 = \frac{\hbar\omega_D}{\sinh(\frac{1}{N(0)V})} \tag{2.49}$$

In the weak coupling limit: $\Delta_0 \simeq 2\hbar\omega_D \exp(-\frac{1}{N(0)V})$. To estimate Δ_0, let's take the Debye temperature $\hbar\omega_D / k_B \sim 100K$ and $N(0)V \sim 0.3$, we obtain $\Delta_0 / k_B \sim 4\text{K}$.

We can then derive the energy difference between the superconductor ground state and the normal ground state, the result is:

$$W = E_s - E_n = -\frac{1}{2} N(0)\Delta_0^2 \tag{2.50}$$

Recalling that this energy difference is also given by $H_c^{\,2}(0)/8\pi$, we can write down the expression for the thermodynamic critical field in terms of characteristic parameters of the superconductor:

$$H_c(0) = \Delta_0 \sqrt{4\pi N(0)} \tag{2.51}$$

The elementary excitation energy in the superconductors is given by:

$$E_k = \sqrt{\varepsilon_k^2 + \Delta_0^2} \tag{2.52}$$

This is the energy needed to add one extra electron to a superconductor in the ground state, we increase the energy of the system by at least the value of Δ_0. This means that the spectrum of elementary excitations of the superconductor is separated from the ground-state energy level by an energy gap. This is illustrated in Fig 2.12. The dependence of E_k on k given by (2.52) is shown in Fig 2.13.

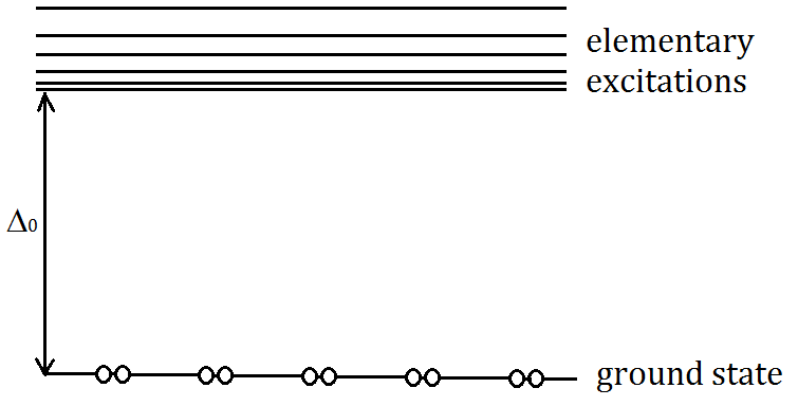

Fig 2.12 Energy gap Δ_0 separates the energy levels of elementary excitations from the ground-state level

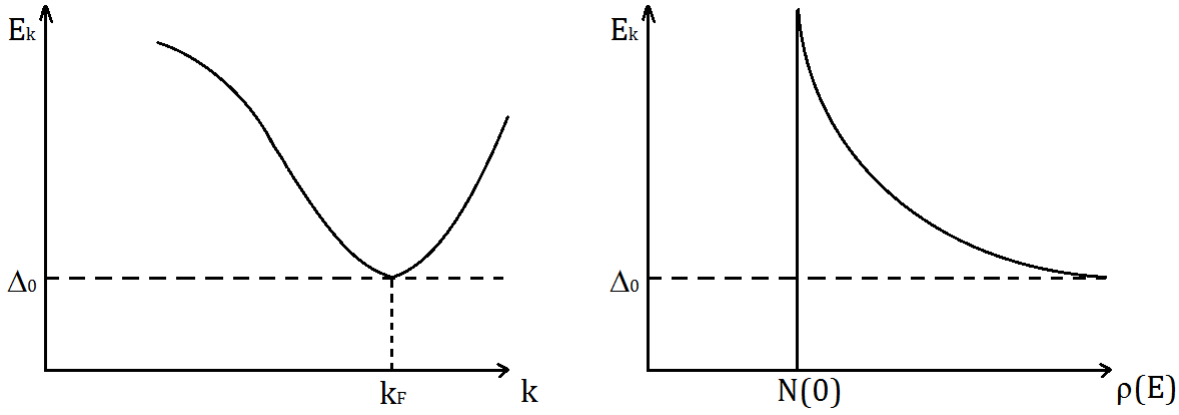

Fig 2.13 Energy dispersion of the elementary excitations of the superconductor (left) and the density of states (right)

The density of states of elementary excitations can be derived as:

$$\rho(E) = N(0)\frac{E}{\sqrt{E^2 - \Delta_0^2}} \tag{2.53}$$

It follows from (2.53) that the density of states of elementary excitations goes to infinity as $E \to \Delta_0$.

Let's now discuss how the superconducting coherence length can be evaluated using the microscopic theory. We have already seen that large variations of v_k^2 can occur only within $\Delta k \sim 2\Delta_0 \frac{k_F}{\varepsilon_F}$. In real space, large variations of the ground state wavefunction can be expected within $\Delta x \sim 1/\Delta k$ from the Uncertainty principle. It then follows:

$$\Delta x \sim \frac{\varepsilon_F}{2\Delta_0 k_F} = \frac{\hbar v_F}{4\Delta_0}$$

Thus $\xi_0 \sim \frac{\hbar v_F}{4\Delta_0}$, more rigorous calculations yields:

$$\xi_0 \sim 0.18 \frac{\hbar v_F}{k_B T_c} \tag{2.54}$$

As the temperature increases, the energy gap Δ decreases. This is easy to understand because the energy required to break a Cooper pair is 2Δ and if the temperature is such that $k_B T \sim 2\Delta$, it is evident that many Cooper pairs will be broken through thermal processes. As a result, more states will be occupied by elementary excitations (single electrons) and fewer states can form pairs that lower the superconductor's energy. An implicit expression of the temperature dependent gap is:

$$1 = N(0)V \int_0^{\hbar\omega_D} \frac{d\varepsilon}{\sqrt{\varepsilon^2 + \Delta^2(T)}} \tanh \frac{\sqrt{\varepsilon^2 + \Delta^2(T)}}{2k_B T} \tag{2.55}$$

The temperature dependence is the gap is shown in Fig 2.14. Near T_c, the variation of the gap with temperature obeys $\Delta \propto (T_c - T)^{1/2}$.

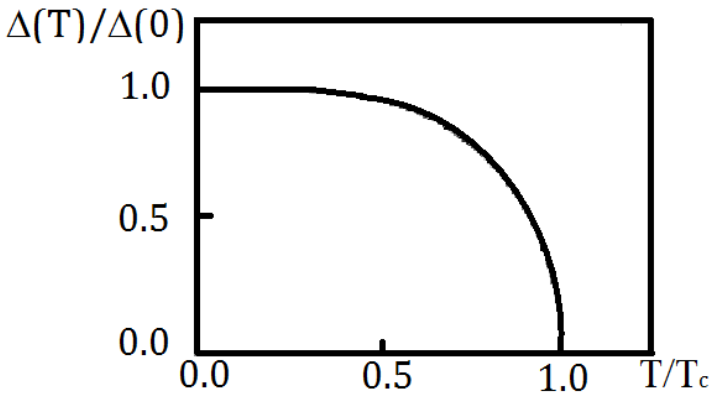

Fig 2.14 Temperature dependence of the energy gap in BCS theory

An expression of the critical temperature T_c can also be derived since at $T = T_c$, the gap $\Delta = 0$. Putting these two conditions in (2.55) gives us:

$$\frac{1}{N(0)V} = \int_0^{\hbar\omega_D} \frac{d\varepsilon}{\varepsilon} \tanh \frac{\varepsilon}{2k_B T_c} \tag{2.56}$$

Carrying out the integration, we get:

$$k_B T_c \simeq 1.14\hbar\omega_D \exp(-\frac{1}{N(0)V}) \tag{2.57}$$

We already know that, in the weak coupling limit: $\Delta_0 \simeq 2\hbar\omega_D \exp(-\frac{1}{N(0)V})$, then

$$2\Delta_0 = 3.53 k_B T_c \tag{2.58}$$

Some other important thermodynamic properties of BCS superconductors are:

(1) In the weak coupling limit, the specific heat jump can be expressed as the universal relation:

$$\left.\frac{C_s - C_n}{\gamma_n T}\right|_{T=T_c} = 1.43 \tag{2.59}$$

where $\gamma_n = \frac{1}{3}\pi^2 k_B^2 N(0)$ is the Sommerfeld constant in the normal state.

(2) In the weak coupling limit, the thermodynamic critical field can be expressed as:

$$H_c(0) = -0.55 T_c \left.\frac{dH_c}{dT}\right|_{T_c} \tag{2.60}$$

Where $\left.\frac{dH_c}{dT}\right|_{T_c} = 4.4\sqrt{\gamma_n}$.

(3) In the weak coupling limit, at very low temperature:

$$C \propto \frac{\Delta(0)^{2.5}}{T^{1.5}} \exp(-\frac{\Delta(0)}{k_B T}) \tag{2.61}$$

The superconducting gap is a very important quantity in superconductors not only because it determines the thermodynamic properties of superconductor, but also because it is closely related to the Cooper pair state and superconducting order parameter. It was proved [86] that the order parameter ψ(r) in GL theory is actually the pair wavefunction in BCS theory and is proportional to the superconducting gap. Therefore, by measuring the superconducting gap, information about the pairing symmetry, which is critical to determining the pairing mechanism, can be extracted.

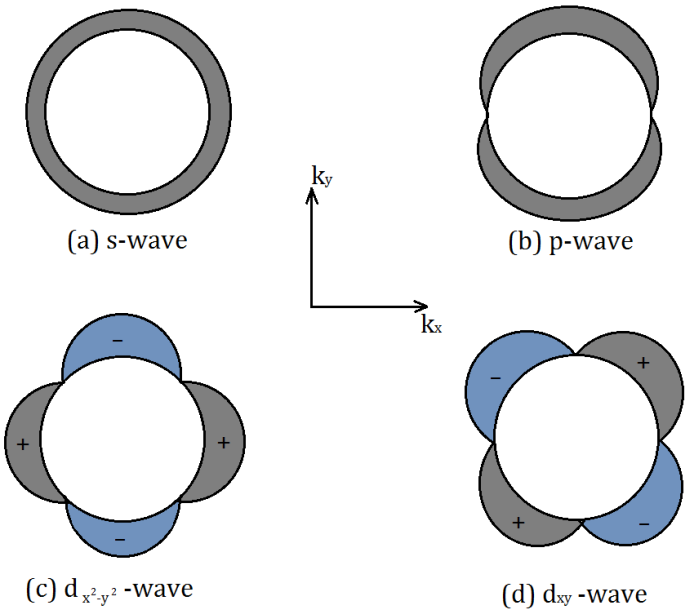

Fig 2.15 superconducting gap with different gap symmetries in k space.

Fig 2.15 shows the schematic representation of Δ in *k* space. Fig 2.15(a) shows the isotropic *s*-wave superconducting gap with $L = 0$ and $S = 0$, the superconductor is fully gapped, which is the situation discussed in the original BCS theory. For the so called $s\pm$ wave pairing symmetry, which was proposed to be favored in Fe-based superconductors, the superconductor is fully

gapped on both electron and hole Fermi sheets but with opposite signs between them [33]. Fig. 2.15(b) shows the anisotropic *p*-wave gap with $L = 1$ and $S = 1$. Fig 2.15(c) and (d) show the anisotropic *d*-wave gap with $L = 2$ and $S = 0$. For different gap symmetries, the angular dependent superconducting gap, $\Delta(k)$, can be written as:

$$\Delta(k) \propto \begin{cases} 1 & \text{isotropic s-wave} \\ \cos(2\varphi) & d_{x^2-y^2}\text{-wave} \\ \sin(2\varphi) & d_{xy}\text{-wave} \end{cases} \tag{2.62}$$

The gap anisotropy is defined as:

$$\Omega = 1 - \frac{\langle \Delta(k) \rangle^2}{\langle \Delta(k)^2 \rangle} \tag{2.63}$$

which is 0 for isotropic s-wave superconductor and 1 for d-wave superconductors.

2.7 Theory of nematic phase transition in FeSCs

The theory of nematic order in Fe-based superconductors was established by several authors and two different mechanisms have been proposed, i.e. spin-nematic [54-58] and orbital-order [49-53]. In the spin driven Ising-nematic scenario, the qualitative idea is simple and can be understood using symmetry arguments [57], as shown in Fig 2.16. In many antiferromagnets, the symmetry that is broken at the magnetic transition temperature is the *O*(3) spin-rotational symmetry. To the *O*(3) symmetry-breaking corresponds also a translational symmetry-breaking, due to the increase in the

size of the crystalline unit cell in the magnetically ordered phase. In the iron pnictides, however, the situation is different. The SDW ground state is actually doubly degenerate, as it is characterized by magnetic stripes of parallel spins along either the y axis (ordering vector $\mathbf{Q}_1$ = (π,0)) or the x axis (ordering vector $\mathbf{Q}_2$ = (0, π)). Therefore, to go to the ordered state, the system has to break not only the $O(3)$ spin-rotational symmetry, but it also has to choose between two degenerate ground states, which corresponds to a Z_2 (Ising-like) symmetry. Since Z_2 is a discrete symmetry, the Z_2 symmetry-breaking is expected to be less affected by fluctuations than the continuous $O(3)$ symmetry-breaking, what opens up the possibility of the former happening before the latter.

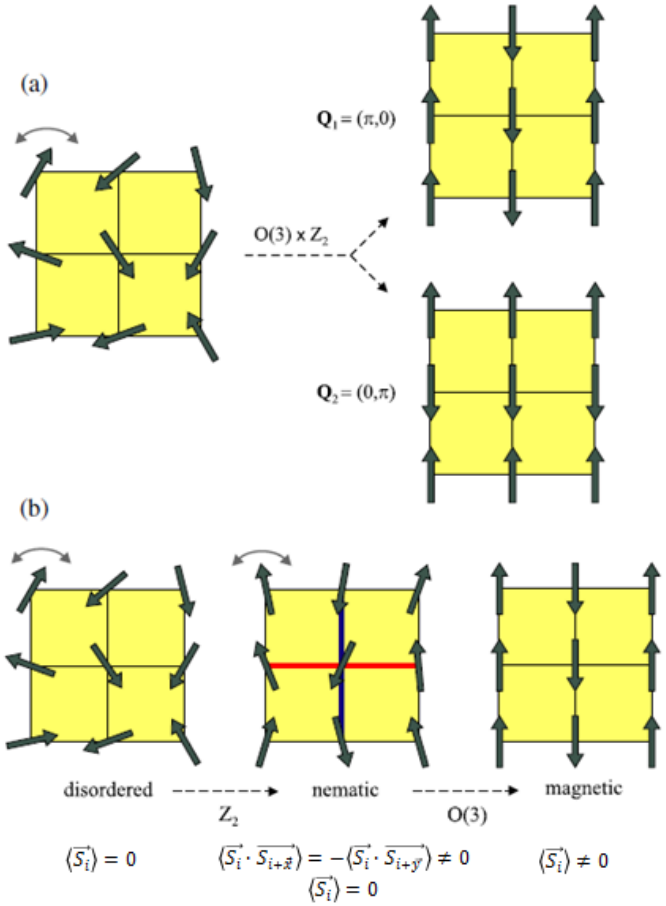

Fig 2.16 Schematic representation of the nematic phase transition in real space. (a) The transition from the paramagnetic phase to the stripe ordered SDW phase breaks $O(3) \times Z_2$ symmetry. (b)

The symmetry breaking in two successive steps. First, the Z_2 symmetry is broken but the system is still in the paramagnetic state, but the spin correlations break the tetragonal symmetry. In the second step, the *O*(3) symmetry is broken and the system acquires long range magnetic order [57].

This leads to the idea of an Ising-nematic state: an intermediate phase preceding the SDW state, where the Z_2 symmetry is broken but the *O*(3) symmetry is not. In real space, the Z_2 symmetry breaking corresponds to a broken tetragonal symmetry, since the correlation functions $\left\langle \vec{S}_i \cdot \vec{S}_{i+\bar{x}} \right\rangle$ and $\left\langle \vec{S}_i \cdot \vec{S}_{i+\bar{y}} \right\rangle$ acquires opposite signs. This is an analogy of the nematic phase in liquid crystals, which is characterized by broken rotational symmetry and unbroken translational symmetry. Although translational symmetry and rotational symmetry are always broken in crystals, the analogy remains valid: in the electronic nematic phase, the point-group symmetry is reduced from C_4 to C_2 corresponding to additional lowering of the rotational symmetry. From a purely symmetry point of view, the nematic state is therefore equivalent to the orthorhombic phase, which is the result of the inevitably induced distortion of the crystalline lattice. The term 'nematic' is however used to emphasize the fact that the phase transition is of purely electronic origin and would still take place in a perfectly rigid lattice. The nematic susceptibility measurements by Chu *et al* [46] demonstrated indeed the existence of a divergence of the nematic susceptibility at the structural transition in $Ba(Fe_{1-x}Co_x)_2As_2$, which gives firm evidence that the structural transition from C_4 to C_2 symmetry in FeSCs is indeed driven by electronic nematicity. The phase diagram of iron pnictides, after the incorporation of the influence of electronic nematicity, is shown in Fig 2.17.

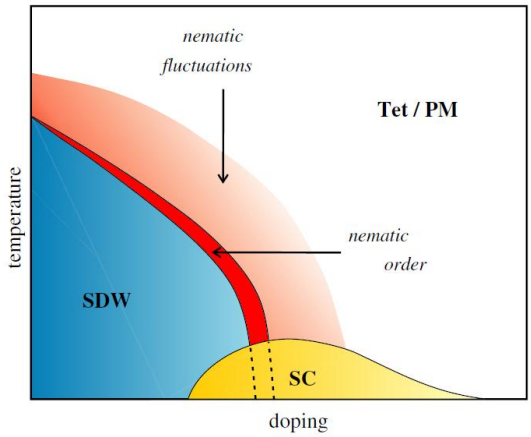

Fig 2.17. Nematic phase diagram of FeSCs. SDW denotes the spin-density wave state, SC the superconducting state, PM the paramagnetic phase and Tet the tetragonal phase. Tetragonal symmetry is broken only below nematic/structural transition line, but nematic fluctuations remain at higher temperatures [57].

The mechanism behind the spontaneous breaking of the additional Ising symmetry is reminiscent of the order-out-of-disorder mechanism put forward by Chandra *et al* in the context of localized-spin models [87]. Not surprisingly, the first model calculations that obtained a spontaneous nematic phase in the pnictides were based on a strong-coupling approach, the so-called J_1–J_2 model [54, 55, 88]. More recently, it was shown that an itinerant description of the system also accounts for a preemptive nematic phase [56]. Notwithstanding important differences between the strong-coupling and weak-coupling approaches—in particular on the character of the nematic and magnetic transitions as function of doping and pressure [56]—they share similar physics: magnetic fluctuations spontaneously break the tetragonal symmetry already in the paramagnetic phase.

A brief discussion of the J_1-J_2 model is given below following the paper by C. Fang *et al* [55]. It has to be emphasized beforehand that a model of localized spins cannot be taken as a realistic representation of the electronic structure in iron-pnictides. The most obvious point is that FeSCs

are metallic, or more rigorously, semi-metallic. However, the model is sufficiently simple and its predictions agree qualitatively with experimental results.

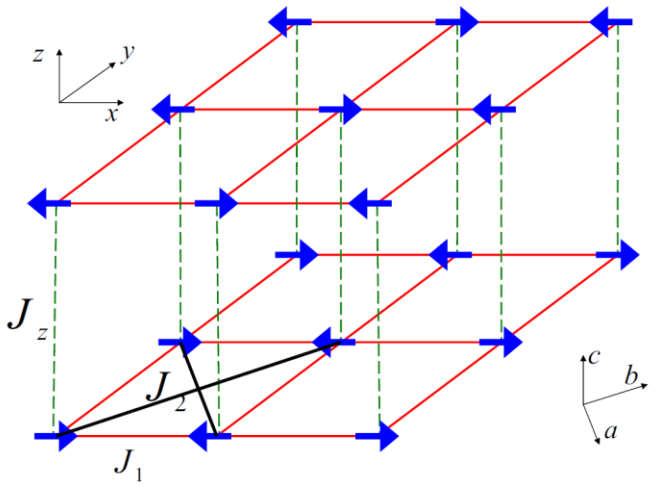

Fig 2.18 Schematic showing the nearest neighbor coupling J_1, next nearest neighbor coupling J_2, and the interlayer coupling J_z, and the orientation of spins in the J_1-J_2 model [55].

In the tetragonal phase, the iron sites form square planar arrays, such that the sites of adjacent planes lie above one another. Because the superexchange is mediated through off plane but plaquette centered As atoms, the first- and second-neighbor antiferromagnetic exchange couplings, J_1 and J_2, are expected to be of roughly the same magnitude. However, the coupling between spins on neighboring planes, J_z, while still antiferromagnetic, is expected to be much smaller than the in-plane couplings (Fig 2.18). Estimates from previous work [87] are $J_1 \approx 0.5 J_2 \approx 400 - 700$ K . J_z is several orders of magnitude smaller than J_2. The resulting minimal Hamiltonian is:

$$H = \sum_{n,R,\delta_1} [J_1 \vec{S}_{R,n} \cdot \vec{S}_{R+\delta_1,n} - K(\vec{S}_{R,n} \cdot \vec{S}_{R+\delta_1,n})^2] + J_2 \sum_{n,R,\delta_2} \vec{S}_{R,n} \cdot \vec{S}_{R+\delta_2,n} + J_z \sum_{n,R} \vec{S}_{R,n} \cdot \vec{S}_{R,n+1} \quad (2.64)$$

Where $\vec{S}_{R,n}$ is a spin S operator on site **R** in plane *n*; δ_1 and δ_2 are first and second nearest neighbor lattice vectors; K is the biquadratic interaction term which is small. In the broken-symmetry "nematic" phase, the spin-nematic order parameter given in (2.65) is not zero. Since a structural distortion of appropriate symmetry is linearly coupled to the spin nematic order parameter, the magnitude of the structural distortion u will be proportional to N in the presence of weak electron-lattice coupling.

$$N \equiv \left\langle \sum_{\delta_1} F_d(\delta_1)\vec{S}_{R,n} \cdot \vec{S}_{R+\delta_1,n} \right\rangle; \qquad F_d(\pm\hat{x}) = -F_d(\pm\hat{y}) = 1 \tag{2.65}$$

The model is considered in the limit of $J_2 > J_1/2 \gg J_z$, $K > 0$. Finite temperature properties of the model is obtained by considering $\vec{S}$ as an N dimensional unit vector [*SO(N)* spin] and solving the problem in the large N limit. Without going into the details of the theoretical derivation, the results show that the above model has two second order phase transitions. The nematic transition temperature T_N is always larger than the SDW transition temperature T_{SDW}. The transition temperatures T_N and T_{SDW} as the function of $\tilde{J}_z$ for a fixed $\tilde{K} = 0.0075\tilde{J}_2$ are shown in Fig 2.19. The theoretical results agree qualitatively with the experimental observation of a structural transition preceding the SDW transition.

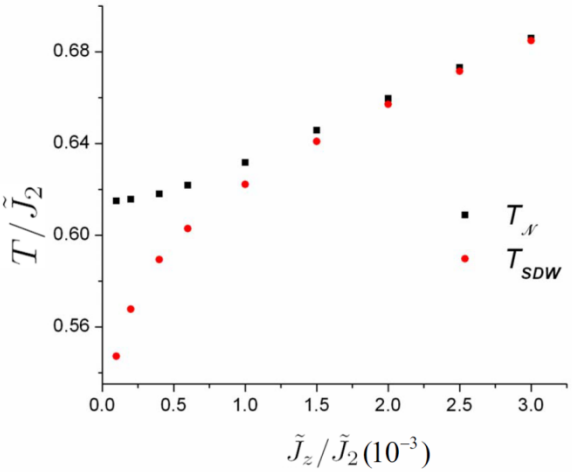

Fig 2.19 T_N and T_{SDW} as a function of $\tilde{J}_z$ for $\tilde{J}_1 = 2\tilde{J}_2$, $N = 3$ and $S = 1$ in the J_1-J_2 model [55].

Chapter 3

Experimental method: AC micro-calorimetry

3.1 Overview

Accurate thermodynamic measurements are essential to understanding the fundamental properties of materials. The heat capacity measurements probe the low energy excitations in solids, which played an important role in early studies of solid-state physics, e.g. measurements of the low temperature electronic specific heat of metals allows us to measure the Sommerfeld constant $\gamma = \frac{\pi^2}{3} k_B^2 N(0)$ because $C_e = \gamma T$ when $T \ll T_F$, which gives information about the density of states at the Fermi surface; while measurements of the low temperature lattice specific heat allows us to determine the Debye temperature (Θ_D) of the material ($C_{latt} = \frac{12\pi^4}{5} n k_B (\frac{T}{\Theta_D})^3$, when $T \ll \Theta_D$) [89]. In the study of unconventional superconductors, the measurements of heat capacity is also central to revealing new undiscovered phases, e.g. the discovery of vortex melting transition in high purity YBCO single crystals [90] and the more recent Chiral CDW phase in $TiSe_2$ [91], etc. and studying volume effects such as the superconducting state in a material, e.g. the confirmation of two-band superconductivity in MgB_2 by low temperature specific heat measurements [92].

In this thesis, I primarily use a built-in-house membrane based ac micro-calorimeter to study the thermodynamic properties of unconventional superconductors (High T_c cuprates, FeSCs). The advantageous design of the calorimeter allows accurate high resolution measurements of sub-μg

single crystals or films from room temperature down to sub-K in high magnetic fields (as high as 8T).

3.2 Calorimetric methods

The term calorimeter is used for the description of an instrument devised to determine heat and rate of heat exchange, and denotes the combination of sample and measuring system, kept in a well-defined surrounding, the thermal bath or shield, as shown in Fig 3.1 [93].

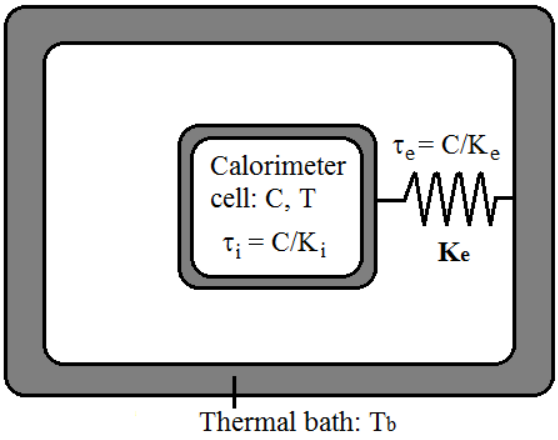

Fig 3.1 Schematic representation of a calorimeter [93]. The measuring cell is thermally connected to the thermal bath at temperature Tb with a thermal conductance of K_e. The internal and external time constants $\tau_i = C/K_i$ and $\tau_e = C/K_e$ represent the time in which thermal equilibrium is achieved in the calorimetric cell, and cell plus bath system respectively.

A list of common calorimetric methods is given in Table 3.1. Depending on the heat transfer conditions between the sample cell and the thermal bath, calorimeters can be divided in *isothermal*, *isoperibol*, and *adiabatic*. *Isothermal* calorimeters have both calorimeter and thermal bath at constant T_b. If only the surroundings are isothermal the mode of operation is called

isoperibol. In *adiabatic* calorimeters the exchange of heat between the calorimeter and the shield is kept close to zero by making the thermal conductance as small as possible.

Method	Typical condition	Measured quantity	Condition for good accuracy	Typical sample size
Heat pulse	Adiabatic	Temp. variation	$\tau_e >> \Delta t_h > \tau_i$	>200 mg
Thermal relaxation	Isoperibol	Temp. variation	$\tau_e >> \tau_i$	0.01 - 1 g
Continuous heating	Adiabatic	Temp. variation	$(T-T_b)/\tau_i >> dT/dt$	>100 mg
Differential calorimetry	Isoperibol	Heat flow	τ_e short	10 - 100 mg
AC steady state	Isoperibol	Temp. variation	$\omega\tau_e>1>\omega\tau_i$	sub μg - mg

Table 3.1 Principle methods used in modern calorimetry [94], T, T_b, τ_e and τ_i are explained in Fig 3.1. Δt_h represents the length of the heat pulse.

1) Heat pulse method

The heat-pulse method is realized by heating the sample for a finite time Δt_h and measuring the temperature increment ΔT. This method is the direct transposition of the thermodynamic definition of heat capacity:

$$C = \lim_{\Delta T \to 0} \frac{Q}{\Delta T} \tag{3.1}$$

where Q is the heat supplied to the sample and calorimeter in form of a pulse.

2) Thermal relaxation method

The thermal relaxation method consists of applying a known power P to the cell to raise the sample temperature by an amount $\Delta T = P/K_e$. When a steady state condition is reached the power is turned off and the temperature will drop back to the initial value with an exponential decay which depends on the external time constant $\tau_e = C/K_e$:

$$T = T_b + \Delta T e^{-t/\tau_e} \tag{3.2}$$

By fitting the exponential dependence of the sample temperature, one determines ΔT and τ_e. From these two quantities one can derive the thermal conductance between the calorimeter cell and bath, $K_e = P/\Delta T$ and the heat capacity of the cell, $C = \tau_e K_e$.

3) Continuous heating method

In the continuous heating method, heat is added continuously to the sample at constant power P and the resulting temperature increase is recorded. The heat capacity is given by the instantaneous derivative of the temperature T with respect to time as:

$$C = \frac{P}{dT / dt} \tag{3.3}$$

This method is usually performed under adiabatic conditions and is well suited for samples of high thermal conductivity which exhibit a short internal relaxation time τ_i. The requirements for a fast distribution of the heat within the calorimeter/sample system restrict its general application.

4) Differential scanning calorimeter (DSC)

DSC (Fig 3.2) is a thermal analysis method where differences in heat flow into a sample and a reference are measured as a function of sample temperature, while both are subjected to a controlled temperature program. There exist two types of DSCs: heat-flux DSCs and power-compensated DSCs.

In heat-flux DSC, the sample and reference assembly is enclosed in a single furnace which is heated with a linear heating rate:

$$T = T_b + \beta t \tag{3.4}$$

where T_b is the initial temperature and $\beta = dT/dt$ is the known heating rate. Owing to the heat capacity difference between the sample and reference, there would be a temperature difference between the sample and reference ΔT. The heat flow rate is proportional to ΔT through a temperature dependent proportionality factor E(T) which is related the geometry and the materials of construction of the device as $\dot{Q} = E(T)\Delta T$. The heat capacity is given by $C = \dot{Q} / \beta$.

In the power-compensated DSC the heat to be measured is compensated by increasing or decreasing an adjustable Joule heat. The measuring system consists of two identical furnaces, embedded in a large temperature controlled heat sink. The temperatures of the sample and reference are controlled independently and are made identical by varying the power input to the two furnaces; the energy required to do this is a measure of the heat capacity changes in the sample relative to the reference.

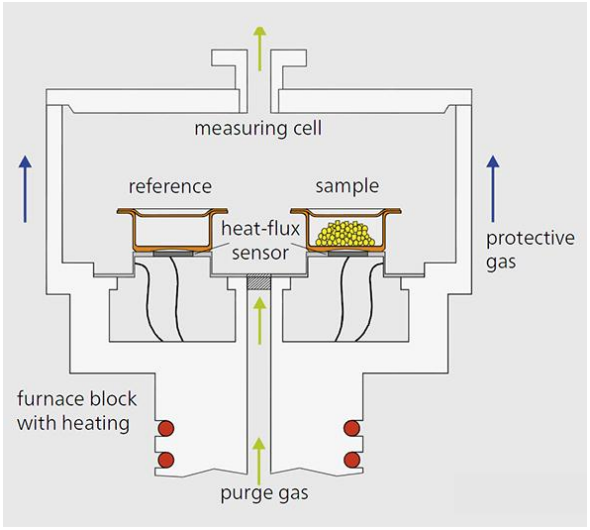

Fig 3.2 Schematic of a heat-flux differential scanning calorimeter [95]

5) 3ω method

The first measurement of specific heat using the temperature modulation was performed by Corbino in 1910/11 [96]. He used the resistance of electrically conducting samples to determine the temperature oscillations with a method known as third-harmonic (3ω) method. In this kind of experiment the same metal resistor element is used as both heater and thermometer. The heater, with resistance R, is driven by a current at frequency ω which results in a power of double the frequency:

$$I(t) = I_0 \cos \omega t \tag{3.5a}$$

$$P(t) = P_0(1 + \cos 2\omega t) \tag{3.5b}$$

where $P_0 = \frac{1}{2} I_0^2 R$. This power leads to temperature oscillations of frequency 2ω in the resistor, which to a first order approximation, leads to oscillations in the resistance of the resistor at the same frequency:

$$R(t) = R_0[1 + \alpha\delta T \cos(2\omega t + \phi)] \tag{3.6}$$

where $\alpha \equiv \frac{1}{R}\frac{dR}{dT}$ and ϕ is the phase shift between temperature oscillation δT and power oscillation. The combined effect on the voltage over resistor is then:

$$V(t) = I(t)R(t) = I_0 R_0 \cos\omega t + \frac{I_0 R_0}{2}\alpha\delta T \cos(\omega t + \phi) + \frac{I_0 R_0}{2}\alpha\delta T \cos(3\omega t + \phi) \tag{3.7}$$

The first term is the normal AC voltage at the drive frequency, while the second and third terms, which derive from mixing the current and resistance oscillations, are dependent on the δT. The temperature oscillation amplitude, in turn, is related to the sample heat capacity [97].

3.3 AC steady state calorimetry

AC steady state calorimetry was first developed by Sullivan and Seidel in their seminal 1968 paper [98, 99]. They employed an AC current to heat an indium sample that was coupled to a heat reservoir for which the resultant equilibrium temperature of the sample contained an AC term with a amplitude that was inversely proportional to the heat capacity and was measurable with high precision [98]. It must be acknowledged that this method was independently developed also by Kraftmakher and Handler [100], Mapother and Rayl [101] at about the same time, but we have become more familiar with Sullivan and Seidel's research. Since then, this method has been widely used, especially for small samples and it is the method which our membrane micro-calorimeter is based on.

3.3.1 Principles of AC steady state micro-calorimetry

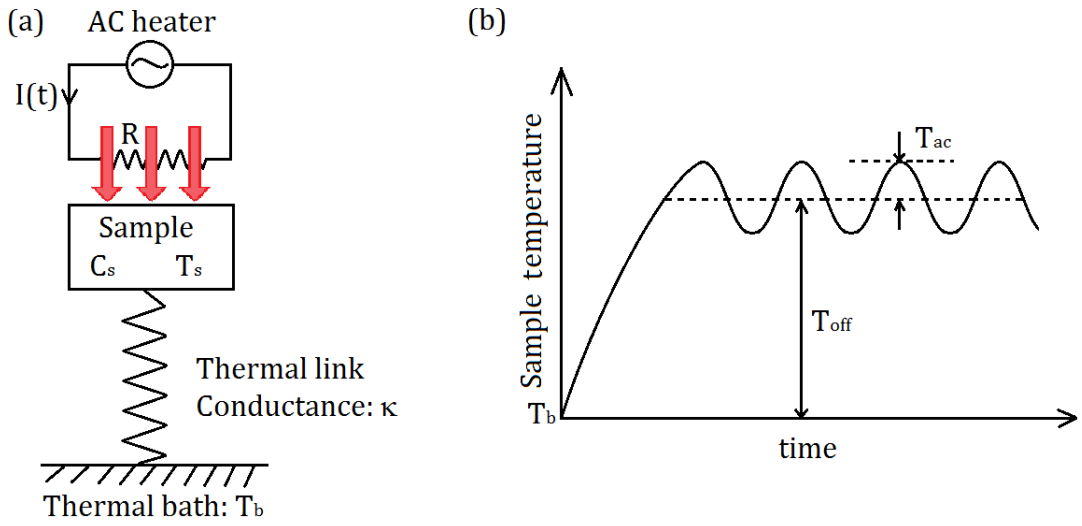

Fig 3.3 (a) Schematic of AC steady state specific heat measurement. A sample is connected to the thermal bath at T_b, and heated with an AC power. The temperature oscillation of the sample at steady state is measured by a thermometer. (b) Sample temperature plotted as a function of time. The DC offset temperature and AC temperature oscillations at steady state are marked in the plot.

Consider the system illustrated in Fig 3.3 (left). A sample with heat capacity C_s is placed on a substrate-base or platform that is weakly linked to a thermal bath with temperature T_b which has a large enough heat capacity comparing to the sample so that its temperature can be assumed constant. The thermal conductance between the sample and the heat bath is κ. Then the sample is heated by a small AC heating power which causing its temperature to oscillate with a small amplitude T_{ac} around the steady state condition of the bath. The ac current passed through the heater with resistance R and the power generated is given by equations (3.8) and (3.9) respectively:

$$I(t) = I_0 \sin \omega t \tag{3.8}$$

$$P(t) = I^2(t)R = \frac{P_0}{2}(1 - \cos 2\omega t); \quad P_0 = I_0^2 R \tag{3.9}$$

When the system reaches equilibrium, the heat balance equation gives:

$$\frac{dQ(t)}{dt} = P(t) = C_s \frac{dT_s(t)}{dt} + \kappa\left[T_s(t) - T_b\right] \tag{3.10}$$

where $T_s(t)$ is the sample temperature, Q(t) is the heat absorbed by sample. Substituting equation (3.9) into (3.10), we get:

$$\frac{P_0}{2} - \frac{P_0}{2}\cos\omega' t = C_s \frac{dT_s(t)}{dt} + \kappa\left[T_s(t) - T_b\right]; \quad \omega' = 2\omega \tag{3.11}$$

Comparing both sides of equation, we can see that we must have an AC and DC term on each side. Then the solution to $T_s(t)$ should look like:

$$T_s(t) = T_b + T_{off} + T_{ac}(t) \tag{3.12}$$

The difference between the temperature of sample and thermal bath is T_{off} and $T_{ac}(t)$, which are caused by the DC and AC components of the heating power. Putting equation (3.12) into (3.11), we get:

$$\frac{P_0}{2} - \frac{P_0}{2}\cos\omega' t = C_s \frac{dT_{ac}(t)}{dt} + \kappa\left[T_{ac}(t) + T_{off}\right] \tag{3.13}$$

Comparing the dc and ac terms separately, one can get:

$$\frac{P_0}{2} = \kappa T_{off} \tag{3.14}$$

$$-\frac{P_0}{2}\cos\omega' t = C_s \frac{dT_{ac}(t)}{dt} + \kappa T_{ac}(t) \tag{3.15}$$

Solving the above two equations, we get the expressions for the DC and AC component of the temperature difference between sample and thermal bath:

$$T_{off} = \frac{P_0}{2\kappa} \tag{3.16}$$

$$T_{ac}(t) = \frac{P_0}{2\kappa} \frac{1}{\sqrt{1+(\omega'\tau_s)^2}} \sin(\omega' t + \varphi) \tag{3.17}$$

where τ_s denotes the external time constant given by:

$$\tau_s = C_s / \kappa \tag{3.18}$$

and the phase angle φ is defined by:

$$\varphi = \sin^{-1}\left(\frac{1}{\sqrt{1+(\omega'\tau_s)^2}}\right) - \frac{\pi}{2} \tag{3.19}$$

The amplitude of the ac temperature oscillation of the sample is given by:

$$T_{ac} = \frac{P_0}{2\kappa} \frac{1}{\sqrt{1+(\omega'\tau_s)^2}} = \frac{T_{off}}{\sqrt{1+(\omega'\tau_s)^2}} \tag{3.20}$$

If $\omega'\tau_s \gg 1$, then equation (3.20) can be reduced to:

$$T_{ac} = \frac{P_0}{2\kappa} \frac{1}{\omega'\tau_s} = \frac{P_0}{4\omega C_s} \tag{3.21}$$

i.e.:

$$C_s = \frac{P_0}{4\omega T_{ac}} \tag{3.22}$$

Note that the condition $\omega'\tau_s \gg 1$ corresponds to $T_{ac}/T_{off} \ll 1$ (from equation (3.20)). The analysis above gave us the idea that if the frequency of the AC power, ω, is tuned so that it falls into the range of $\omega'\tau_s \gg 1$, or $T_{ac}/T_{off} \ll 1$, then the heat capacity of the sample can be determined by controlling the value of P_0 and ω, and measuring the value of T_{ac}.

3.3.2 Design of membrane based AC micro-calorimeter

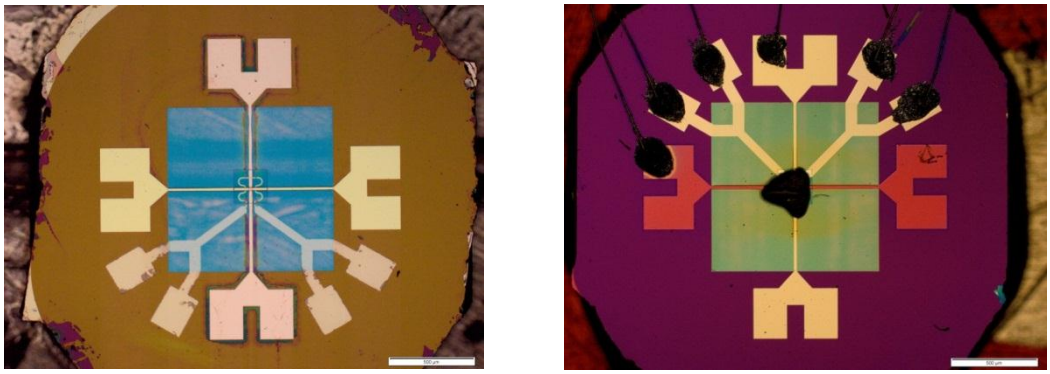

Fig 3.4 Front view of the membrane micro-calorimeter immediately after fabrication (left); Front view of the calorimeter with a sample mounted in the center and Au wires bonded to the contact pads for the heater and thermocouple (right).

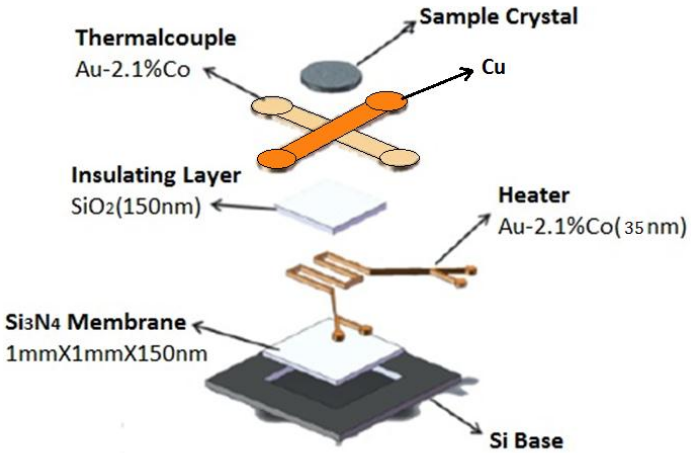

Fig 3.5 Expanded view of the micro-calorimeter: a 200 μm thick silicon base with a 150 nm thick thin layer of Si_3N_4 is back etched to produce a suspended membrane window of dimensions 1x1 mm^2. A thin film heater, a SiO_2 insulating layer and a thermocouple are patterned and deposited on top of the membrane. The sample is placed on top of the thermocouple with minute amount of Apiezon N grease [102].

The theoretical formulation in the previous section suggests that a sensitive calorimeter will require the following components: (i) a heat base to provide a stable bath temperature for the sample; (ii) an AC heater with well controlled power amplitude and frequency; (iii) a sensitive thermometer capable of detecting small temperature oscillations of the sample.

For the heat base and substrate, we chose a thin membrane of silicon nitride. The choice of Si-N membrane is due to its low thermal expansion coefficient which gives good thermal shock resistance, good high-temperature strength, creep resistance and oxidation resistance. Since the membrane is as thin as 150nm, the addendum heat capacity from it would be negligible.

For the AC heater, we use a sputtered thin film metallic layer of Au-2.1% Co patterned as a meandering strip. The thickness of the heater is around 35nm and the resistance of it is usually around 700 to 800 Ω. There is a meandering section of the heater with an area of 150 x 150 μm^2 located at the center of the Si_3N_4 membrane, which acts as the effective heating area. Wide contact lines connect this center region with four contact pads located on the Si substrate. Typical current sent to the heater is ~0.1 to 0.2 mA with a power ~10 μW driven at a frequency range of 15 – 100 Hz. The ideal sample size should be about the size of the meandering part of the heater (150 x 150 μm^2), and as thin as possible (typically ~10-30 μm) for best possible heat conductance. A 150 nm thick SiO_2 insulating layer covering an area of 200 x 200 μm^2 was sputtered on the top of the meandering heater to electrically separate the heater from the thermocouple. The amplitude

and frequency of the current through the heater is provided by the controlled output from a Stanford Research Lock-in amplifier (SR830).

For the thermocouples, choosing the right materials is critical to achieve high resolution and good functionality. Ultra-low noise measurements require transformer preamplifiers which cannot operate if the impedance of the thermocouples is too high. In our case, we use a sputtered thin film Au-2.1%Co and Cu thermocouple, which has a low resistance value of ~25 Ω and a Seebeck coefficient of ~ 42 μV/K at room temperature (Fig 3.6), to measure the AC temperature oscillation in the sample. Front side images of the membrane based micro-calorimeter without and with a sample on top are shown in Fig 3.4. A schematic showing the individual components of the calorimeter is shown in Fig 3.5.

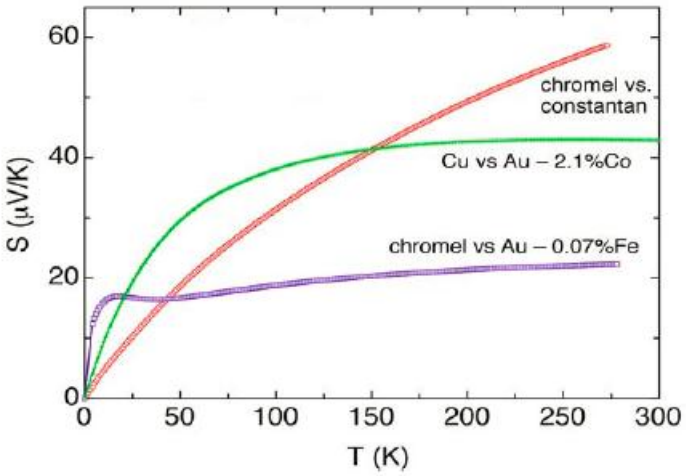

Fig 3.6 Seebeck coefficient versus temperature for three different thermocouples. The chromel/constatan and chromel/Au-0.07%Fe thermocouples both have high resistance values when compared to Cu/Au-2.1%Co thermocouple. From Ref [103].

One of the major disadvantages of this thermocouple based membrane micro-calorimeter is that the sensitivity becomes very low at low temperature since $S \to 0$ as $T \to 0$, which makes low-temperature specific heat measurements difficult. To overcome this problem, we have

developed a Ge/Au alloy based resistive thermometer that has high dimensionless sensitivity ($d\ln R / d\ln T$) even at low temperature. An image of the center of the 2nd generation micro-calorimeter with this resistive thermometer incorporated is shown in Fig 3.7:

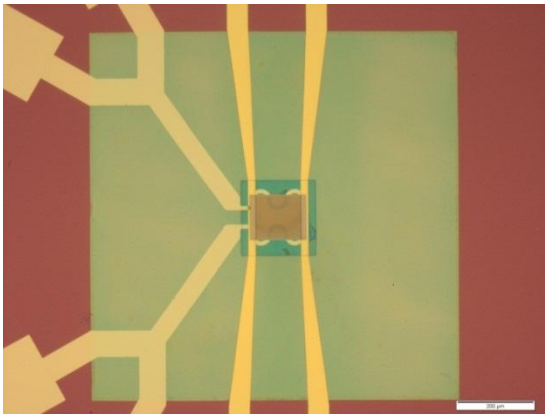

Fig 3.7 second generation membrane based micro-calorimeter with the Ge/Au resistive thermometer (120mm x 80 mm x 100 nm) in replacement of the original Au-2.1%Co thermalcouple.

The resistance of a test Ge/Au alloy based resistance thermometer as a function of temperature is given in Fig 3.8. The dimensionless sensitivity of the thermometer as deposited and annealed on a hotplate at 160 ^{o}C for 1 hour is shown in Fig 3.9. Its temperature sensitivity approaches that of commercially available Cernox temperature sensors.

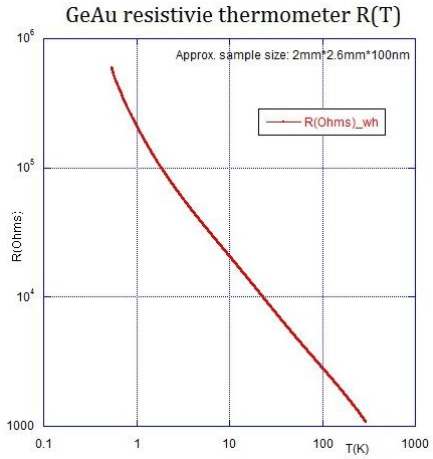

Fig 3.8 Resistance versus temperature of a test GeAu alloy resistive thermometer on log-log scale.

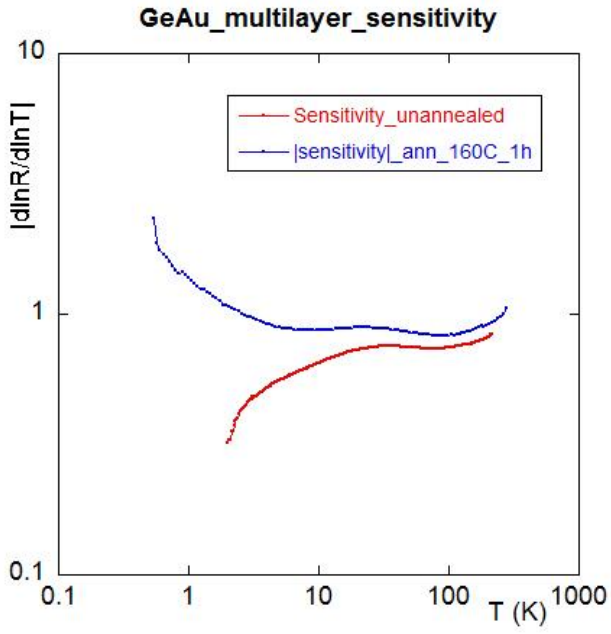

Fig 3.9 Dimensionless sensitivity of as deposited and annealed GeAu thermometer as a function of temperature.

A novel wafer based semiconductor fabrication process has also been developed for fabricating both the first and second generation membrane calorimeters with high efficiency. With this new process, the cost and time for fabrication is significantly reduced and the yield from one round of fabrication is also significantly enhanced.

3.3.3 Calorimetric measurements

The micro-calorimeter was mounted onto a Cu-plate with silver epoxies. This Cu-plate is then placed in the slot in the center of a circuit board with vacuum grease (Apiezon N). Gold wires with diameters of 25μm and 50μm are then used to connect the electrical contact pads on the SiN membrane to the contact pads on the circuit board with silver epoxy (type: H20E). The circuit

board or chip is then attached to the end of a probe and electrical connections between the probe and the circuit board is made by plugging in the 18-pin male connector from the probe to the female connector on the circuit board. An image of the bottom of the probe with the calorimeter mounted is shown in Figure 3.10.

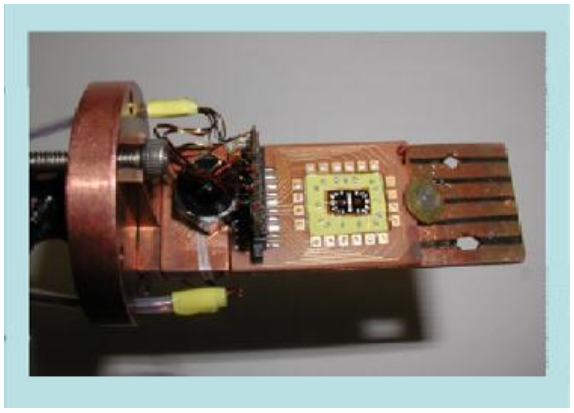

Fig 3.10 Bottom part of the specific heat probe showing the circuit board with the calorimeter in the center

The amplitude and frequency of the current sent through the heater is controlled by the output of a Stanford Research Lock-In amplifier (SR830). The base temperature of the Cu-block where the chip (circuit board containing the calorimeter cell) is attached is controlled and measured by a LakeShore 340 Temperature Controller and a Cernox thermometer. The signal from the thermocouple related to T_{ac} is amplified 1:100 by a Stanford Research Transformer (SR554) followed by a 1:1000 Stanford Research Preamplifier (SR560). See Figure 3.11 below for a schematic of the measurement setup.

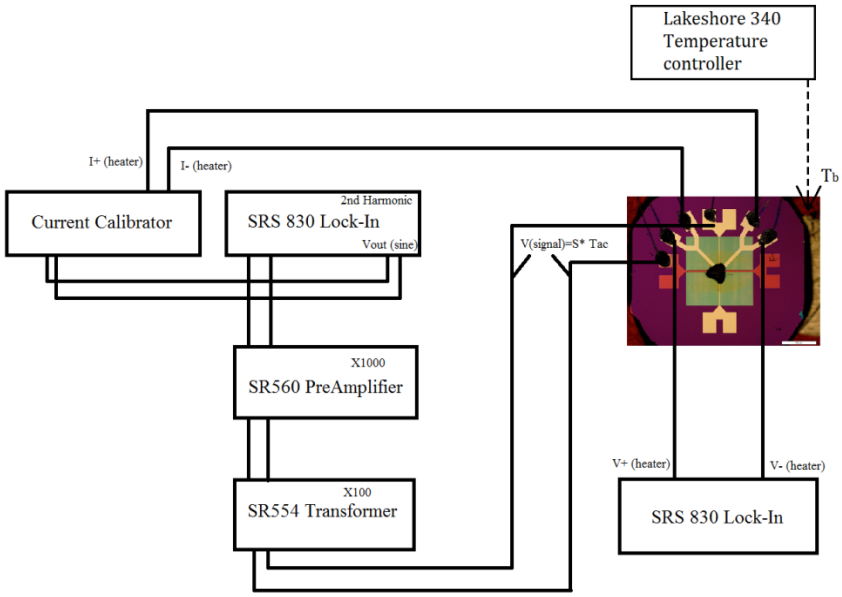

Fig 3.11 Schematic showing the specific heat measurement setup

All the instruments used in the measurements are connected using GPIB cables to a computer with LabVIEW installed. Several LabVIEW programs have been developed to automate the control of instruments and data acquisition. Fig 3.12 shows a photo of the user interface for one of the LabVIEW programs which is capable of measuring the specific heat as a function of temperature with preset applied magnetic field and field angle sequence.

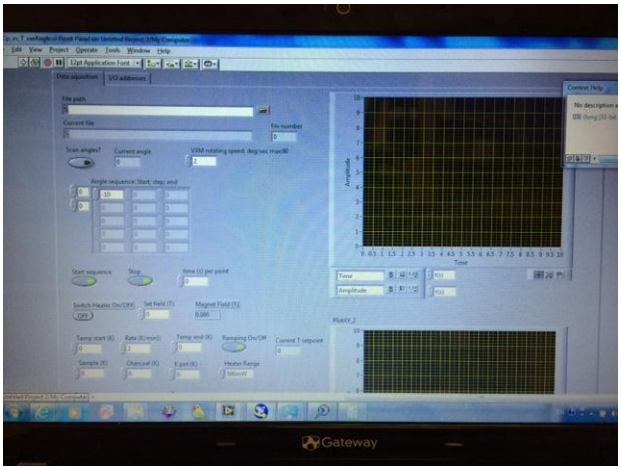

Fig 3.12 User interface of LabVIEW program for heat capacity measurements

From section 3.1 we know that $T_{off} = \frac{P_0}{2\kappa}$, so T_{off} depends on the amplitude of the heater power and the coupling between sample and base (copper block). By tuning the amplitude of the heater power, we can change the offset temperature. Usually we keep T_{off} ~ 0.2 – 0.5K. Now we need to set the measuring frequency to satisfy the condition $T_{ac} / T_{off} \ll 1$. In order to find the correct operating frequency, we perform a frequency scan of the calorimeter at a fixed temperature. A typical frequency scan is shown in Figure 3.13 below:

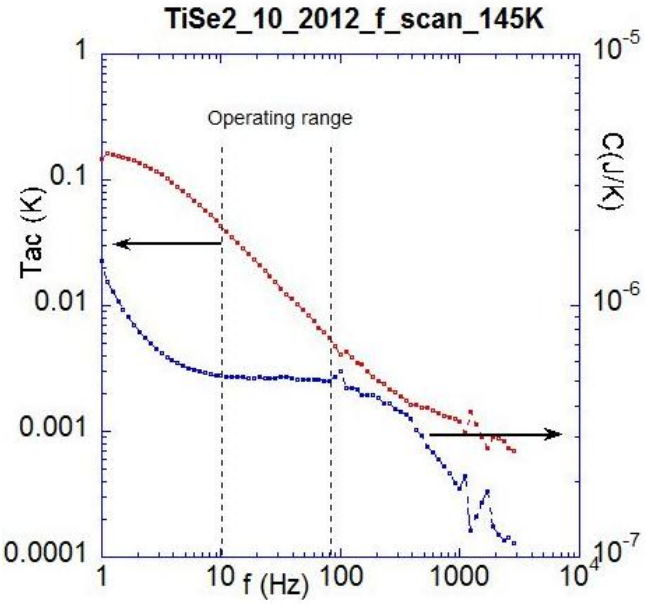

Fig 3.13 Log-log plot of the amplitude of the ac temperature oscillation and the heat capacity defined by (3.22) vs. frequency from a $TiSe_2$ single crystal on top of the calorimeter. The heater power amplitude is kept constant.

As we can see from the figure, when the frequency of the AC current is in the range of 10 - 100Hz, the AC temperature response of the sample, T_{ac} is inversely proportional to the frequency. This is the correct frequency range to maintain $T_{ac} / T_{off} \ll 1$. If this condition holds,

$C_s = \frac{P_0}{4\omega T_{ac}} = \frac{P_0}{4(2\pi f)T_{ac}}$. When plotted on log-log scale, the dependence of T_{ac} on f will be a linear line with a slope of -1. At lower frequencies, T_{ac} is nearly constant. This can be explained by looking at equation (3.20), when f (or ω) is small enough, $T_{ac} \approx T_{off}$, while $T_{off} = \frac{P_0}{2\kappa}$ is independent of frequency. At higher frequencies, $f \sim 100 - 1000\text{Hz}$, the response from the sample starts to slow down so the slope of T_{ac} vs. f becomes smaller. When the frequency is higher than 1000 Hz, the signal from the sample quickly diminishes until it becomes undetectable because at such a high frequency, the sample basically lose coupling to the calorimeter. Hence, for this particular sample, the operating frequency range is $f \approx 10 - 100Hz$ and it is marked by a linear slope of T_{ac} and a plateau in heat capacity in the T_{ac} and C vs. f plot (log-log scale) at fixed temperature.

3.3.4 More rigorous model and calorimeter calibration

The model we discussed in section 3. 1 is a simplified model of the membrane calorimeter which is useful to describe the system but is slightly oversimplified. In particular, we ignored the heat capacity of the thermocouples, the supporting SiN membrane underneath the thermocouple and the thermal link between the sample and the thermocouple. Here, we include all these effects and discuss the results below.

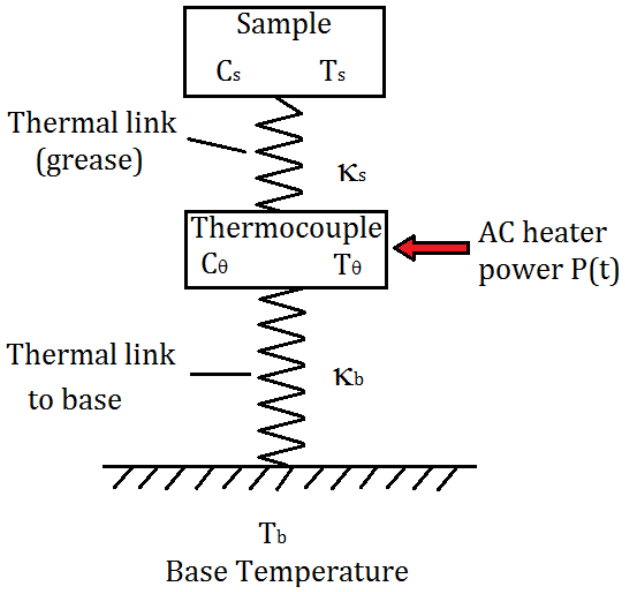

Fig 3.14 Schematic diagram of the more rigorous model of the calorimeter, the effects of the heat capacity of the thermocouple (heat capacity of the section of membrane support the thermocouple included) and the thermal link between sample and thermocouple are included [104].

The heat balance equations for this updated model system are:

$$C_s \frac{dT_s}{dt} = \kappa_s (T_\theta - T_s) \tag{3.23}$$

$$P(t) = C_\theta \frac{dT_\theta}{dt} + \kappa_b (T_\theta - T_b) + \kappa_s (T_\theta - T_s) \tag{3.24}$$

Substituting the expression for T_θ, equation (3.23) into equation (3.24), we get:

$$P(t) = C_\theta \frac{C_s}{\kappa_s} \frac{d^2 T_s}{dt^2} + \left[C_\theta + \frac{\kappa_b}{\kappa_s} C_s + C_s \right] \frac{dT_s}{dt} + \kappa_b (T_s - T_b) \tag{3.25}$$

The expression for the AC power input is still the same as in the previous model:

$$P(t) = I^2(t)R = \frac{P_0}{2}\left[1 - \cos 2\omega t\right] \tag{3.26}$$

Similarly, we can guess the form of the solution for T_s as:

$$T_s = A + B\cos(2\omega t + \varphi) \tag{3.27}$$

where A is a constant or dc part of T_s, and B is the amplitude of the ac temperature oscillation, i.e. T_{ac}, φ is the phase angle of the ac oscillation.

Substituting equations (3.26) and (3.27) into equation (3.25), we obtain:

$$\frac{P_0}{2} - \kappa_b(A - T_b) = \cos(2\omega t)\left[\frac{P_0}{2} + B\cos\varphi\cdot(\kappa_{\mathrm{b}} - 4\omega^2 C_\theta\frac{C_s}{\kappa_s}) - 2B\omega\sin\varphi\cdot(C_\theta + \frac{\kappa_{\mathrm{b}}}{\kappa_s}C_s + \mathrm{C_s})\right]$$
$$\text{-}\sin 2\omega t\left[B\sin\varphi\cdot(\kappa_{\mathrm{b}} - 4\omega^2 C_\theta\frac{C_s}{\kappa_s}) + 2\,\mathrm{B}\,\omega\cos\varphi(C_\theta + \frac{\kappa_{\mathrm{b}}}{\kappa_s}C_s + \mathrm{C_s})\right] \tag{3.28}$$

Equating the DC and AC parts on both sides of the equation, we get:

$$\frac{P_0}{2} - \kappa_b(A - T_b) = 0 \tag{3.29}$$

$$\frac{P_0}{2} + B\cos\varphi\cdot(\kappa_{\mathrm{b}} - 4\omega^2 C_\theta\frac{C_s}{\kappa_s}) - 2B\omega\sin\varphi\cdot(C_\theta + \frac{\kappa_{\mathrm{b}}}{\kappa_s}C_s + \mathrm{C_s}) = 0 \tag{3.30}$$

$$\sin\varphi\cdot(\kappa_{\mathrm{b}} - 4\omega^2 C_\theta\frac{C_s}{\kappa_s}) + 2\omega\cos\varphi(C_\theta + \frac{\kappa_{\mathrm{b}}}{\kappa_s}C_s + \mathrm{C_s}) = 0 \tag{3.31}$$

From equation (3.29), we get the solution for A:

$$A = \frac{P_0}{2\kappa_b} + T_b \tag{3.32}$$

As I have pointed out in equation (3.27), A is the DC component of the temperature of the sample. This result is the same as what was obtained earlier for the simplified model: The elevation of temperature with respect to the base temperature is equal to the average power divided by the thermal link between the base and the thermocouple.

From equation (3.20) and (3.21), we obtain the expression for the sample heat capacity:

$$C_s = \frac{P_0}{4\omega B}\frac{1}{\sqrt{\left(\frac{1}{2\omega\frac{C_s}{\kappa_b}} - 2\omega\frac{C_\theta}{\kappa_s}\right)^2 + \left(1+\frac{\kappa_b}{\kappa_s}+\frac{C_\theta}{C_s}\right)^2}} = \frac{P_0}{4\omega B}\frac{1}{\sqrt{\left(\frac{1}{2\omega\frac{C_s}{\kappa_b}}\right)^2 + \left(2\omega\frac{C_\theta}{\kappa_s}\right)^2 + \left(\frac{C_\theta}{C_s}\right)^2 + 2\frac{C_\theta}{C_s} + \left(1+\frac{\kappa_b}{\kappa_s}\right)^2}} \tag{3.33}$$

Knowing the typical values of κ_b, κ_s , *and* C_θ, and estimating C_s for the materials to be measured, it can be shown that some of the fractions in the denominator of Equation (3.33) would be much smaller or equal to unity in such a way that for this model C_s can be approximated as:

$$C_s = \frac{P_0}{4\omega T_{ac}}\frac{1}{2} \tag{3.34}$$

Using this factor in combination with the fact that the power received by the sample is ~3/4 times of the power applied, the measured heat capacity will be 8/3 times larger than the actual value:

$$C_s = \frac{P_0}{4\omega T_{ac}}\frac{3}{8} \tag{3.35}$$

We can see that the specific heat we measured by using equation (3.22) are off by a factor of ~2. In order to find out the exact of value of this correction factor, we calibrate our specific heat measurements by measuring a standard gold reference sample with a known literature value [105]. By scaling our measurement data to the standard data we determine this correction factor to be ~2, which is quite close to the value of 3/8 from equation (3.35). Each membrane calorimeter was individually calibrated against a standard gold foil, so all the measurements presented in this thesis have been corrected by this particular factor. See Fig 3.15 for an example calibration data of one of our membranes with a gold sample.

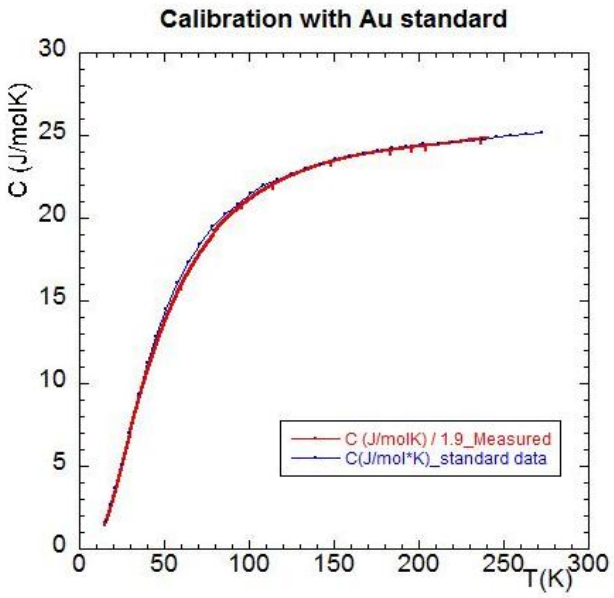

Fig 3.15 Plot of the measured specific heat of a Au standard sample after a correction factor of 1.9 (red) and the literature specific heat data [105] of the sample (blue).

3.3.5 Helium-3 Cryostat System

The cryostat used in our experiments was built by Cryo-Industries and is a top-loading ^{3}He system designed to achieve temperatures ranging from as high as room temperature (300K) to as low as 0.3 K. The tail of the cryostat is placed in the bore of a transverse 8 Tesla superconducting magnet from American Magnetics, Inc. Both the ^{3}He-cryostat and the magnet reside in a super-insulated liquid ^{4}He dewar. A stepper motor bolted at the top of the cryostat allows rotation of the sample probe and the load lock by 360^o horizontally. A load lock is attached to the top of the 3He cryostat with an isolation valve so that the sample space of the ^{3}He cryostat is maintained in vacuum when loading and unloading samples. A schematic of the cryostat is shown in Fig 3.16.

Cooling the sample is achieved through the following procedure: First, the sample probe is inserted into the load lock on top of the cryostat. Then the load lock is pumped down to a pressure of below 10^{-5} Torr by a portable pump station. Then the isolation valve between the load lock and the sample space of the ^{3}He cryostat is opened and the sample probe is slowly lowered into the cryostat. Once the bottom of the probe, where the calorimeter sits reaches the center of the horizontal superconducting magnet, the top of the probe can be locked to the top of the load lock by two screws and four nuts. To cool down the probe, ^{3}He gas is then released into the sample space either from an external ^{3}He gas storage tank that is connected to the sample space or by heating up charcoal sorption pump to release previously absorbed ^{3}He gas. The ^{3}He cryostat consists of a 1K pot which is in direct contact with the outer wall of the sample chamber and draws liquid Helium from the reservoir in the dewar through a capillary tube (see Fig 3.17). Filling the 1K pot with liquid helps cool the sample probe to nearly 4.2 K. Pumping on the ^{4}He gas vapor 1K pot with an external pump reduces the vapor pressure of liquid ^{4}He in the 1K pot ,which further lowers the temperature to ~1.5 K. At this temperature, ^{3}He gas condenses on the part of the inner wall of the sample chamber which is directly connected to the 1K pot and immerses the tip of the sample probe. The charcoal sorption pump operates by cooling the charcoal by drawing liquid ^{4}He from the dewar in a similar manner as that of the 1K pot, through

a second capillary tube. Lowering the temperature of charcoal greatly enhances its absorbing capability. The absorbed gas can be later be released by heating the charcoal with a provided heater attached to its container. We use the charcoal sorption pump to reduce the vapor pressure of liquid ^{3}He in the sample chamber which allows us to reach a base temperature close to ~300 mK. The low temperature retention time is about two hours with around 30 ml of L^{3}He in the bottom of the sample chamber. Once liquid ^{3}He has completely evaporated, we can repeat the process by heating the charcoal to release ^{3}He gas back into the sample chamber provided that the 1K pot is full and being pumped. By controlling the temperature of the 1K-pot and the charcoal pot, the temperature of the ^{3}He exchange gas can be adjusted. Furthermore, by adjusting the power of the heater on the sample holder, the temperature of the sample can be tuned from 0.3K to 300K.

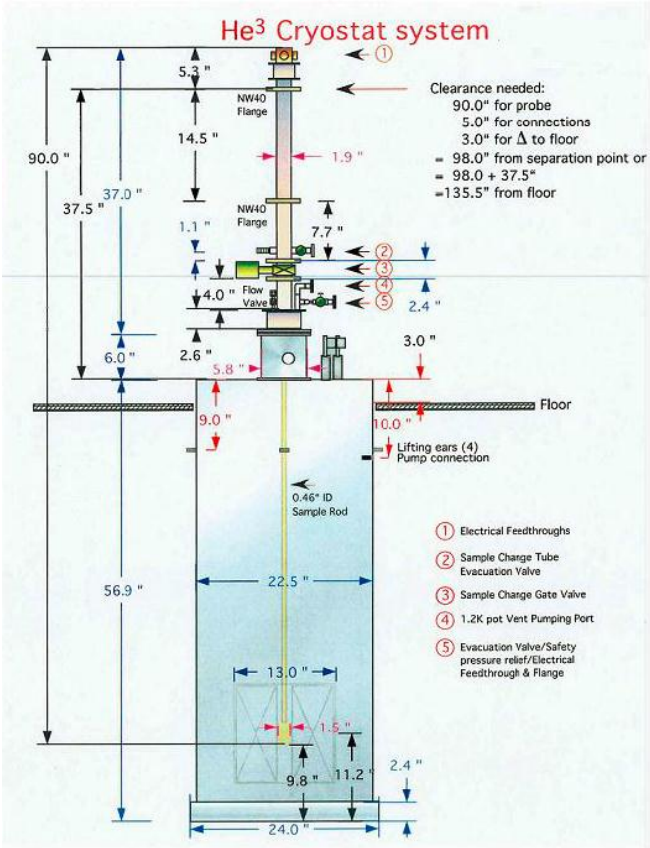

Fig 3.16 Schematic of the ^{3}He cryostat with dimensions.

The system is designed to perform both temperature sweep and field sweep measurements. To do so, we simply cool the sample down to the desired temperature first. The desired sample temperature can be stabilized by balancing the cooling power from the 1K pot and charcoal sorption pumps and the heating power from the resistive heater on the sample holder. The orientation of the sample with respect to the magnetic field is adjusted by using the stepper motor via a LabVIEW control program. The stepper motor provides angle resolution of 0.015 degrees/step. For temperature sweep measurements, the temperature ramp rate is controlled via a Lakeshore temperature controller and the temperature sweep rate can be as small as 0.1K/minute. For our heat capacity measurements, we use a typical ramp rate of 0.2K/minute.

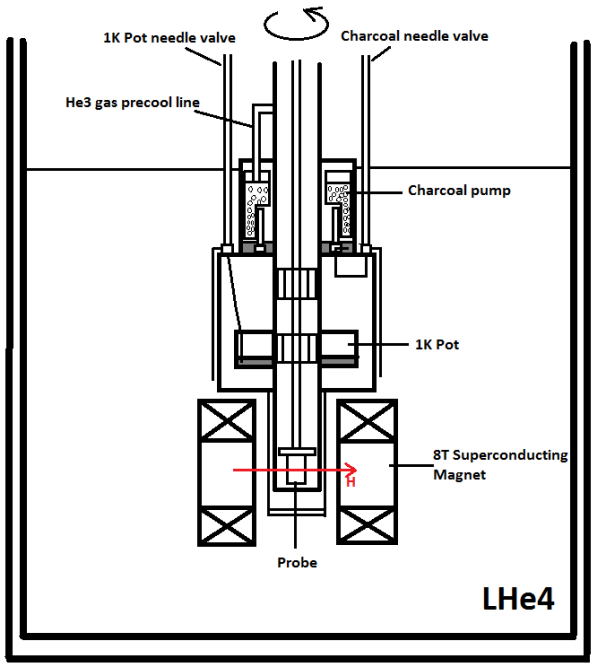

Fig 3.17 Bottom part of the ^{3}He cryostat showing the details of the 1K pot and charcoal sorption pump.

Chapter 4

Study of nematic and antiferromagnetic transitions in Fe-based superconductors

4.1 Introduction and overview

The phase diagrams of one of the most studied Fe-based superconducting system, namely the "122" system, have been introduced in section 1.2. Starting from the antiferromagnetic parent compound $BaFe_2As_2$, one can systematically dope either Ba with K, Fe with Co or Ni, or As with P to suppress antiferromagnetism (AFM) and a superconducting dome emerges in the phase diagram. Among these three systems the iso-valent P-doped Ba122 system has attracted the most attention recently due the discovery of a "true" nematic phase transition line in the phase diagram by magnetic torque and high resolution XRD experiments [61].

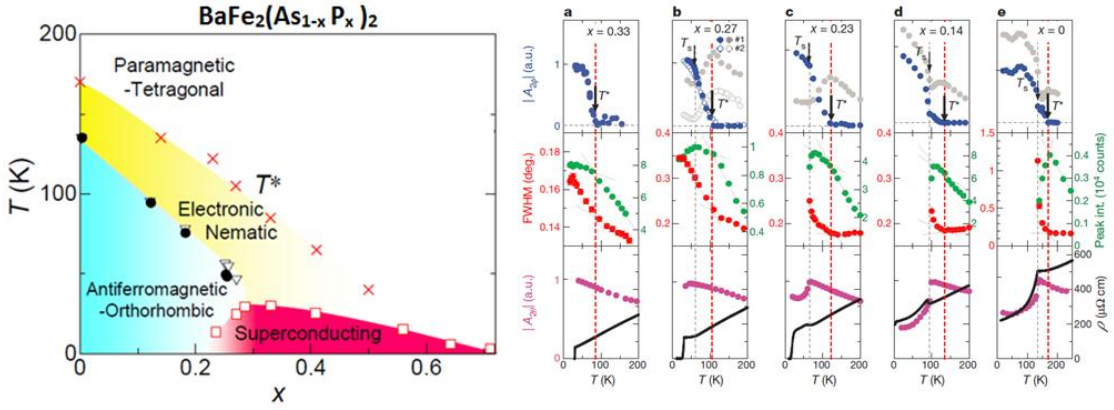

Fig 4.1 T-doping phase diagram after addition of the true nematic phase transition line (left); Measurement data from magnetic torque, high-resolution XRD and resistivity with red lines

marking the true nematic phase transition temperatures for five different doping levels of $BaFe_2(As_{1-x}P_x)_2$.[61]

Conventionally the structural transition which usually precedes or is coincident with the AFM transition in the temperature-doping phase diagram of "122" system has been regarded as a nematic phase transition due to experimentally observed unusually large electronic anisotropy either in resistivity, optical conductivity, or orbital occupancy in order to separate it from a conventional phonon (lattice vibration) driven structural transition. However, recent magnetic torque measurements on $BaFe_2(As_{1-x}P_x)_2$ [61] and $EuFe_2(As_{1-x}P_x)_2$ [62] single crystals under in-plane magnetic field rotation revealed breaking of the tetragonal symmetry at a temperature T^* more than 30K above the conventional nematic/structural transition at T_S. The 2nd order phase transition at T^* is now regarded as the "true" nematic phase transition while the structural transition ceases to be a true phase transition but is regarded as a meta-nematic transition.

Measurements of the strain dependent resistivity anisotropy [46] (Fig 4.2) or of the shear modulus [64] (Fig 4.3) of $BaFe_2As_2$ shows strong divergence of the nematic susceptibility at the structural transition with a long tail which extends to much higher temperatures. This give evidence for strong nematic fluctuations right above the structural transition T_s and leads to the updated nematic phase diagram for FeSCs with an extra region of strong nematic fluctuations (Fig 4.4). However, no evidence was found for another phase transition above the existing nematic/structural transition.

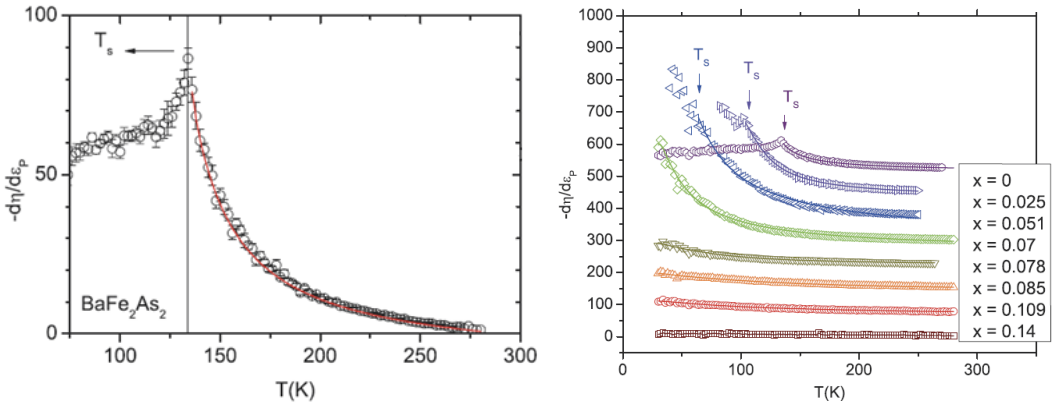

Fig 4.2 measurements of the strain dependent resistivity anisotropy, a quantity which is proportional to the nematic susceptibility. Strong divergence of the nematic susceptibility is found at T_s, with a Curie-Weiss shaped long tail indicative of nematic fluctuations extending to temperatures as high as room temperature. The left figure shows data for the parent compound while the right figure shows data for various doping levels of $Ba(Fe_{1-x}Co_x)_2As_2$ [46].

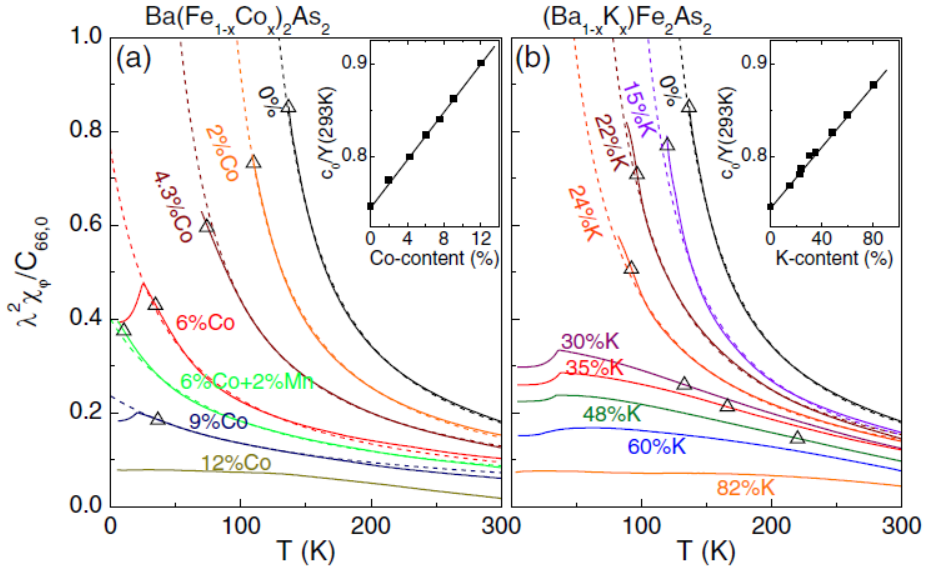

Fig 4.3 Nematic susceptibility, expressed in unit of $C_{66,0}/\lambda^2$ where $_{C66,0}$ is the temperature independent elastic constant and λ is the electron-lattice coupling strength, plotted as a function of temperature. Strong divergence is seen at T_s for both $Ba(Fe_{1-x}Co_x)_2As_2$ and $Ba_{1-x}K_xFe_2As_2$ [64].

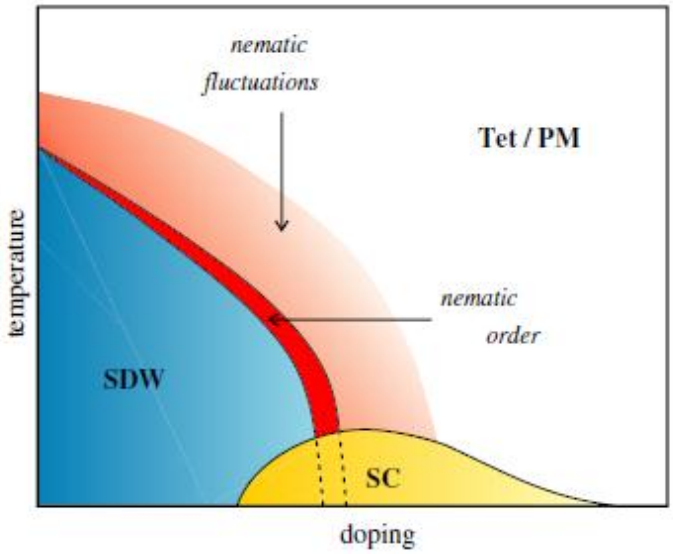

Fig 4.4 Nematic phase diagram of $BaFe_2(As_{1-x}P_x)_2$ or $Ba(Fe_{1-x}Co_x)_2As_2$ [57]

A recent STM/STS study on NaFeAs single crystals [65] revealed the persistence of local electronic nematicity up to temperatures of almost twice T_S. In this case, residual strains in the sample in conjunction with a large nematic susceptibility were considered as possible origin of such symmetry breaking. Similarly, recent inelastic neutron scattering experiments shows change in the low energy spin excitations in uniaxially strained $BaFe_{2-x}T_xAs_2$ (T=Co or Ni) from four fold to two fold symmetry at temperatures (T^*) corresponding to the onset of in-plane resistivity anisotropy observed previously [66]. However, the authors also emphasized the effects from the uniaxial strain they applied which rendered the structural transition at T_S a crossover and T^* only marks a typical range of nematic fluctuations [66]. Nevertheless, magnetic torque is directly related to the spin nematic order parameter [57] possibly facilitating the observation of a nematic

phase transition. Thus, the question whether the phenomena at T^* represent a 2nd order phase transition, a cross-over associated with the onset of sizable short-range correlations and fluctuations, or spurious effects due to frozen-in or applied strains remains unresolved.

Here we present a study of single crystal $BaFe_2(As_{1-x}P_x)_2$ by high resolution ac micro-calorimetry [106] and SQUID magnetometry to investigate the various phase transitions and to explore the "true" nematic phase transition. If another 2nd order true nematic phase transition does exist more than 30K above the structural transition, we should see a corresponding feature in the specific heat since specific heat is a direct thermodynamic probe of any phase transitions.

4.2 Experimental results

High quality $BaFe_2(As_{1-x}P_x)_2$ crystals were grown by the self-flux method as described elsewhere [107]. Annealing of as-grown $BaFe_2As_2$ was carried out in an evacuated quartz tube together with BaAs flux at 800 ^oC for 72 hours [108]. High resolution specific heat measurements were performed with our home built membrane-based ac micro-calorimeter. Single crystal samples of $BaFe_2As_2$, with dimensions of $\sim 120 \times 110 \times 20\ \mu m^3$ for the as-grown and $\sim 130 \times 180 \times 13\ \mu m^3$ for the annealed sample, respectively, were mounted onto the calorimeter with minute amount of Apiezon N grease.

Fig 4.5 shows the temperature dependence of the specific heat for both as-grown and annealed $BaFe_2As_2$ samples from 100K to 220K. Fig 4.6 shows the magnified peak region of the original data for as grown and annealed samples. For the as grown $BaFe_2As_2$, a sharp peak is distinguished at 133K with a relative peak height of $\Delta C/C \sim 37\%$ and a width of only 1.2K (FWHM), which signifies the simultaneous AFM and tetragonal to orthorhombic structural transitions in this parent compound of the 122 family. The sharpness of the peak, combined with the step-like feature in the entropy as shown later, seem to suggest the first order nature of this

combined phase transition. This agrees with previous results from heat capacity and synchrotron XRD measurements of C. R. Rotundu et al [109] and neutron diffraction from S. Avci et al [41]. The peak associated with the AFM/structural transition shifts to a higher temperature of 137K for the annealed $BaFe_2As_2$, with a relative height of $\Delta C/C$ ~69% and a width of 0.7K. Interestingly the shape of peak becomes λ-like rather than approximately symmetric after annealing. This might be a direct consequence of improvement in sample quality by annealing, which was found to increase the transition temperature gradually [109]. The absolute values of the peak height, in $\Delta C/T_N$, are about 0.3 J/mol K^2 and 0.5 J/mol K^2 for as grown and annealed $BaFe_2As_2$, consistent with a previous reported value of 0.3 J/mol K^2 at a transition temperature of 138K for a high quality sample [110].

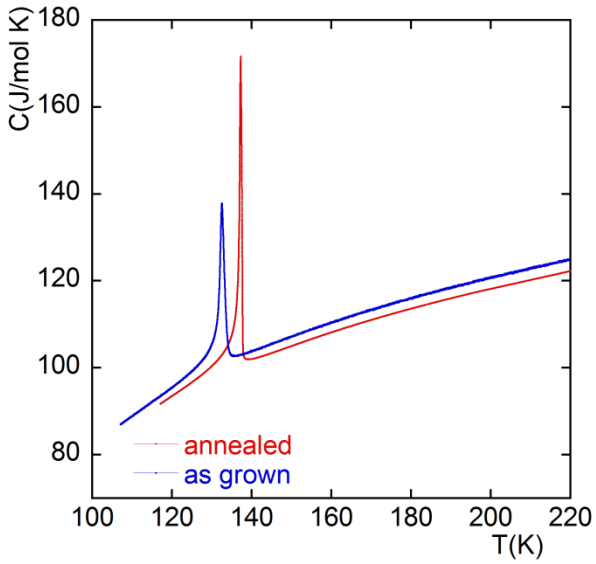

Fig 4.5 Temperature dependence of the specific heat of as-grown and annealed $BaFe_2As_2$ single crystals.

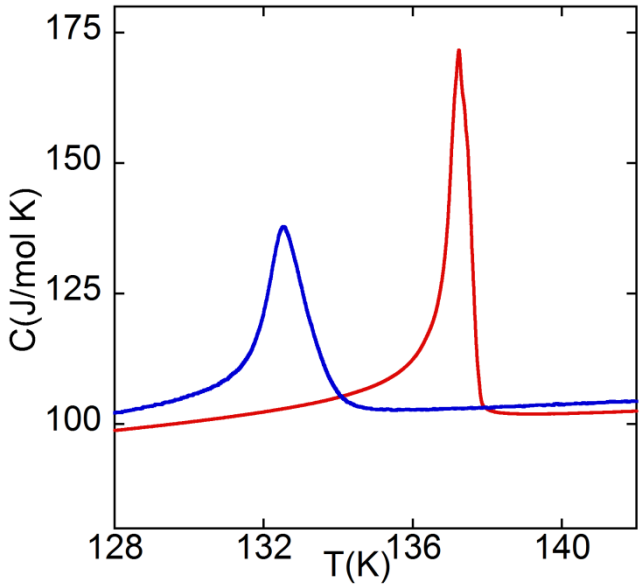

Fig 4.6 Peak regions of the specific heat of as grown (blue) and annealed (red) $BaFe_2As_2$.

Integrating *C/T* over temperature yields the change in entropy across the transition as shown in Fig 4.7. A clear step-like anomaly is discernible at the AFM/Structural transitions of both samples. The detailed shape of the anomaly is shown in Fig 4.8 obtained by subtracting a normal state background from the original entropy. The change in entropy at the transition, extracted by approximating the transition as a sharp step, amounts to ~0.5 J/mol K, or 0.06 k_B per formula unit, for both as-grown and annealed $BaFe_2As_2$. This value is slightly smaller than ~0.84 J/mol K reported for an annealed crystal with a transition temperature of 140 K [109]. The change in entropy across the AFM transition is substantially smaller than the value of $R\ln(2)$ expected for the onset of long-range magnetic order in a *S*=1/2–system, indicative of pronounced magnetic fluctuations [95]. The shape of the *C/T* - and *S* - curves, particularly of the as-grown sample, is consistent with a broadened first order transition as well as with a second order magnetic transition accompanied by critical fluctuations [112]. However, for our annealed sample a clear kink in *S(T)* is seen near the top of the transition about 0.5 K above the peak temperature in the specific heat, followed by a tail towards high temperatures. Such behavior is not expected for

critical fluctuations, and may instead indicate two transitions, namely a second order transition preceding a first order transition by approximately 0.5 K. Similar results have been reported in recent X-ray diffraction and X-ray resonant magnetic scattering studies on as-grown $BaFe_2As_2$ [59], where they found a second order structural transition and a first order AFM transition separated by approximately 0.75 K.

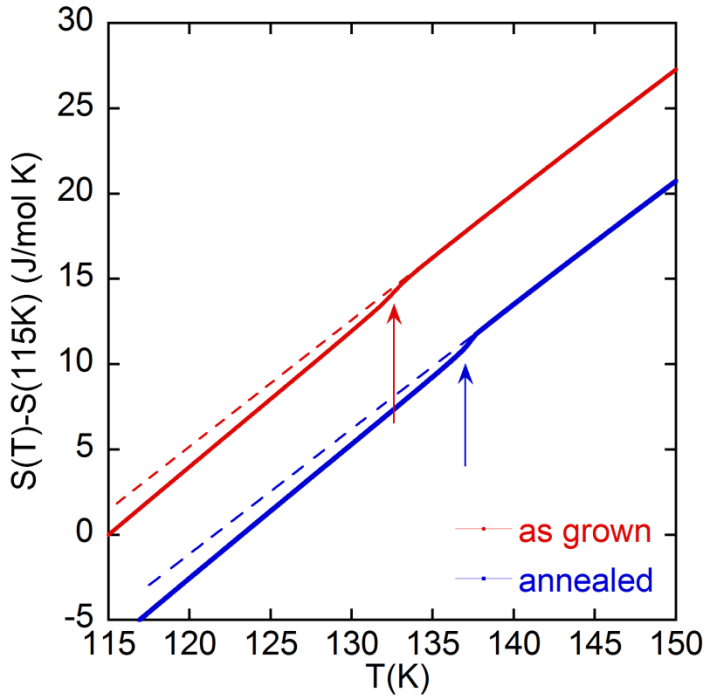

Fig 4.7 Temperature dependence of the entropies of as grown and annealed $BaFe_2As_2$. Dashed lines in the main panel indicate extrapolations of the normal state entropy. Blue and red arrows indicate the AFM/structural transitions.

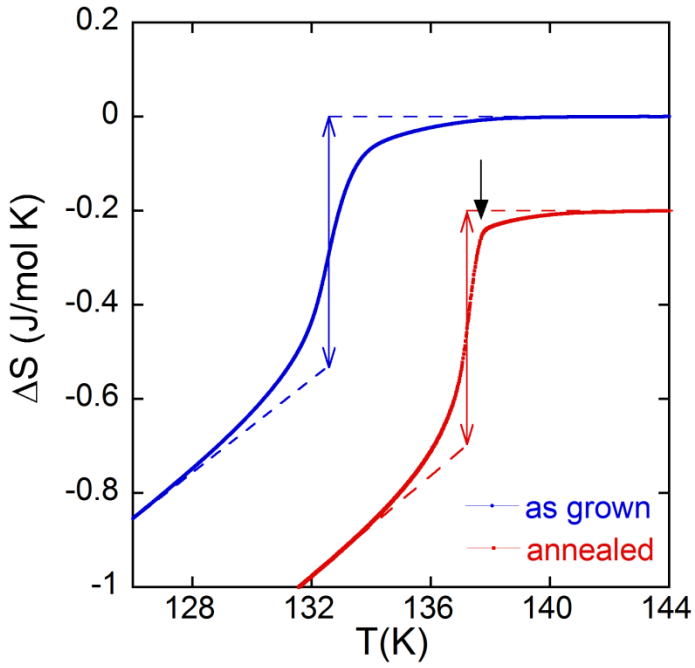

Fig 4.8 Temperature dependence of the entropy of as grown and annealed $BaFe_2As_2$, after subtraction of a smooth normal state background indicated by the dashed lines Fig 4.7, respectively. The data for the annealed sample is shifted downward slightly to assist the eye. The dashed lines and double headed arrows demonstrate the construction used for extracting the entropy steps at the transitions. The black arrow indicates the position of the kink in the entropy of the annealed $BaFe_2As_2$, and the double-headed arrows mark the location of the maxima in the specific heat.

We also measured the specific heat of near optimum doped $BaFe_2(As_{1-x}P_x)_2$ (x=0.3) crystal with dimensions of 113 x 154 x 22 μm^3 from 15K to 120K. The result is shown below in Fig 4.9.

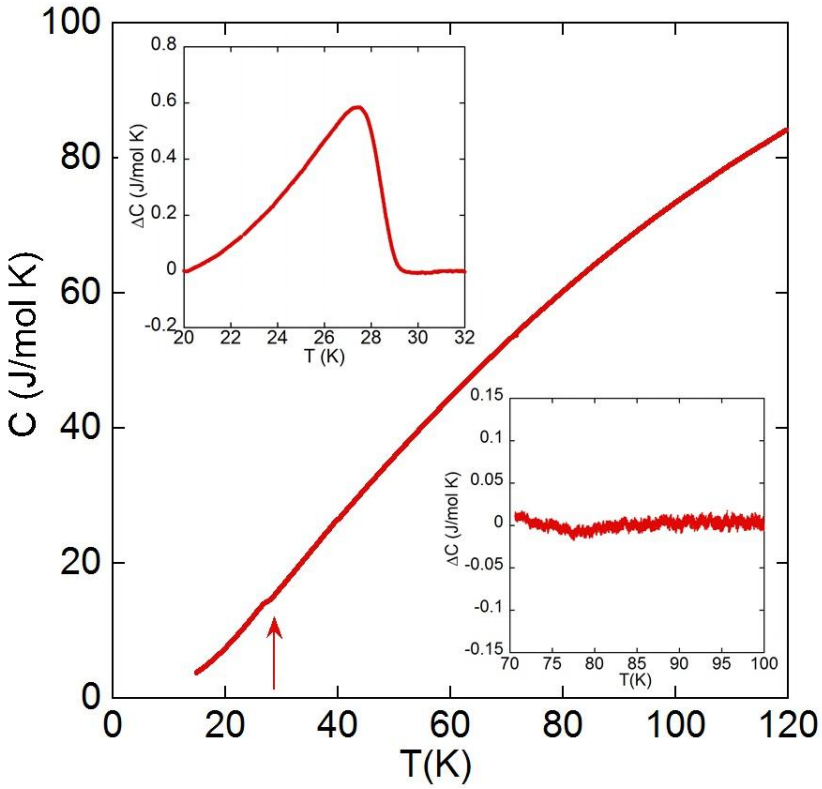

Fig 4.9 Temperature dependence of the heat capacity of $BaFe_2(As_{0.7}P_{0.3})_2$. Upper inset shows a magnification of the SC transition region. Lower inset is a magnification of the temperature region where the nematic transition is expected to occur. The level of resolution is about 10^{-4}. The kink-like feature at around 77 K is an artifact due to the condensation of minute amounts of N_2 gas in certain areas of the cryostat.

Substracting a polynomial (third order) normal state background from the raw data, we can look at the superconducitng transition more closely in the upper inset of Fig 4.9. The superconducting T_c for this particular sample is around 29K taking the onset as the criterion.

Fig 4.10 and the lower inset of Fig. 4.9 show the specific heat for $BaFe_2As_2$ and $BaFe_2(As_{0.7}P_{0.3})_2$ under high magnification after subtraction of a smooth polynomial background. Within our resolution of 10^{-4}, no feature can be identified that would indicate a phase transition near the

expected nematic transition temperatures of 170 K and 90 K of the parent compound and optimally doped sample, respectively.

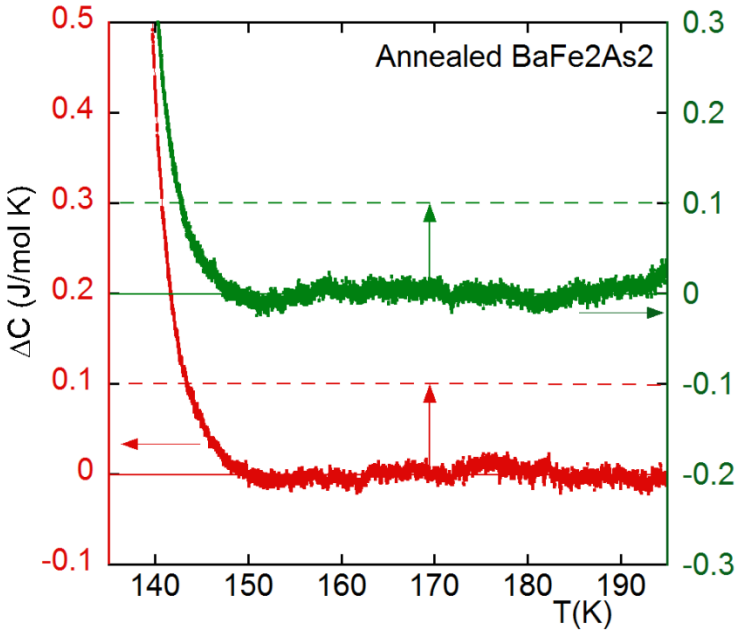

Fig 4.10. The specific heat of annealed $BaFe_2As_2$ after a background subtraction for the temperature region above the peak. Red and green curves correspond to warming and cooling runs, respectively. Dashed lines indicate the level of the anomaly expected on the basis of the GL-model. Data are off-set by 0.2 J/mol K for clarity of presentation.

We evaluate the expected specific heat signature at the nematic transition using the GL free energy for $BaFe_2As_2$ as given in Ref [61]:

$$F[\delta,\psi]=\left[t_s\delta^2-u\delta^4+v\delta^6\right]+\left[t_p\psi^2+w\psi^4\right]-g\delta\psi \qquad (4.1)$$

Here $\delta=\frac{a-b}{a+b}$ denotes the lattice distortion and ψ is the nematic order parameter. $t_{s,p}=\frac{T-T_{s,p}^{(0)}}{T_{s,p}^{(0)}}$ is the reduced temperature of the structural/nematic transitions, with $T_{s,p}^{(0)}$

denoting the transition temperatures in the absence of coupling between the two order parameters, i.e. $g = 0$. The coefficients *u*, *v*, and *w* are determined in Ref [61] from fits to the torque and XRD data on a $BaFe_2As_2$ crystal with a transition temperature very close to the one investigated here. This GL model yields a 2nd order nematic phase transition at $T^* > T_p^{(0)}$ and a meta-nematic transition at $T_s > T_s^{(0)}$. By using the same model, we derive the temperature dependence of the free energy *F*(*T*), entropy *S*(*T*) and specific heat *C*(*T*). The latter two are shown in Fig 4. 11.

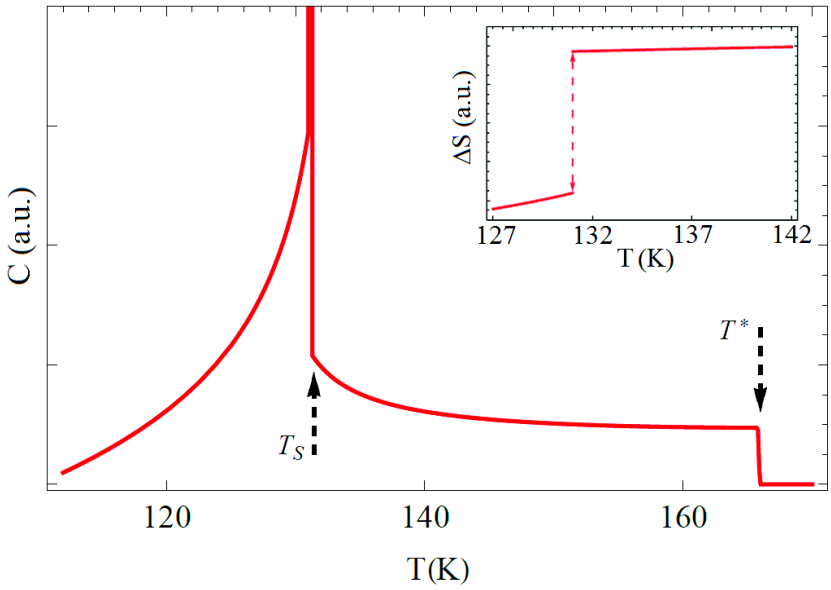

Fig 4.11 Temperature dependence of the specific heat of $BaFe_2As_2$ as derived from the GL model. Inset shows the calculated result of the temperature dependence of entropy near the AFM/structural transition.

As we can see, the theoretical curves of *S(T)* and *C(T)* reproduce the shape of the experimental curves quite well, with a similar sharp peak in the specific heat and a step in the entropy at T_s, though the experimental entropy curve is more smeared possibly due to fluctuations or

inhomogeneity in the sample. In addition, the theoretical specific heat curve also reveals a small step at the nematic transition (T^*). In order to evaluate the expected height of this step, we consider the ratio of the change in entropy at T_s, as given by $\Delta S = -\left(\partial F/\partial T\big|_{T_s^+} - \partial F/\partial T\big|_{T_s^-} \right)$, and the step in the specific heat at T^*, $\Delta C = -T\,\partial^2 F/\partial T^2\big|_{T^*}$. This ratio is independent of an over-all scale factor and is found from the GL model to be $\Delta S\,|_{T_s}/\Delta C\,|_{T^*} \approx 5$.

From Fig. 2 we obtain the change in entropy at the AFM/structural transition of ~0.5 J/mol K, yielding the expected height of the specific heat anomaly at T^* of ~ 0.1 J/mol K. Considering that the noise level at ~170 K (the expected T^* for $BaFe_2As_2$) is ~0.012 J/mol K, we should be able to distinguish such a feature, indicating that there are no 2nd order phase transition at T^* and that the transition into the C_2-phase occurs at T_S.

It is important to recognize that the phenomenological order parameter ψ contains, in principle, both spin-nematic and orbital components, which are linearly coupled by symmetry. The magnetic degrees of freedom (DOF) are taken into account in the free energy through the spin-nematic component of ψ. Thus in the case of an AFM order also developing at T_S, which apparently is true for $BaFe_2As_2$, the related change in entropy is automatically taken into account through the spin-nematic component of ψ. Moreover, any additional entropy change at T_S in the orbital DOF is taken into account through the orbital component of ψ. Thus, the free energy constructed above contains all the thermodynamic information about the system and the entropy step at *Ts* calculated in our model has taken into account all the related DOF.

Fig. 4.12 shows the magnetization of both as grown and annealed $BaFe_2As_2$ samples measured in an applied field of 1 T along the basal plane and along the c-axis, respectively. Note that for annealed $BaFe_2As_2$, a Curie-type paramagnetic background ($M_{Curie} = a + \frac{b}{T}$), possibly coming

from precipitates of Fe or Fe related compound introduced during annealing, was subtracted. Similar background subtraction was also done on the magnetization of as grown $BaFe_2As_2$, although the magnitude of the background is almost negligible.

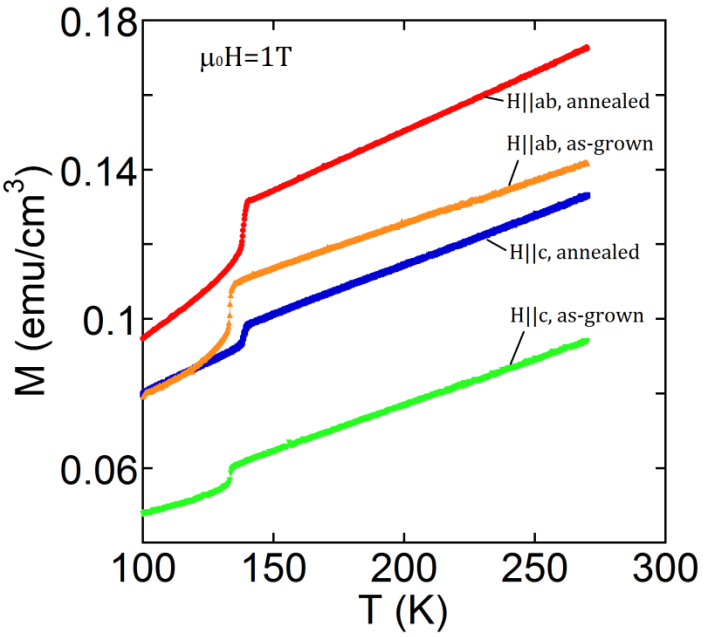

Fig 4.12 Temperature dependence of the magnetization of as grown and annealed $BaFe_2As_2$ in an applied field of 1T along the *ab* plane and *c*-axis.

High DC magnetic fields on the order of 10T [113] and pulsed fields of 27.5T [114] have been observed to partially detwin under-doped $Ba(Fe_{1-x}Co_x)_2As_2$ crystals. This field dependence of the structure may suppress the sharpness of the structural transition; however, in our case, a relatively small applied field of 1T would not cause any significant detwinning effects that could lead to transition broadening. In fact, we observe a sharp step-like feature in the magnetization for both applied field directions in as grown and annealed samples indicates the AFM/Structural transition. The transition temperatures are consistent with those obtained from the specific heat measurements. The value of the magnetization and the drop at T_N for $H \parallel ab$ are higher than that for $H \parallel c$ by a factor of ~2-3, consistent with the in-plane spin arrangements in the Fe-As planes

[17]. Above the magneto-structural transition the magnetization increases linearly with temperature [115], distinctly different from the temperature-independent Pauli paramagnetism of itinerant carriers as well as the 1/*T*-decrease in the Curie-Weiss law of independent local moments. Such linear temperature dependence has been reported previously for several iron-based superconductors, including $BaFe_2As_2$ [116], $CaFe_2As_2$ [117], $LaFeAsO_{1-x}F_x$ [118], $Ca(Fe_{1-x}Co_x)_2As_2$ [118] and $SrFe_2As_2$ [119], as well as high-T_c $La_{2-x}SrCuO_{4-y}$ [120]. It was suggested to be a consequence of strong AFM correlations [121, 122] persisting in the paramagnetic state or, alternatively, of flat electronic bands caused by the quasi 2D crystal structure [123].

Subtraction of the aforementioned linear $M(T)$ background from the raw data yields a detailed presentation of the magnetic transition shown in Fig 4.13. The transition is slightly sharper for the annealed compound. Specifically, the broadening right above the transition found in the as grown sample almost disappears after annealing. Such a sharp transition without any indication of precursors is quite unexpected if magnetic fluctuations play a key role in the magnetostructural transition. However, this seeming contradiction can be explained by the fact that uniform magnetization is mostly sensitive to fluctuations at $\boldsymbol{Q} = 0$ in the BZ, and is therefore, not a direct measurement of the fluctuations at the SDW ordering wave vectors ($\boldsymbol{Q} = (0, \pi)$ and $(\pi, 0)$). Recently, a scaling relation between the NMR spin lattice relaxation and the elastic shear modulus in $Ba(Fe_{1-x}Co_x)_2As_2$ was discovered [124], indicative of strong coupling between magnetic and structural fluctuations.

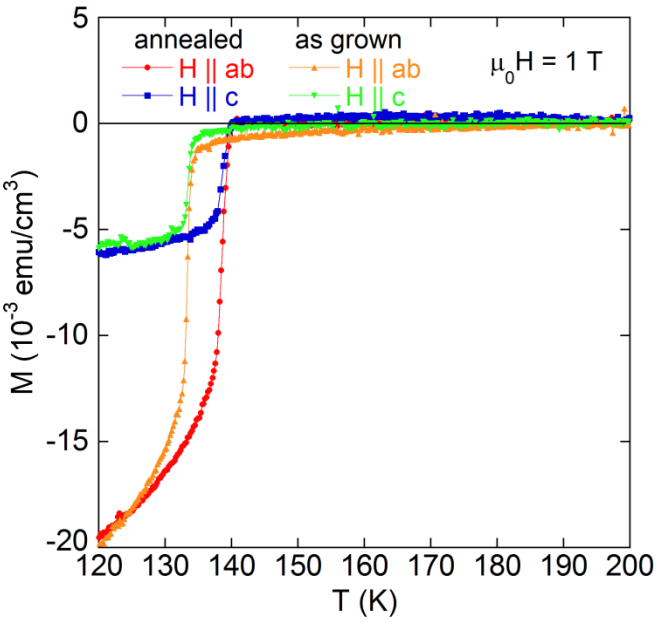

Fig 4.13 Temperature dependence of the magnetization of as grown and annealed $BaFe_2As_2$ after subtraction of the linear *M(T)* background in an applied field of 1T along the *ab* plane and *c*-axis.

4.3 Summary and discussion

In this chapter, I presented SQUID magnetometry and high resolution AC microcalorimetry measurements of single crystal $BaFe_2(As_{1-x}P_x)_2$ ($x = 0,\ 0.3$). This technique allows us to probe the thermodynamic phase diagram without the application of external potentially symmetry breaking fields such as strain or magnetic, nor does it exert uncontrolled residual strains for example due to thermal contraction. Results on both as grown and annealed $BaFe_2As_2$ reveal a sharp peak at the AFM/Structural transitions. A kink in the entropy of annealed $BaFe_2As_2$ gives evidence for splitting of the two transitions by approximately 0.5 K. Our measurements show no additional features in the specific heat of both $BaFe_2As_2$ and $BaFe_2(As_{0.7}P_{0.3})_2$ in the temperature regions of the purported "true" nematic phase transition reported in torque measurements [49], eventhough the Ginzburg-Landau model used to fit the magnetic torque data indicates that the expected thermal anomaly should be easily observable with our experimental resolution of 10^{-4}.

We thus conclude that the behavior previously reported [61] for $BaFe_2As_2$ at T^* does not represent a second order phase transition, and that the phase transition into the orthorhombic phase does occur at T_S.

Chapter 5

Emerging new phases in Fe-based superconductor and thermodynamics of High temperature superconductors

5.1 Study of the emergent C_4 SDW phase in $Ba_{1-x}Na_xFe_2As_2$

5.1.1 Introduction

Recently a wholly new magnetic phase with C_4-symmetry in the lattice was found to exist at the boundary between superconductivity and stripe mangetism in $Ba_{1-x}Na_xFe_2As_2$ by high resolution neutron diffraction experiments [58] (Fig 5.1). For several doping levels: x=0.24, 0.26, 0.27 and 0.28 in the coexistence regime of antiferromagnetism (or spin density wave (SDW)) and superconductivity, an emergent C_4 symmetric SDW phase was found above the superconducting transition (Fig 5.2). This discovery has important implications for the origin of magnetic and structural transitions in iron-based superconductors. The results agree with the prediction of the spin-nematic models [44] that a C_4 phase can become degenerate with the C_2 phase only at higher doping when hole and electron Fermi surfaces are not well nested, and that the stability of the C_4 phase would be limited to a very narrow region close to the suppression of anitiferromagnetism.

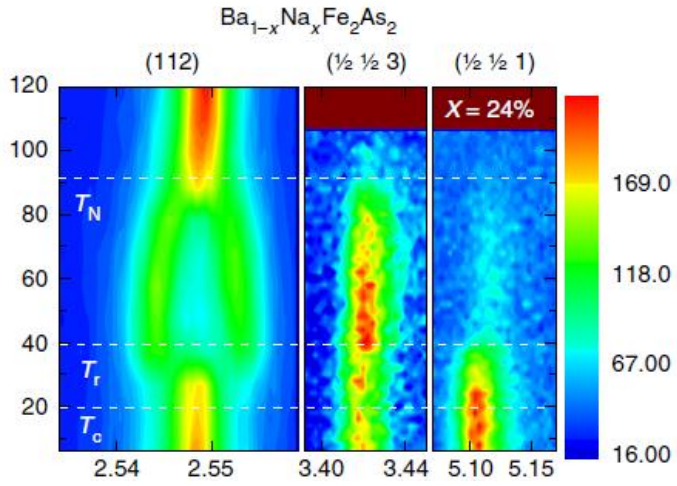

Fig 5.1 Temperature dependence of powder neutron diffraction from $Ba_{1-x}Na_xFe_2As_2$ (x=0.24). The first diffractogram shows data from the (112) Bragg peak (using tetragonal indices), which shows the orthorhombic transition at T_N and the re-entrant tetragonal transition at T_r. The other two diffractorgrams are from mangetic bragg peaks. The $(\frac{1}{2},\frac{1}{2},3)$ data shows the onset of stripe SDW order at T_N. The $(\frac{1}{2},\frac{1}{2},3)$ data show the onset of the C_4 SDW order at T_r [58].

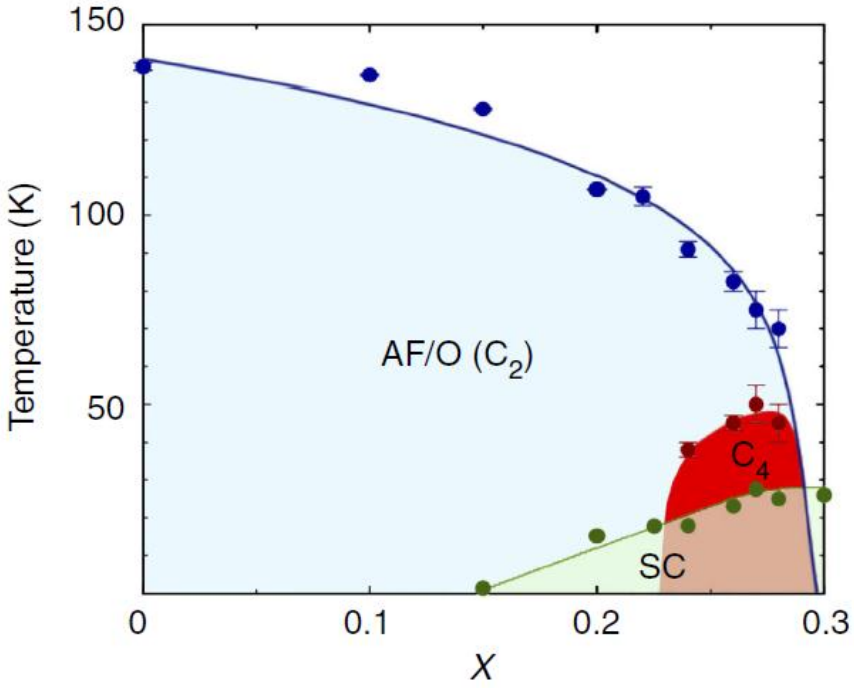

Fig 5.2 Phase diagram of $Ba_{1-x}Na_xFe_2As_2$. Blue points indicate coincident antiferromagnetic and Tetragonal to Orthorhombic structural transition temperatures,T_N. Red points indicate observed transition temperatures, T_r, into the C_4 phase, all measured by neutron diffraction. Green points indicate superconducting transition temperatures, T_c, determined from magnetization data [58].

In an attempt to map out with more precision the transition temperatures of this new emergent C_4 cymmetric magnetic phase, we performed heat capacity measurements of a series of samples of $Ba_{1-x}Na_xFe_2As_2$, at doping levels of x=0.22,0.26,0.27 and 0.28.

5.1.2 $Ba_{1-x}Na_xFe_2As_2$ (x=0.22)

The sample is of polycrystalline form and has dimensions of ~120μm x 90μm x 15μm. The specific heat of the sample was measured from 15K to 120K and a clear bump- shaped anomaly is found at around 100K (Fig 5.3 (left)), indicative of the AFM/SDW transition which was later confirmed by SQUID magnetization measurements. A better view of the details of this phase transition is made available by subtracting a smooth polynomial background from the raw data, as shown in Fig 5.3 (right). We use entropy conservation to extract the transition temperature as T_N=97.5K.

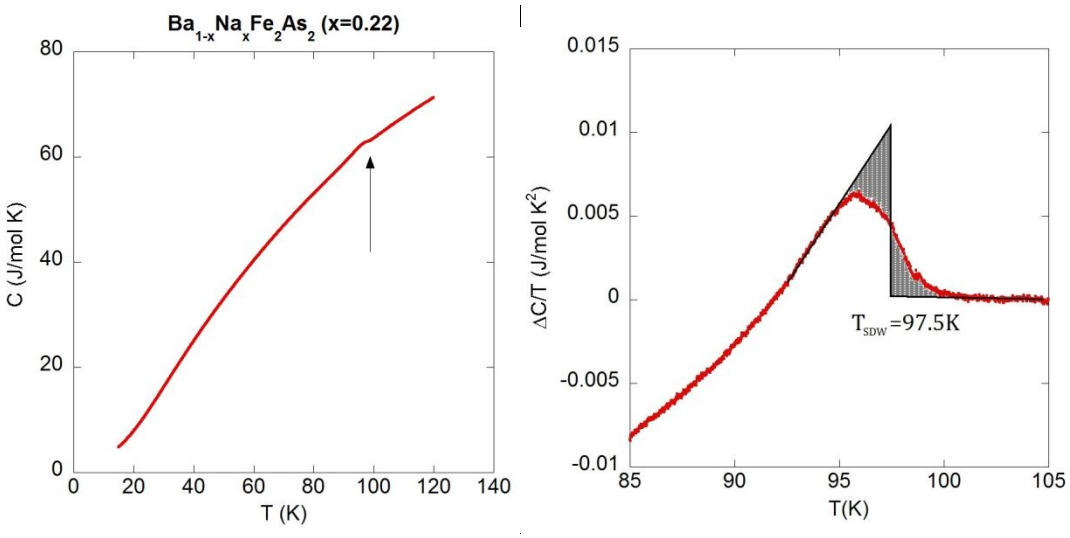

Fig 5.3 (left) Temperature dependence of the specific heat of $Ba_{1-x}Na_xFe_2As_2$ (x=0.22) from 15K to 120K, a bump-like feature at around 100K marks the AFM/structural transition. (right) C/T data of the same sample after subtraction of a smooth background. An illustration of the entropy conservation construction is shown in the figure as our way to determine the transition temperature precisely.

To look for the superconducting transition in $Ba_{1-x}Na_xFe_2As_2$ (x=0.22), we measured the specific heat from 10K to 30K with high precision. The data is shown in Fig 5.4 as a plot of C/T versus T. A broad hump in the specific heat roughly between 14K and 18K can be distinguished in the raw data (left figure in Fig 5.4). After a smooth polynomial (second order) background subtraction, the superconducting transition is seen as a broadened step with an onset Tc of ~18K and a width of ~2K. It is worth mentioning that the superconducting anomaly is extremely small, with a $\Delta C / T_c \approx 2.5\text{mJ/mol K}^2$, almost an order of magnitude smaller than $\Delta C / T_c = 20\ \text{mJ/mol K}^2$ for a $BaFe_2(As_{1-x}P_x)_2$ (x=0.5) single crystal sample which has a T_c of 18K [125]. This might be due to the poor quality of the polycrystalline sample that we used for our measurements which contains significant amount of non-superconducting materials, such as flux from material growth.

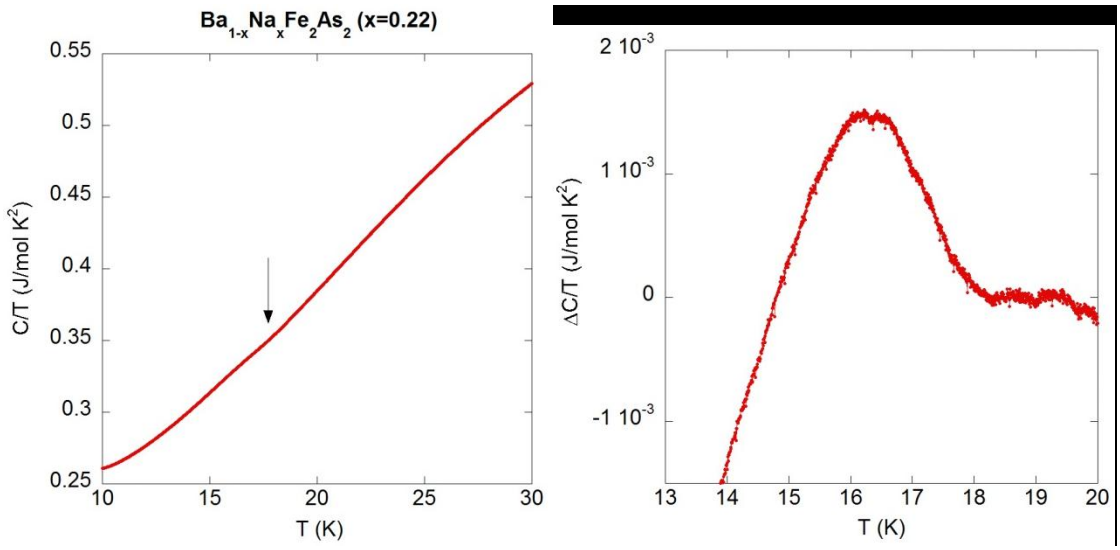

Fig 5.4 (Left) Temperature dependence of the specific heat (more precisely, C/T) of $Ba_{1-x}Na_xFe_2As_2$ (x=0.22) from 10K to 30K. A broad bump-like feature can be distinguished between 15K and 20K and is marked by the black arrow in the figure. (Right) the data after a smooth background subtraction showing the superconducting transition with more details.

The magnetization of $Ba_{1-x}Na_xFe_2As_2$ (x=0.22) has also been measured from 15K to 120K in an applied field of 2T after the sample was cooled in zero field (ZFC). The result is shown in Fig 5.5. A small step like feature is found at 98K which corresponds to the AFM (or SDW) transition, the results agrees with specific heat data quite well since the temperature in specific heat data needs to be corrected for an offset temperature with a value of ~0.6K due to the DC component of heating power. The drop in magnetization associated with the superconducting transition onsets at 18K which is also consistent with results from specific heat measurements.

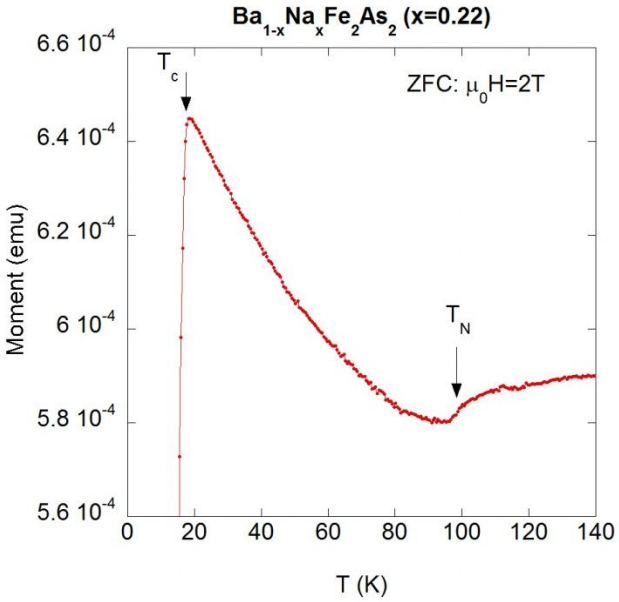

Fig 5.5 Temperature dependence of the magnetization of $Ba_{1-x}Na_xFe_2As_2$ (x=0.22) in an applied field of 2T, zero field cooled. The arrows mark the onset of the superconducting transition and the AFM transition respectively.

It is worth mentioning that this sample lies outside of the emergent C_4 phase in the phase diagram of $Ba_{1-x}Na_xFe_2As_2$ and we don't see any new phase transition in our data. However, our results confirm a T_c at 18K and a T_N at 98K, which agrees with results from neutron diffraction measurements and provides more accurate transition temperatures. It also gives us a general idea of the quality of the sample and how the AFM transition looks like in specific heat.

5.1.3 $Ba_{1-x}Na_xFe_2As_2$ (x=0.26)

For this doping level, neutron diffraction results tell us that there would be 3 phase transitions: one AFM/SDW transition at ~80K, one re-entrant C_2 to C_4 symmetry structural transition at ~ 45K and one superconducting transition at ~25K [58]. We performed specific heat measurement of this sample at a frequency of 34Hz (determined by a frequency scan at 40K) with a heating current of 120 μA from 20K to 105K. The result is shown below in Fig 5.6:

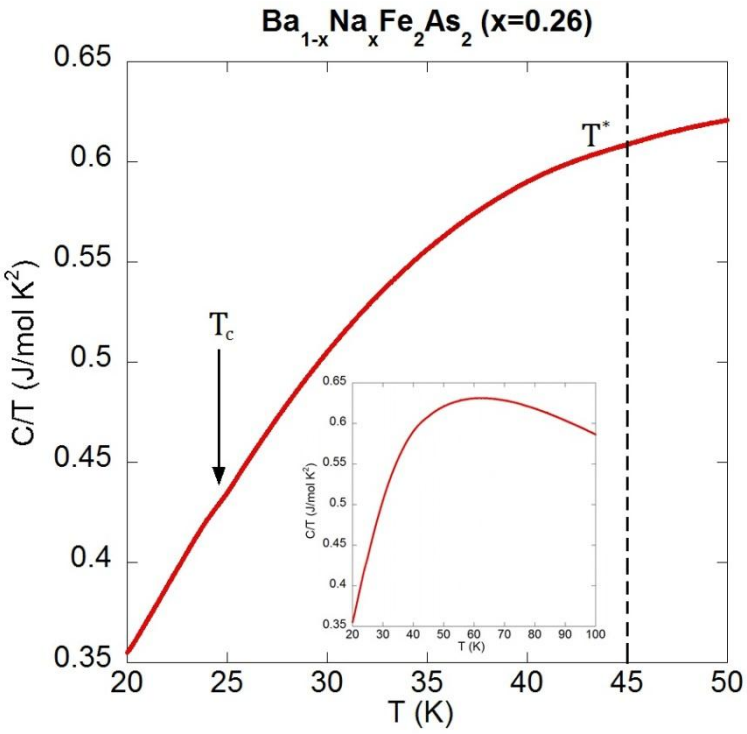

Fig 5.6 (main panel) Temperature dependence of the specific heat of $Ba_{1-x}Na_xFe_2As_2$ (x=0.26) from 20 to 50K with the arrow marking the superconducting transition at around 25K and the dashed line marking another weak anomaly at $T^* = 45K$. (Inset) Specific heat data for the sample sample up to 100K.

A weak anomaly can be seen at around 25K in the specific heat data which marks the superconducting transition at this doping level in the sample. In addition to this feature, another weak feature can be seen in specific heat at around $T^* = 45K$ and is marked by the dashed line which possibly signifies the reentrant C_2 to C_4 transition in the sample. A better look at the details of the superconducting transition is made possible by subtracting a smooth polynomial background from the raw data near the superconducting feature. The results is shown in Fig 5.7. Using entropy conservation construction, the height of the superconducting anomaly can be

determined as $\Delta C / T_c \approx 3.6 \text{mJ/mol K}^2$. This value is slightly higher than that of $Ba_{1-x}Na_xFe_2As_2$ (x=0.22). Considering that the T_c for x=0.26 sample is also higher (25K comparing to 18K onset), the results are consistent. However, we have to emphasize again that the value is considerably smaller (~ a factor of 10) than that from measurements of a similar single crystal sample $Ba_{0.77}K_{0.23}Fe_2As_2$ with about the same T_c [126], which can be attributed to the poor quality of the polycrystalline sample we have used. From the comparison of the results, we estimate that only ~10% of the sample is actually superconducting.

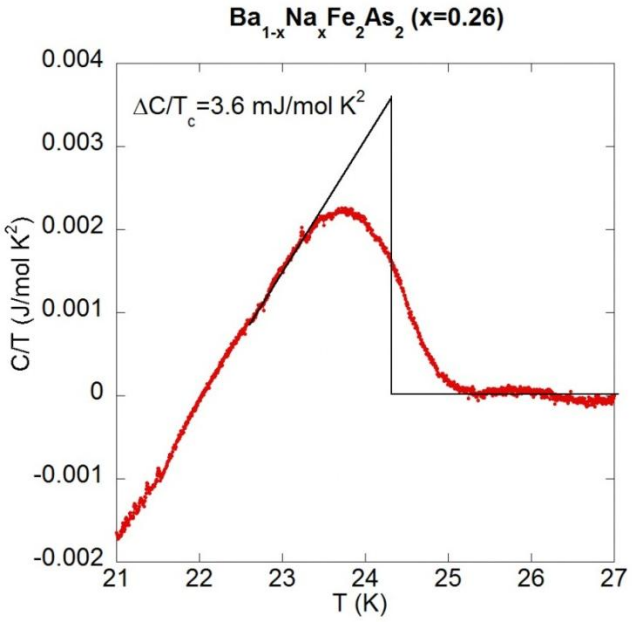

Fig 5.7 Specific heat of $Ba_{1-x}Na_xFe_2As_2$ (x=0.26) after subtraction of a normal state background showing the superconducting transition in details. The step in the specific heat is determined by entropy conservation.

A better look at the specific heat anomaly at T* is made available by taking the first derivative of the heat capacity data and the results is shown in Fig 5.8.

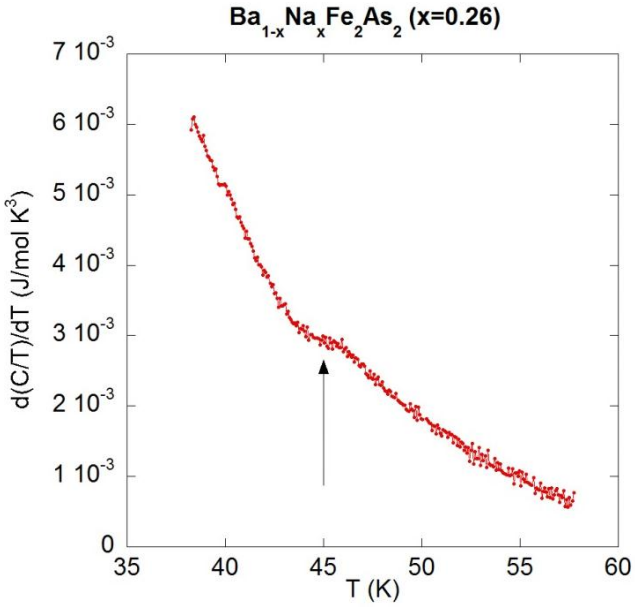

Fig 5.8 The first derivative of the specific heat of $Ba_{1-x}Na_xFe_2As_2$ (x=0.26) from 35 to 60K. The anomaly at T^*=45K is clearly shown.

Unfortunately, we are not able to distinguish another feature in the temperature region above T^* that could possibly mark the AFM transition in the sample, which brings doubt to the nature of the feature at T^*. There are be two possiblities: 1) T^* marks the regular AFM(SDW) transition and there is not a reentrant C_4 symmetric SDW phase transition at this doping level; 2) T^* indeed marks the new phase transition. However, due to certain reasons (e.g. sample quality), we cannot locate the regular AFM(SDW) transition.

To further investigate and verify the phase transitions we found in specific heat, we also performed SQUID magnetization measurments on powder samples of $Ba_{0.74}Na_{0.26}Fe_2As_2$ from the same batch (Fig 5.9). In addition to the superconducting transition, which is manifested as a drop in the magnetization with a onset of 25K (Fig 5.10), we found that there is a kink in the M/T vs T curve at 45K for all three different applied magnetic fields (H=2kG, 1T and 2T) with either ZFC (Zero-field cooled) or FC (Field cooled) conditions. The transition temperatures agree with that from specific heat measurements. No evidence for another phase transition above 45K can be

found, which also agrees with the specific heat measurement results. Thus the existence of the re-entrant C_4 AFM(SDW) transition is not clear based on our experimental data.

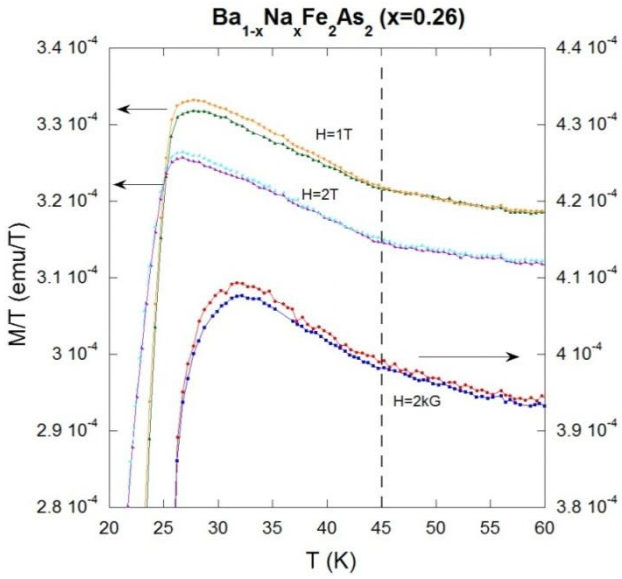

Fig 5.9 Magnetization (actually magnetic moment) versus temperature for $Ba_{1-x}Na_xFe_2As_2$ (x=0.26) from 20 to 60K. The kink-like anomalies are marked by the dashed line at 45K. Different colored curves for the same applied field are results from ZFC and FC measurement conditions respectively.

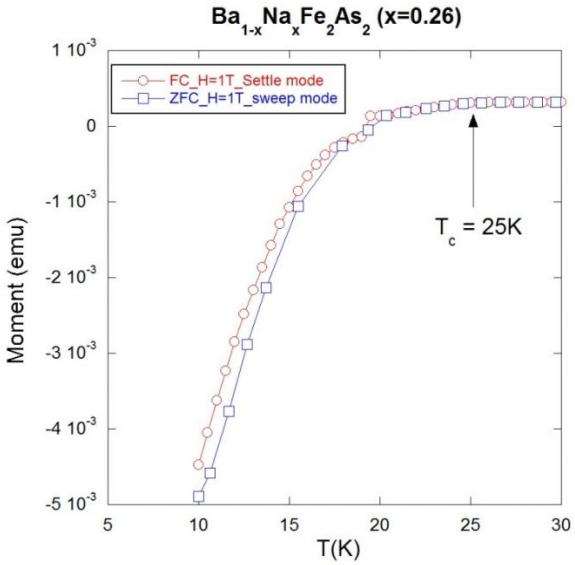

Fig 5.10 Magnetic moment versus temperature for $Ba_{1-x}Na_xFe_2As_2$ (x=0.26) from 10 to 30K in an applied field of 1T under ZFC (blue) and FC (red) conditions. The black arrow marks the T_c at 25K.

5.1.4 $Ba_{1-x}Na_xFe_2As_2$ (x=0.28)

Two samples, sample 1 and sample 2, of $Ba_{1-x}Na_xFe_2As_2$ at doping level of x=0.28 have also been measured. According to neutron diffraction data [58], this sample should have T_c in the range of 25 to 30K, T_r (reentrant C_4 symmetry SDW transition) in the range of 40 to 50K and T_N in the range of 65 to 75K. Our specific heat results show that the samples are actually multi-phased and the doping level has variations from sample to sample, which again brought doubt to the interpretation of data from neutron diffraction measurements.

The specific heat of sample 1 (size: 88μm x 78μm x 15μm) is measured from 20K to 80K and the result is shown below in Fig 5.11. A step like anomaly is found strangely at around 34K. By subtracting a normal state background, we look at the step in specific heat in more details in the inset of Fig 5.11. The behaviors of this anomaly in applied magnetic fields give evidence for the nature of the anomaly as a superconducting transition (Fig 5.12). This contradicts the T_c value of ~26K as given in Ref [58] for x=0.28 doping level and in fact agrees more with the literature T_c value for a $Ba_{1-x}Na_xFe_2As_2$ (x=0.4) single crystal sample [127]. The height of the step at T_c from our data is found to be $\Delta C / T_c = 58$ mJ/mol K^2, about 40% lower than the value of $\Delta C / T_c = 102$ mJ/mol K^2 for the $Ba_{1-x}Na_xFe_2As_2$ (x=0.4) single crystal sample from Ref [127].

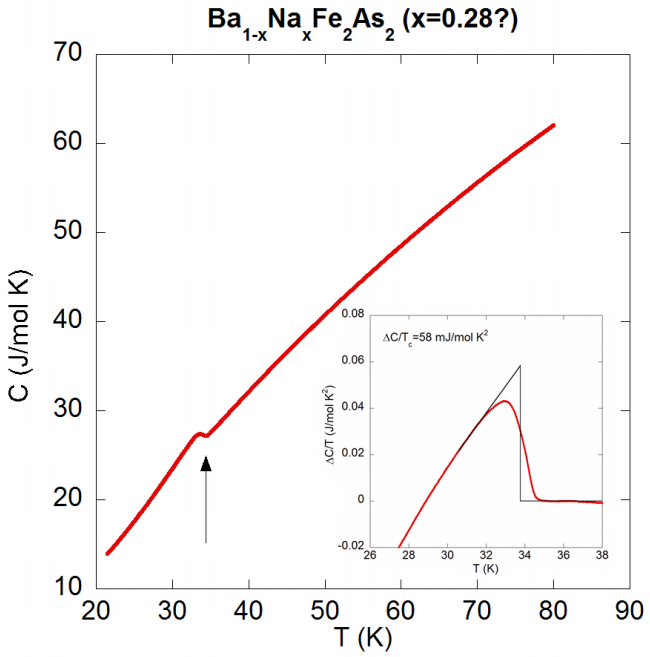

Fig 5.11 (Main panel) Temperature dependence of the specific heat for sample 1 of $Ba_{1-x}Na_xFe_2As_2$ (x=0.28). The black arrow marks the step-like feature at the superconducting transition. (Inset) Detailed view of the superconducting transition after subtraction of a normal state background.

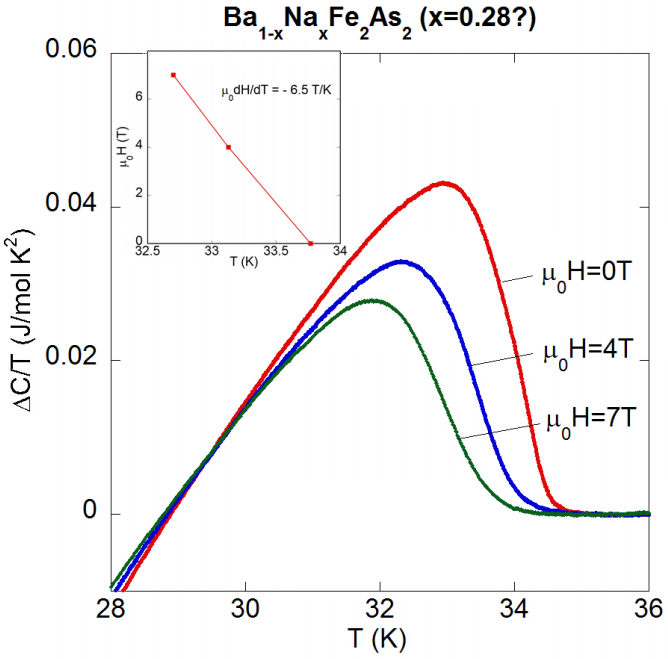

Fig 5.12 (Main panel) temperature dependence of the specific heat for three different applied field after substraction of a normal state background. (Inset) Magnetic phase diagram extracted from the data, a linear upper critical field slope of $\mu_0 dH_{c2} / dT = -6.5$ T/K is found.

From the field dependence of the specific heat data, we extract the upper critical field slope near T_c as $\mu_0 dH_{c2} / dT = -6.5$ T/K . This value is slightly larger than the value of $\mu_0 dH_{c2}{}^{c} / dT = -5.25$ T/K from [127] for applied field along the crystalline c-axis. Considering that the sample we meaured is polycrystalline and the alignment of the field could be off from c-axis by quite a bit. The slightly higher value we got for the upper critical field slope is quite reasonable. Because of the good agreement of our data with the literature data for $Ba_{0.6}Na_{0.4}Fe_2As_2$, we conclude that sample 1 actully has a doping level of 0.4, rather than 0.28. What this indicates is that the powdered $Ba_{1-x}Na_xFe_2As_2$ sample (x=0.28) we used in our measurements is not homogenous and some of them is actually optimum doped (x=0.4).

In an attempt to verify our conclusion, we measured the heat capacity of another sample (sample 2) from the same batch of powered polycrystals. The result is shown in figure 5.13.

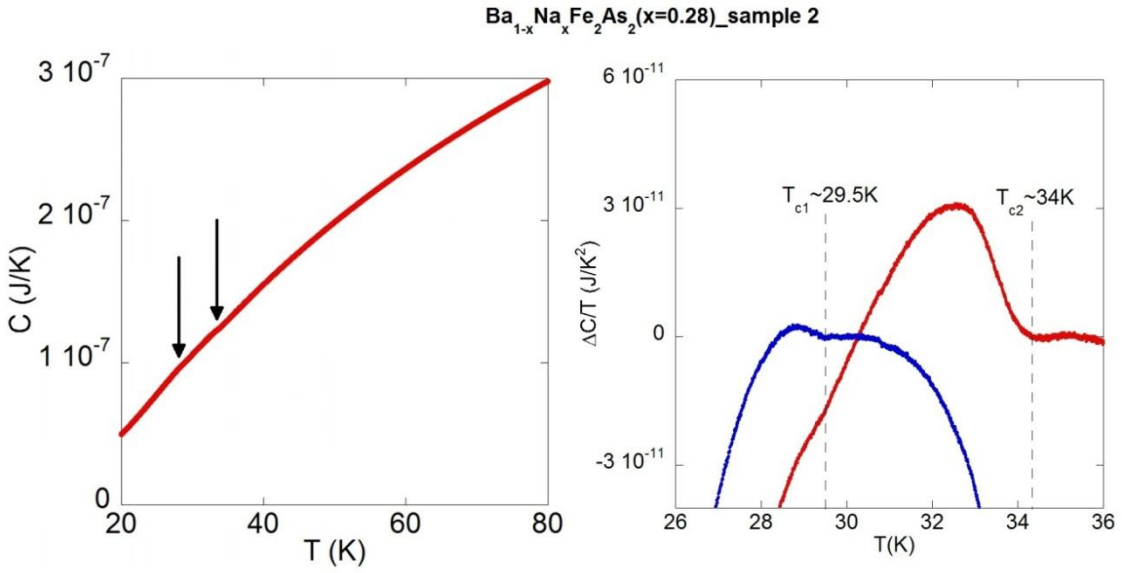

Fig 5.13 (Left) temperature dependence of the heat capacity of sample 2 of $Ba_{1-x}Na_xFe_2As_2$ (x=0.28). Two small anomalies marked by black arrows can be seen in the raw data. (Right) heat capacity data after two different smooth background subtractions to give a better look at the two transitions at 34K (red) and 29.5K (blue) respectively.

The data shows two anomalies at 34K and 29.5K. The feature at 34K, as we have seen in sample 1, is the superconducting transition temperature for $Ba_{0.6}Na_{0.4}Fe_2As_2$, i.e., x=0.4. The nature of the 29K feature was confirmed as another superconducting transition by the observation of a shift in the position of the feature in an applied magnetic field of 4T (Fig 5.14). This results, combined with the results from sample 1, confirmed that the sample we obtained were not homogeneous and thus not useful for identifying the reentrant C_4 symmetric SDW transition claimed by neutron diffraction measurements.

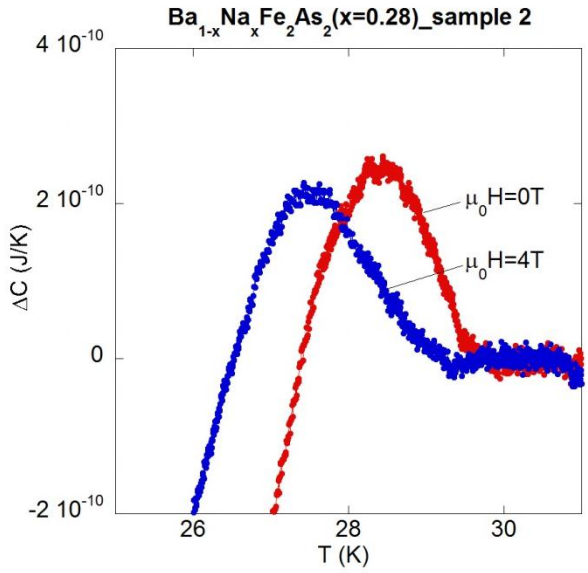

Fig 5.14 Temperature dependence of the heat capacity of sample 2 of $Ba_{1-x}Na_xFe_2As_2$ (x=0.28) near 29K for applied fields of 0T (red) and 4T (blue) respectively.

5.1.5 Discussion

In conclusion, we studied the specific heat of $Ba_{1-x}Na_xFe_2As_2$ at several different doping levels, i.e. x=0.22, 0.26 and 0.28. For the x=0.22 sample, a peak in the specific heat and a step in the magnetization at 98K marks the AFM/structural transition. Another tiny step in specific heat and a drop in the magnetization at 18K mark the superconducting (SC) transition. The SC anomaly height found from our data is almost a factor of 10 smaller than that of a similar sample in the "122" family with about the same T_c [126], which can be attributed to the poor quality of the polycrystalline sample that we have used for our measurements. For the x=0.26 sample, we were about to find a phase transition at $T^* = 45K$ which is exactly the transition temperature for the reentrant C_4 phase transition. However, the lack of signs for another transition at around 80K leaves doubt about the nature of the transition at 45K. It is equally possible that the transition at 45K marks the SDW transition and there isn't a reentrant SDW transition into C_4 symmetry. For the x=0.28 samples, we found that they are not homogeneous and many has a SC transition at 34K, which in fact corresponds to x=0.4 optimum doped samples. As a result, we cannot draw any additional conclusion about the reentrant C_4 SDW phase transition from the data measured on samples at this doping level.

It is worth mentioning that recently a group of scientists at KIT indeed found through thermal expansion and heat capacity measurements the existence of a C_4 SDW phase in underdoped $Ba_{1-x}K_xFe_2As_2$ [126]. The high quality single crystals used in their experiments certainly helped to confirm the existence of this new phase. However, for the $Ba_{1-x}Na_xFe_2As_2$, further investigations with high quality samples are definitely needed to verify the existence and determine the phase boundaries of this emergent new phase.

5.2 Heavy ion irradiation effects on the thermodynamic anisotropy of $YBa_2Cu_3O_{7-\delta}$ single crystals

5.2.1 Introduction

The vortex dynamics of high temperature superconductors (HTSC) is quite different from that of traditional superconductors. Among the non-conventional characteristics that were early identified are: 1) Large drop of the critical current density J_c with temperature; 2) existence of an "irreversibility line" in the H-T phase diagram above which $J_c = 0$ and the magnetic response is reversible; 3) very fast time relaxation of the persistent currents in the irreversible regime, orders of magnitude faster than in low temperature superconductors [128].

Aligned columnar defects produced by heavy-ion irradiation in HTSC are amorphous tracks whose diameters are a few times the coherence length of these materials (Fig 5.15(Left)). When the magnetic field is applied parallel to the tracks, each defect can confine the whole length of a vortex core without any increase of the elastic energy of vortex, at least at low fields where vortex interactions are weak. These columnar shaped defects are the most effective pinning centers for flux lines in HTSCs [128]. They are found to generate large increases in the critical current densities (Fig 5.15(right)) and expand the irreversible regimes (Fig 5.16) in $YBa_2Cu_3O_{7-\delta}$ and the various Bi- and Tl-based compounds. In $YBa_2Cu_3O_{7-\delta}$ single crystals and thin films, the pinning enhancement is strongly angular-dependent, and maximizes when the applied magnetic field is parallel to the amorphous latent tracks (Fig 5.17) [128].

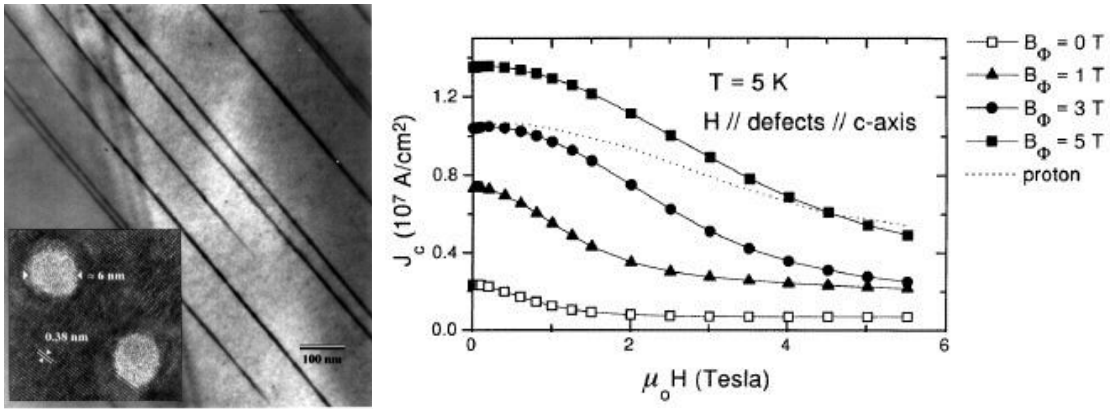

Fig 5.15 (Left) columnar shaped defects induced by heavy ion irradiation. The inset shows the cross section for two defects, the diameter of the amorphous region is around 6 nm. (Right) J_c *vs* H for $YBa_2Cu_3O_{7-\delta}$ single crystals irradiated with 580MeV Sn ions to different doses. For reference, the largest *Jc* obtained for a proton irradiated crystal is shown [129]. Note that doses are expressed as dose matching fields: $B_\Phi = n \cdot \Phi_0$, where n is the number of defects per unit area.

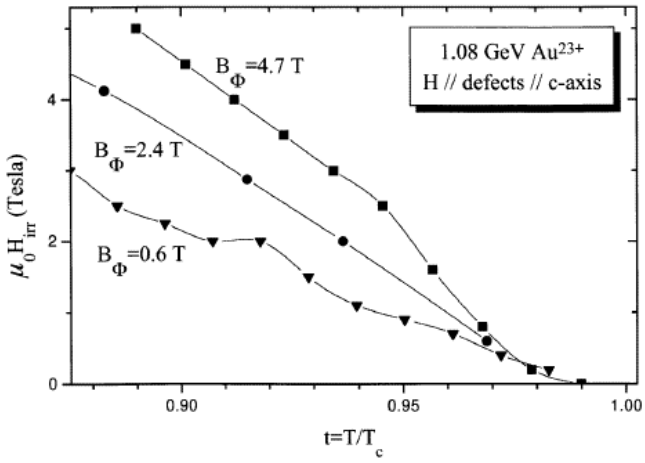

Fig 5.16 The irreversibility lines for three different Au heavy ion irradiation doses on $YBa_2Cu_3O_{7-\delta}$ single crystals [130].

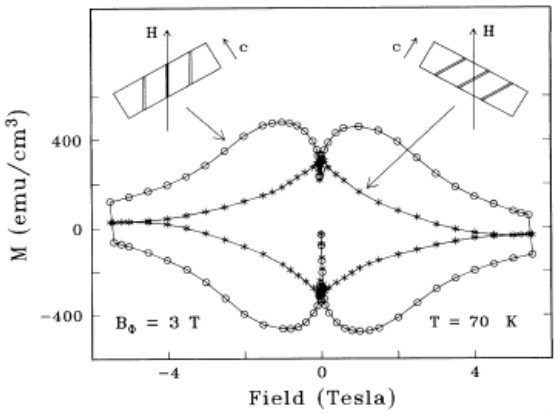

Fig 5.17 Hysteresis loops taken at 30K for an $YBa_2Cu_3O_{7-\delta}$ crystal irradiated at 30^o off the c-axis. The hysteresis loops for applied field aligned +/- 30^o with respect to the c-axis are shown [129].

Recently there have been experimental studies on the effects of heavy ion irradiation on the thermodynamic properties of a few iron-based superconductors. More specifically, it was found that heavy-ion irradiation can reduce the thermodynamic anisotropy of $SmFeAsO_{1-x}F_x$ [68], $SrFe_2(As_{1-x}P_x)_2$ [69] and $Ba_{1-x}K_xFe_2As_2$ [70]. In the case of $SmFeAsO_{1-x}F_x$, an irradiation dose of 4T and 9.5T was found to reduce the anisotropy by a factor of 2, from 8 to 4 (Fig 5.18).

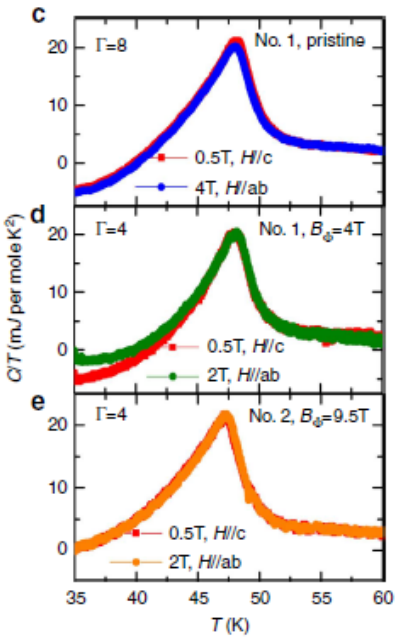

Fig 5.18 Measurements of the thermodynamic anisotropy of pristine and irradiated (B_Φ=4T, 9.5T) $SmFeAsO_{1-x}F_x$ through specific heat measurements [68].

However, the effects of heavy ion irradiation on the thermodynamic anisotropy of HTSC has not been thoroughly studied. Here we use high resolution angular dependent specific heat to study the effects of heavy ion irradiation on the thermodynamic properties of one of the most studied HTSC, $YBa_2Cu_3O_{7-\delta}$.

5.2.2 Experimental results

We irradiated two single crystal $YBa_2Cu_3O_{7-\delta}$ with 1.4GeV Au heavy ion to dose matching fields of B_Φ = 1T and 6T. Then specific heat of the pristine, 1T irradiated and 6T irradiated samples are measured with various magnetic fields applied along the ab plane and c-axis to determine the H-T phase diagram and the uppercritical field (H_{c2}) lines. Fixed field varing angle measurements were also carried out for the pristine and 6T irradiated sample to obtain the field angle dependence of the upper critical temperature (T_{c2}), which then is fitted by a GL model to extract the thermodynamic anisotropy with precision. Alignment of the sample with the applied fields was made with a hall sensor mounted on the bottom of the probe which approximately aligns with the calorimeter (+/- 2^o).

For the pristine sample, the specific heat versus temperature curves after subtraction of a normal state background from 83 to 99K for applied fields along the ab plane and c-axis have been plotted in Fig 5.19. The T_c for this pristine sample is 92.4K (taking the inflection point as criterion) and the width of the superconducting transition is only 0.6K. The appearance of a small peak below the main superconducting transition indicates the first order vortex melting transition and gives further evidence for the purity of the sample.

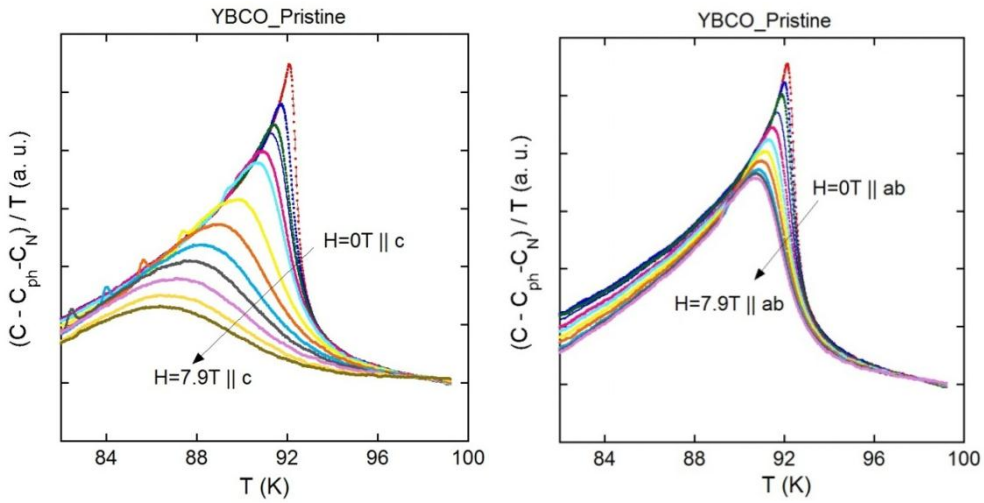

Fig 5.19 Temperature dependence of the specific heat for the pristine $YBa_2Cu_3O_{7-\delta}$ for applied fields from 0T to 7.9T along the crystalline c-axis (left) and ab-plane (right).

Taking the inflection point as the criterion for the critical temperature (T_c), we extract the H-T phase diagram for the pristine sample as shown in Fig 5.20. Using a linear weighted least square fit to the temperature dependence of the upper critical fields, we extract the upper critical field slopes as: $\mu_0 \frac{dH_{c2}^{c}}{dT} = -2.0 \pm 0.2$ T/K and $\mu_0 \frac{dH_{c2}^{ab}}{dT} = -12.5 \pm 0.8$ T/K. From the ratio of these two slopes we can extract the thermodynamic anisotropy for the pristine sample as:

$$\gamma_{pris} = \frac{dH_{c2}^{ab} / dT}{dH_{c2}^{c} / dT} = 6.3 \pm 0.7 \qquad (5.1)$$

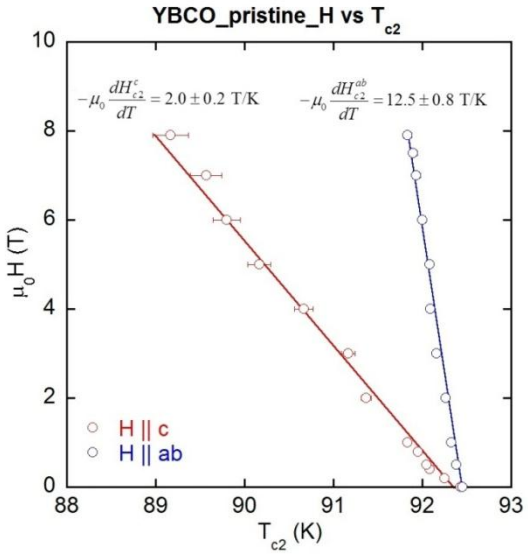

Fig 5.20 The H-T phase diagram for the pristine $YBa_2Cu_3O_{7-\delta}$ sample for applied field along the ab plane and c-axis.

Another way to determine the thermodynamic anisotropy using specific heat is to fit a Ginzburg-Landau (GL) model to the angular dependence of the upper critical field. However, this measurement requires scanning of the applied magnetic field which is not very well controlled in our experimental setup. Instead, as an alternative, we applied a fixed field to the sample and measure the temperature dependence of the specific heat for different applied field angles. The resulting upper critical temperature versus field angle can be fitted with the following GL model [131]:

$$T_{c2}(\theta) = T_{c0} + H\sqrt{\cos^2\theta + \gamma^2 \sin^2\theta} \,/\, (\partial \mathrm{H}_{c2}^{ab} / \partial \mathrm{T}) \tag{5.2}$$

Where H is the strength of the fixed applied field, T_{c0} is the Tc at zero applied field. θ is the field angle relative to the ab-plane.

For the pristine $YBa_2Cu_3O_{7-\delta}$ sample, we applied a magnetic field of 1T and measured C(T) for field angles of -9 degrees to 189 degrees, which consists of 36 groups of data. The upper critical

temperature (T_{c2}) for each C(T) is extracted by taking the inflection point as the criterion and the resulting $T_{c2}(\theta)$ plot is shown in Fig 5.21.

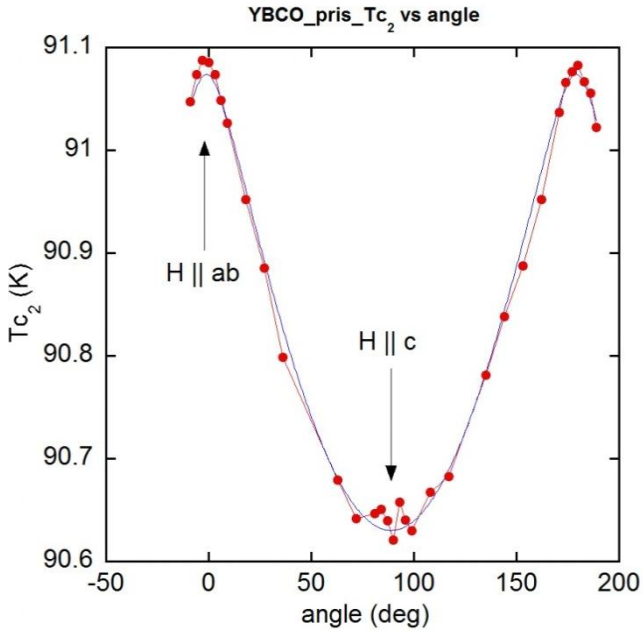

Fig 5.21 Angular dependence of the upper critical temperature of the pristine $YBa_2Cu_3O_{7-\delta}$ sample in an applied field of 1T. The blue curve is the GL model fit to the data.

Fitting the GL model in equation (5.2) to raw data gives us the anisotropy as a fitting parameter and its value determined from the fit is:

$$\gamma_{pris} = 7.8 \pm 2.0 \tag{5.3}$$

The slightly discrepancy between the anisotropy obtained from the GL model fit to $T_{c2}(\theta)$ data and that obtained from the ratio of upper critical field slopes probably comes from the slight misalignment between the magnetic field and the crystal orientations (~ 2 degrees). In this scenario, the anisotropy obtained from the upper critical field slopes would be slightly smaller.

We performed the same kind of specific heat measurements for the YBCO_Au6T sample (short name for the $B_\Phi = 6$ T Au heavy ion irradiated $YBa_2Cu_3O_{7-\delta}$ sample). The specific heat data for applied fields up to 4T along the c-axis and 7.9T along the ab-plane is shown in Fig 5.22 after a normal background subtraction. For this irradiated sample, we can see that T_c has been suppressed by 1.7K to 90.7K and the superconducting transition has also broadened, with a width of about 2.6K. The broadening of the transition brings more error to our determination of T_c , which is manifested by the large error bars in the H-T phase diagram (Fig 5.23) extracted from the specific heat data.

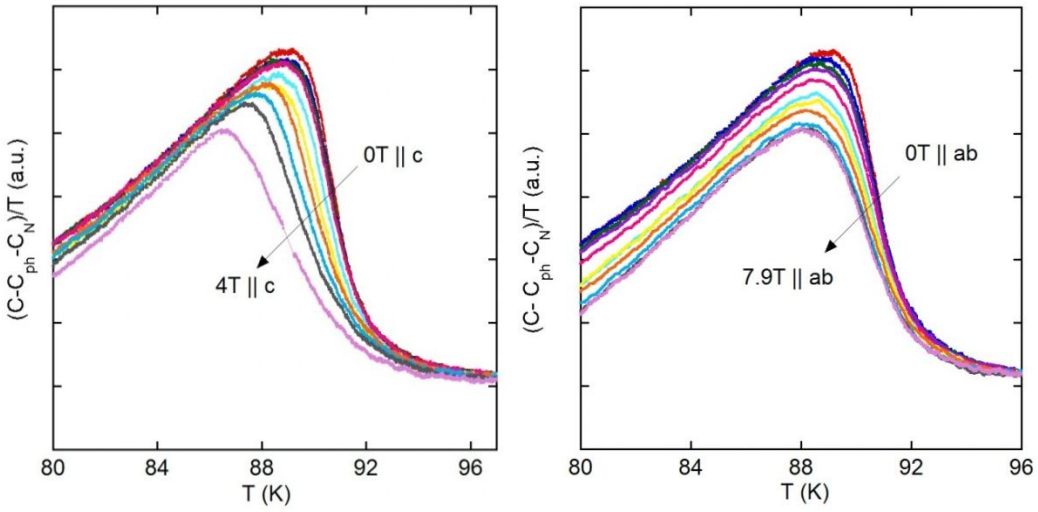

Fig 5.22 Temperature dependence of the specific heat of the Au heavy ion irradiated $YBa_2Cu_3O_{7-\delta}$ ($B_\Phi = 6$ T) for applied fields from 0 T to 7.9 T along the crystalline c-axis (left) and from 0 T to 4 T along the ab-plane (right).

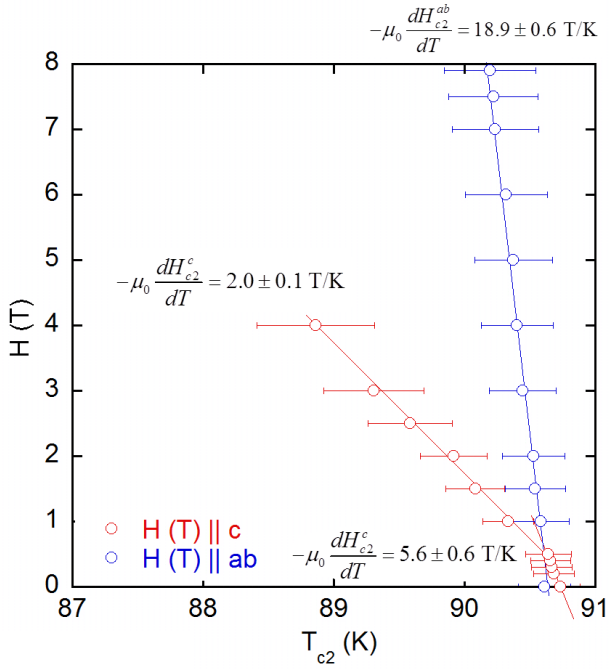

Fig 5.23 The H-T phase diagram for the irradiated $YBa_2Cu_3O_{7-\delta}$ sample ($B_\Phi = 6$ T) for applied fields along the ab plane and c-axis.

For magnetic fields applied along the c-axis, we can see that there is a variation in the slope of the upper critical field. Comparing to the pristine sample, the upper critical field slope along c-axis is enhanced in YBCO_Au6T by approximately a factor of 2.8 in the low field regime to $\mu_0 \frac{dH_{c2}^{c}}{dT} = -5.6 \pm 0.6$ T/K . It relaxes back to the value of the pristine sample at $\mu_0 \frac{dH_{c2}^{c}}{dT} = -2.0 \pm 0.1$ T/K in the high field regime. There is also an enhancement in the upper critical field slope along the ab-plane by a factor of ~1.5 to $\mu_0 \frac{dH_{c2}^{ab}}{dT} = -18.9 \pm 0.6$ T/K . In this case we can see that there is clearly an indication for reduction in the anisotropy after the Au heavy ion irradiation at $B_\Phi = 6$ T .

Angular dependent specific heat measurements at an applied field of 1T were also carried out for this irradiated sample and the resulting angular dependence of the upper critical temperature at H = 1T is presented in Fig 5.24.

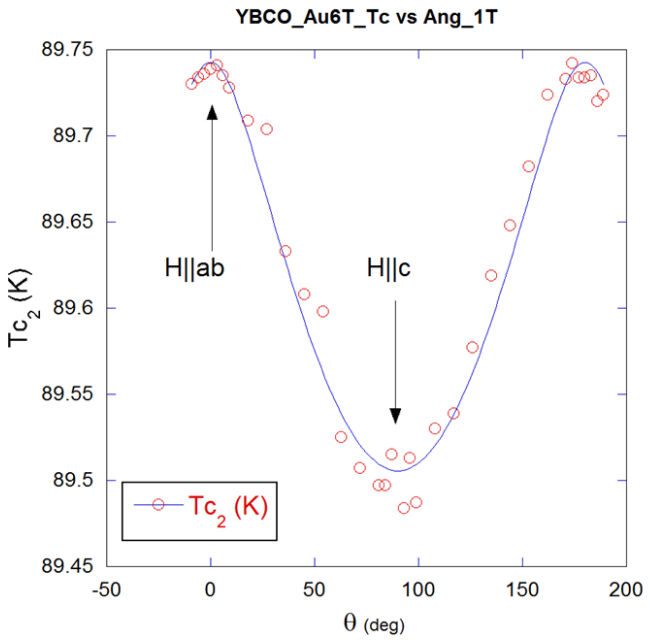

Fig 5.24 Angular dependence of the upper critical temperature of YBCO_Au6T sample in an applied field of 1T. The blue curve is the GL model fit to the data.

Fitting equation (5.2) to the data above gives us the value of the thermodynamic anisotropy of YBCO_Au6T as a fitting parameter:

$$\gamma_{B_\Phi=6T} = 3.7 \pm 1.5 \tag{5.4}$$

Comparing to the anisotropy of the pristine sample, we have:

$$\frac{\gamma_{B_\Phi=6T}}{\gamma_{pris}} = 0.5 \ \pm \ 0.3 \tag{5.5}$$

Thus we can see after Au heavy ion irradiation at a dose matching field of 6T, the anisotropy of $YBa_2Cu_3O_{7-\delta}$ has been reduced by one half. Similar reduction in the anisotropy of another $YBa_2Cu_3O_{7-\delta}$ sample irradiated at $B_\Phi = 1\ \mathrm{T}$ has also been measured in a similar manner as for the $B_\Phi = 6\ \mathrm{T}$ irradiated sample. The anisotropy for YBCO_Au1T was found to be $\gamma_{B_\Phi=1T} = 4.3 \pm 1.4$. Fig 5.25 plots T_c and anisotropy as a function of irradiation dose below:

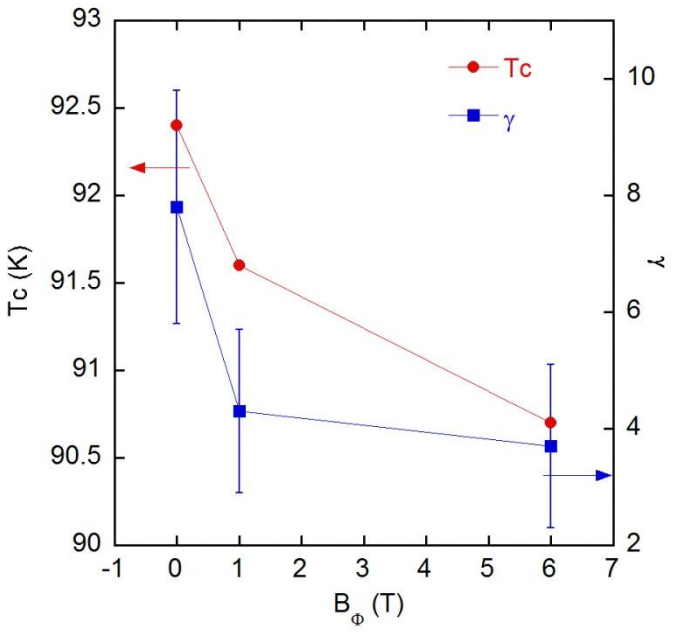

Fig 5.25 The critical temperature and thermodynamic anisotropy of $YBa_2Cu_3O_{7-\delta}$ plotted against 1.4GeV Au heavy ion irradiation dose, expressed in terms of dose matching field.

5.2.3 Comparison to theory and discussion

We can see that the anisotropy is suppressed quickly with irradiation and saturates at high irradiation doses. Similar trends can also be seen in the critical temperatures. A simple model that takes the anisotropic scattering caused by columnar defects into account from Ref [68] can qualitatively explain the reduction in anisotropy as seen in our measurements. Since the upper critical field near T_c in an anisotropic superconductor is given by (in the GL limit):

$$H_{c2}^{c} = \frac{\Phi_0}{2\pi\xi_{ab}^2(T)} = \frac{\Phi_0}{2\pi\xi_{ab}^2(0)}(1-\frac{T}{T_c}) \tag{5.6}$$

$$H_{c2}^{ab} = \frac{\Phi_0}{2\pi\xi_{ab}(T)\xi_c(T)} = \frac{\Phi_0}{2\pi\xi_{ab}(0)\xi_c(0)}(1-\frac{T}{T_c}) \tag{5.7}$$

The superconducting anisotropy is given by:

$$\gamma = \frac{H_{c2}^{ab}}{H_{c2}^{c}} = \frac{dH_{c2}^{ab}/dT}{dH_{c2}^{c}/dT} = \frac{\xi_{ab}}{\xi_c} \tag{5.8}$$

The effect of scattering on the coherent length is that the coherent length needs to be corrected for the mean free path:

$$\frac{1}{\xi^p} = \frac{1}{\xi_0} + \frac{1}{l} \tag{5.9}$$

Heavy ion irradiation leads to additional electron scattering, especially in plane:

$$\frac{1}{l_{ab}} = \frac{1}{l_{ab}^0} + \frac{1}{l_{irr}} \tag{5.10}$$

Assuming the additional scattering along c-axis is negligible, then:

$$\frac{1}{\xi_{ab}} = \frac{1}{\xi_{ab}^p} + \frac{1}{l_{irr}} \;\; ; \;\; \frac{1}{\xi_c} = \frac{1}{\xi_c^p} \tag{5.11}$$

Thus in the clean limit, the ratio of the anisotropy after heavy ion irradiation is given by:

$$\gamma = \frac{\xi_{ab}}{\xi_c} = \frac{\frac{1}{\xi_c^p}}{\frac{1}{\xi_{ab}^p} + \frac{1}{l_{irr}}} = \frac{\xi_{ab}^p}{\xi_c^p}\frac{1}{1+\frac{\xi_{ab}^p}{l_{irr}}} = \gamma_0\frac{1}{1+\frac{\xi_{ab}^p}{l_{irr}}} \tag{5.12}$$

Thus the ratio of the anisotropy after and before heavy ion irradiation is:

$$\frac{\gamma}{\gamma_0} = \frac{1}{1+\frac{\xi_{ab}^{p}}{l_{irr}}} \tag{5.13}$$

The derivation of the anisotropy for a single band superconductor with columnar defects in the dirty limit has been given in Ref [68] and I simply put the results below:

$$\frac{\gamma}{\gamma_0} = \frac{1}{\sqrt{1+\frac{l_{ab}^{0}}{l_{irr}}}} \tag{5.14}$$

The irradiation induced change in the in-plane mean free path is proportional to the mean distance between columns, which is roughly $1/\sqrt{N_{col}}$ (N_{col} is the number of columns) for a classical two-dimensional system. Thus equation (5.13) and (5.14) can then be expressed as:

$$\frac{\gamma}{\gamma_0} = \frac{1}{1+\alpha\sqrt{N_{col}}} \quad \text{for} \quad l \gg \xi \tag{5.15}$$

$$\frac{\gamma}{\gamma_0} = \frac{1}{\sqrt{1+\alpha\sqrt{N_{col}}}} \quad \text{for} \quad l \ll \xi \tag{5.16}$$

where α is a phenomenological parameter. A plot of the anisotropy ratio with number of columnar defects is given in Fig 5.26. We can see that there is qualitative agreement between our data and this simple theoretical model.

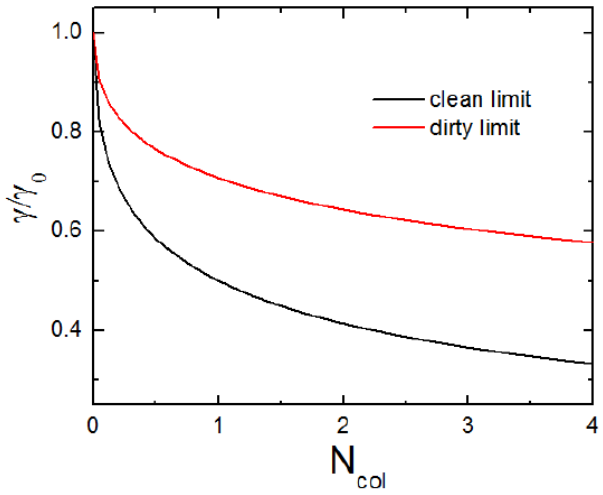

Fig 5.26 Anisotropy normalized by the value of the pristine sample as a function of the number of columnar defects in the clean (black) and dirty (red) limit.

In conclusion, we studied the effects of heavy ion irradiation on the anisotropy of optimum doped $YBa_2Cu_3O_{7-\delta}$ through angular rotational specific heat measurements. We found that after an irradiation dose of $B_\Phi = 6$ T in 1.4GeV Au heavy ion, the anisotropy of $YBa_2Cu_3O_{7-\delta}$ is reduced by approximately 50%. Similar reduction in the $B_\Phi = 1$ T $YBa_2Cu_3O_{7-\delta}$ sample has also been found. The observed dependence of the anisotropy on irradiation dose can be qualitatively explained by the simple theoretical model that takes into account the anisotropic scattering induced by columnar defects produced during heavy ion irradiation.

Chapter 6

Conclusions

In conclusion, I presented a systematic study of the phase transitions and thermodynamics of unconventional superconductors by high resolution membrane based AC micro-calorimetry.

Regarding the controversial "true" nematic phase transitions in $BaFe_2(As_{1-x}P_x)_2$ observed by magnetic torque measurements. We studied the specific heat of $BaFe_2(As_{1-x}P_x)_2$ at two doping levels: x=0 and x=0.3, which is the parent compound and a near-optimum doped compound. We observe a sharp peak in the specific heat at 133K and 137K for the as-grown and annealed parent compound $BaFe_2As_2$ which corresponds to the combined antiferromagnetic (AFM) and structural transition in this material. Entropy analysis of the parent compound reveal a first order like step at the AFM/Structural transition with a change in entropy of ~0.5 J/mol K. A kink about 0.5K above the step in entropy in annealed $BaFe_2As_2$ suggests splitting of the AFM and structural transition by about 0.5K. Careful analysis of the specific heat data for the annealed $BaFe_2As_2$ in the temperature region where torque measurments found the "true" nematic phase transition yields no evidence for another second order phase transition, even though the Ginzburg-Landau model used to fit the magnetic torque data indicates that the expected thermal anomaly should be easily observable with our experimental resolution of 10^{-4}. Similar lack of features has been observed in the specific heat of the near–optimum doped $BaFe_2(As_{0.7}P_{0.3})_2$ above the superconducting transition at 29K. We thus conclude that the behavior previously reported [61] for $BaFe_2As_2$ at T^* does not represent a 2^{nd} order phase transition, and that the phase transition into the orthorhombic phase does occur at T_S, the structural transition.

For the recently found reentrant C_4 symmetric AFM (SDW) phase in under doped $Ba_{1-x}Na_xFe_2As_2$ by high resolution neutron diffraction, we studied the thermodynamic phase transitions of four samples at three different doping levels: x=0.22, 0.26 and 0.28 with specific heat and SQUID magnetization measurements.

For the x=0.22 sample, a broadened step-like anomaly is found at around 18K with a width of ~ 2K that indicates the superconducting transition. The height of anomaly extracted by using an entropy conservation construction was found to be $\Delta C / T_c \approx 2.5 \text{mJ/mol K}^2$, which is about a factor of ten smaller than that of a similar sample in the "122" family with about the same T_c. We attribute this to the poor quality of the polycrystalline sample we have used for our measurements. Another peak in the specific heat at 98K and a step in the magnetization at the sample temperature signal the AFM (SDW) transition in this sample.

For the x=0.26 sample, in which the neutron diffraction experiment found the SDW transition between 80 and 85K and the reentrant C_4 SDW transition at ~ 45K, we were able to identify a kink in the specific heat and magnetization at around 45K. However, the lack of features at ~80 to 85K in both specific heat and magnetization data leaves doubt about the nature of the feature at 45K. Two scenarios can be possible: 1) the feature at 45K indeed marks the reentrant C_4 SDW transition and the lack of features for the C_2 SDW transition is caused by other factors, such as the quality of the sample; 2) the feature at 45K actually marks the C_2 SDW transition and there is not a reentrant C_4 SDW phase for $Ba_{1-x}Na_xFe_2As_2$ at this doping level. Further investigations on high quality single crystal samples would be very helpful in clarifying this issue. A small step like anomaly found at around 25K (onset) in specific heat and a drop in the magnetization at the same temperature indicates the superconducting transition in this sample. The anomaly height at the superconducting transition is estimated to be $\Delta C / T_c \approx 3.6 \text{mJ/mol K}^2$, which is slightly higher

than that of the x=0.22 sample but still much lower than the value of a single crystal sample with about the same T_c.

For the x=0.28 doping level, two samples were measured. For sample 1, a superconducting transition at 34K was found with a $\Delta C / T_c = 58 \text{mJ/mol K}^2$. The value of T_c is significantly higher than the literature value observed for doping level of x=0.28 (~25K) but rather is close to the T_c value of the optimum (x=0.4) doped $Ba_{1-x}Na_xFe_2As_2$. Measurements of the specific heat under various applied magnetic fields allow us to extract the value of the upper critical field slope near Tc as $\mu_0 dH_{c2} / dT = -6.5 \text{ T/K}$, which is quite close to the literature value of $\mu_0 dH_{c2}{}^{c} / dT = -5.25 \text{ T/K}$ for a single crystal $Ba_{1-x}Na_xFe_2As_2$ (x=0.4) sample for applied field along c-axis. The above evidence makes us believe that the sample 1 is actually at doping level of x=0.4 rather than x=0.28. For sample 2, we were able to distinguish two bumps in the specific heat at 29K and 34K respectively. The anomaly at 29K shifts in an applied field, giving evidence to its nature as another superconducting phase. The results from sample 2 lead us to the conclusion that the sample prepared at this doping level is not homogeneous and a range of doping's can be found from powder to powder.

The conclusion from our investigation of the emergent reentrant C_4 SDW phase transition in $Ba_{1-x}Na_xFe_2As_2$ is that there might be a reentrant C_4 phase in $Ba_{1-x}Na_xFe_2As_2$ at doping level of x=0.26. However, to make a firmer conclusion we would need to obtain a high quality single crystal for specific heat measurements. High quality samples for the whole range from x=0.24 to x=0.3 would be helpful for us to determine the exact phase boundaries of this emergent phase in the Temperature-doping phase diagram.

The effects of heavy ion irradiation on the thermodynamic anisotropy of YBCO are studied by field dependent and angular dependent specific heat measurements. For the pristine YBCO sample, anisotropy of 6.3 +/- 0.7 was extracted from the ratio of the upper critical field slopes

along the crystalline ab plane and c-axis. A Ginzburg-Landau model fit to the angular dependence of the upper critical temperature (T_{c2}) in a fixed applied field of 1T yields the anisotropy as a fitting parameter. The value of the anisotropy extracted from the fit is 7.8 +/- 2.0. The slight discrepancy between the anisotropy values from these two methods can be attributed to the slight misalignment of the magnetic field to the crystal orientations, which in our case was found to be around 2 degrees. Similar studies of the anisotropy of $YBa_2Cu_3O_{7-\delta}$ irradiated with 1.4GeV Au heavy ion at two different dose matching fields: $B_\Phi = 1\ \mathrm{T}$ and $B_\Phi = 6\ \mathrm{T}$ yields anisotropy of 4.3 +/- 1.4 for the $B_\Phi = 1\ \mathrm{T}$ $YBa_2Cu_3O_{7-\delta}$ sample and 3.7 +/- 1.5 for the $B_\Phi = 6\ \mathrm{T}$ $YBa_2Cu_3O_{7-\delta}$ sample respectively. Such a reduction in anisotropy can be qualitatively explained by a simple phenomenological model that takes into account the anisotropy scattering induced by columnar defects produced in heavy ion irradiation [68]. The theoretically derived dependence of anisotropy on the number of columnar defects agrees well with experimental data. More specifically, the anisotropy as predicted from the theoretical model does decrease fast with irradiation doses at first and then saturates at high irradiation doses.

Bibliography

[1] H. K. Onnes. The resistance of pure mercury at helium temperatures. *Commun. Phys. Lab. Univ. Leiden* **12**: 120 (1911).

[2] V. V. Schmidt. *The physics of superconductors: introduction to fundamentals and applications*, Springer-Verlag Berlin Heidelberg 1997

[3] https://nationalmaglab.org/education/magnet-academy/learn-the-basics/stories/superconductivity-101

[4] Superconductivity on Wikipedia, http://en.wikipedia.org/wiki/Superconductivity.

[5] Ni. Ni, Structural / magnetic phase transitions and superconductivity in $Ba(Fe_{1-x}TM_x)_2As_2$ single crystals, *Graduate Theses and Dissertations*, paper 10965 (2009).

[6] B. T. Matthias, T. H. Geballe, S. Geller, E. Corenzwit, Superconductivity of Nb_3Sn, *Phys. Rev.* **95** (6), 1435–1435 (1954).

[7] J. L. H. Lindenhovius, E. M. Hornsveld, A. den Ouden, W. A. J. Wessel, H. H. J. ten Kate, Powder-in-tube (PIT) Nb_3Sn conductors for high-field magnets, *Applied Superconductivity* **10** (1), 975–978 (2000).

[8] J. G. Bednorz and K. A. Muller, Possible High-T_c Superconductivity in the Ba-La-Cu-O System, *Z. Phys. B-Condens. Mat*. **64** (2), 189-193 (1986).

[9] M. K. Wu, J. R. Ashburn, and C. J. Torng, P. H. Hor, R. L. Meng, L. Gao, Z. J. Huang, Y. Q. Wang , and C. W. Chu, Superconductivity at 93 K in a new mixed-phase Y-Ba-Cu-O compound system at ambient pressure, *Phys. Rev. Lett.*, **58**, 908 (1987)

[10] Hiroshi Maeda, Yoshiaki Tanaka, Masao Fukutomi and Toshihisa Asano, A New High-*Tc* Oxide Superconductor without a Rare Earth Element, *Jpn. J. Appl. Phys.*, **27,** L209 (1988)

[11] Z. Z. Sheng, A. M. Hermann, Bulk superconductivity at 120 K in the Tl-Ca/Ba-Cu-O system, *Nature*, 332, 138 (1988)

[12] A. Schilling, M. Cantoni, J.D. Guo and H. R. Ott, Superconductivity above 130 K in the Hg-Ba-Ca-C-O system, *Nature*, 363, 56 (1993).

[13] P. Dai, B. C. Chakoumakos, G. F. Sun, K. W. Wong, Y. Xin and D. F. Lu, Synthesis and neutron powder diffraction study of the superconductor $HgBa_2Ca_2Cu_3O_{8+\delta}$ by Tl substitution, *Physica C*, 243, 201 (1995).

[14] Yoichi Kamihara, Takumi Watanabe, Masahiro Hirano, and Hideo Hosono, Iron-Based Layered Superconductor $LaO_{1-x}F_xFeAs$ (x = 0.05-0.12) with Tc = 26 K, J. Am. Chem. Soc., 130, 3296 (2008).

[15] Z.-A. Ren, W. Lu and J. Yang *et al.* Superconductivity at 55 K in iron-based F-doped layered quaternary compound $SmO_{1-x}F_xFeAs$. *Chin. Phys. Lett.* **25**: 2215 (2008).

[16] C. Wang, L. Li and S. Chi *et al*. Thorium-doping-induced superconductivity up to 56 K in $Gd_{1-x}Th_xFeAsO$. *Europhys. Lett.* 83: 67006 (2008).

[17] J. Paglione and R. L. Greene, High-temperature superconductivity in iron-based materials, *Nat. Phys.* 6, 645 (2010)

[18] M. Rotter, M. Pangerl, M. Tegel & D. Johrendt, Superconductivity and crystal structures of $(Ba_{1-x}K_x)Fe_2As_2$ (x = 0 - 1). *Angew. Chem. Int. Ed.* 47, 7949-7952 (2008).

[19] N. Ni *et al*. Effects of Co substitution on thermodynamic and transport properties and anisotropic H_{c2} in $Ba(Fe_{1-x}Co_x)_2As_2$ single crystals. *Phys. Rev. B.* 78, 214515 (2008).

[20] S. Jiang *et al*. Superconductivity up to 30 K in the vicinity of the quantum critical point in $BaFe_2(As_{1-x}P_x)_2$. *J. Phys. Condens. Matter*. 21, 382203 (2009).

[21] P. L. Alireza *et al*. Superconductivity up to 29 K in $SrFe_2As_2$ and $BaFe_2As_2$ at high pressures. *J. Phys. Condens. Matter.* 21, 012208 (2009).

[22] E. Colombier, S. L. Bud'ko, N. Ni and P. C. Canfield, Complete pressure-dependent phase diagrams for $SrFe_2As_2$ and $BaFe_2As_2$. *Phys. Rev. B.* 79, 224518 (2009).

[23] F. Ishikawa *et al*. Zero-resistance superconducting phase in $BaFe_2As_2$ under high pressure. *Phys. Rev. B.* 79, 172506 (2009).

[24] H. Fukazawa *et al*. Suppression of magnetic order by pressure in $BaFe_2As_2$. *J. Phys. Soc. Jpn*. 77, 105004 (2008).

[25] K. Matsubayashi *et al*. Intrinsic properties of AFe_2As_2 (A = Ba, Sr) single crystal under highly hydrostatic pressure conditions. *J. Phys. Soc. Jpn.* 78, 073706 (2009).

[26] D. J. Singh, Electronic structure of Fe-based superconductors. *Physica C* 469, 418-424 (2009).

[27] I. I. Mazin and J. Schmalian, Pairing symmetry and pairing state in ferropnictides: Theoretical overview. *Physica C* 469, 614-623 (2009).

[28] D. H. Lu *et al*. Electronic structure of the iron-based superconductor LaOFeP. *Nature* 455, 81-84 (2008).

[29] T. Kondo *et al*. Momentum dependence of the superconducting gap in $NdFeAsO_{0.9}F_{0.1}$ single crystals measured by angle resolved photoemission spectroscopy. *Phys. Rev. Lett.* 101, 147003 (2008).

[30] H. Ding *et al*. Observation of Fermi-surface-dependent nodeless superconducting gaps in $Ba_{0.6}K_{0.4}Fe_2As_2$. *Europhys. Lett.* 83, 47001 (2008).

[31] H. Shishido *et al*. Evolution of the Fermi surface of $BaFe_2(As_{1-x}P_x)_2$ on entering the superconducting dome. *Phys. Rev. Lett.* 104, 057008 (2010).

[32] N. Harrison *et al*. Quantum oscillations in antiferromagnetic $CaFe_2As_2$ on the brink of superconductivity. *J. Phys. Condens. Matter* 21, 32220 (2009).

[33] I. I. Mazin, D. J. Singh, M. D. Johannes, M. H. Du, Unconventional superconductivity with a sign reversal in the order parameter of $LaFeAsO_{1-x}F_x$. *Phys. Rev. Lett.* 101, 057003 (2008).

[34] K. Matano *et al*, Spin-singlet superconductivity with multiple gaps in $PrFeAsO_{0.89}F_{0.11}$, *Europhys. Lett.* 83, 57001 (2008)

[35] Y. Nakai *et al*, Evolution from Itinerant Antiferromagnet to Unconventional Superconductor with Fluorine Doping in $LaFeAs(O_{1-x}F_x)$ Revealed by ^{75}As and ^{139}La Nuclear Magnetic Resonance, *J. Phys. Soc. Jpn.* 77, 073701 (2008)

[36] S. Graser, T. A. Maier, P. J. Hirschfeld and D. J. Scalapino, Near-degeneracy of several pairing channels in multiorbital models for the Fe pnictides. *New J. Phys.* 11, 025016 (2009).

[37] C. W. Hicks *et al*. Limits on the superconducting order parameter in $NdFeAsO_{1-x}F_y$ from scanning SQUID microscopy. *J. Phys. Soc. Jpn*. 78, 013708 (2009).

[38] X. Zhang *et al*. Observation of the Josephson effect in $Pb/Ba_{1-x}K_xFe_2As_2$ single crystal junctions. *Phys. Rev. Lett.* 102, 147002 (2009).

[39] L. Boeri, M. Calandra, I. I. Mazin, O.V. Dolgov and F. Mauri, Effects of magnetism and doping on the electron-phonon coupling in $BaFe_2As_2$. *Phys. Rev. B* 82, 020506(R) (2010).

[40] C. de la Cruz et al, Magnetic order close to superconductivity in the iron-based layered $LaO_{1-x}F_xFeAs$ systems, *Nature* 453, 899 (2008).

[41] S. Avci *et al*, Magnetoelastic coupling in the phase diagram of $Ba_{1-x}K_xFe_2As_2$ as seen via neutron diffraction, *Phys. Rev. B* 83 172503 (2011).

[42] J.-H. Chu, J. G. Analytis, C. Kucharczyk, and I. R. Fisher, Determination of the phase diagram of the electron-doped superconductor $Ba(Fe_{1-x}Co_x)_2As_2$, *Phys. Rev. B* 79, 014506 (2009).

[43] H.-H. Kuo, Electronic Nematicity in Iron-Based Superconductors, *Thesis submitted to Stanford University Graduate School* (2014).

[44] R. M. Fernandes, A. V. Chubukov, and J. Schmalian, What drives nematic order in iron-based superconductors? *Nature Physics* 10, 97 (2014).

[45] J.-H. Chu, J.G. Analytis, K. De Greve, P.L. McMahon, Z. Islam, Y. Yamamoto and I. R. Fisher, In-Plane Resistivity Anisotropy in an Underdoped Iron Arsenide Superconductor, *Science* 329, 824826 (2010).

[46] J.-H. Chu, H.-H. Kuo, J. G. Analytis and I. R. Fisher, Divergent Nematic Susceptibility in an Iron Arsenide Superconductor, *Science* 337, 710 (2012).

[47] A. Dusza, A. Lucarelli, F. Pfuner, J.-H. Chu, I. R. Fisher, and L. Degiorgi, Anisotropic charge dynamics in detwinned $Ba(Fe_{1-x}Co_x)_2As_2$, *Europhys. Lett* 93, 37002 (2011).

[48] M, Yi *et al*, Symmetry-breaking orbital anisotropy observed for detwinned $Ba(Fe_{1-x}Co_x)_2As_2$ above the spin density wave transition, *Proc. Natl. Acad. Sci* 108, 6878 (2011).

[49] C.-C. Lee, W.-G. Yin and W. Ku, Ferro-Orbital Order and Strong Magnetic Anisotropy in the Parent Compounds of Iron-Pnictide Superconductors, *Phys. Rev. Lett* 103, 267001 (2009).

[50] W. Lv, J. Wu, and P. Phillips, Orbital ordering induces structural phase transition and the resistivity anomaly in iron pnictides, *Phys. Rev. B* 80, 224506 (2009).

[51] C.-C. Chen, J. Maciejko, A. P. Sorini, B. Moritz, R. R. P. Singh and T. P. Devereaux, Orbital order and spontaneous orthorhombicity in iron pnictides, *Phys. Rev. B* 82, 100504 (2010).

[52] C.-C. Chen, B. Moritz, J. van den Brink, T. P. Devereaux and R. R. P. Singh, Finite-temperature spin dynamics and phase transitions in spin-orbital models, *Phys. Rev. B* 80, 180418 (R) (2009).

[53] V. Stanev and P. B. Littlewood, Nematicity driven by hybridization in iron-based superconductors, *Phys. Rev. B* 87, 161122(R) (2013).

[54] C. Xu, M. Muller and S. Sachdev, Ising and spin orders in the iron-based superconductors, *Phys. Rev. B* 78 020501(R) (2008).

[55] C. Fang, H. Yao, W.-F. Tsai, J. P. Hu and S. A. Kivelson, Theory of electron nematic order in LaFeAsO, *Phys. Rev. B* 77, 224509 (2008).

[56] R. M. Fernandes, A.V. Chubukov, J. Knolle, I. Eremin and J. Schmalian, Preemptive nematic order, pseudogap, and orbital order in the iron pnictides, *Phys. Rev. B* 85, 024534 (2012).

[57] R. M. Fernandes and J. Schmalian, Manifestations of nematic degrees of freedom in the magnetic, elastic, and superconducting properties of the iron pnictides, *Supercond. Sci. Technol*. 25, 084005 (2012).

[58] S. Avci, O. Chmaissem, J. M. Allred, S. Rosenkranz, I. Eremin, A. V. Chubukov, D. E. Bugaris, D. Y. Chung, M. G. Kanatzidis, J.-P. Castellan, J. A. Schlueter, H. Claus, D. D. Khalyavin, P. Manuel, A. Daoud-Aladine, and R. Osborn, Magnetically driven suppression of nematic order in an iron-based superconductor, *Nature Commun*. 5, 3845 (2014).

[59] M. G. Kim, R. M. Fernandes, A. Kreyssig, J. W. Kim, A. Thaler, S. L. Bud'ko, P. C. Canfield, R. J. McQueeney, J. Schmalian, and A. I. Goldman, Character of the structural and magnetic phase transitions in the parent and electron-doped BaFe2As2 compounds, *Phys. Rev. B* 83, 134522 (2011).

[60] A. Cano, M. Civelli, I. Eremin, I. Paul, Interplay of magnetic and structural transitions in iron-based pnictide superconductors, *Phys. Rev. B* 82, 020408(R) (2010).

[61] S. Kasahara, H. J. Shi, K. Hashimoto, S. Tonegawa, Y. Mizukami, T. Shibauchi, K. Sugimoto, T. Fukuda, T. Terashima, A. H. Nevidomskyy and Y. Matsuda, Electronic nematicity above the structural and superconducting transition in $BaFe_2(As_{1-x}P_x)_2$, *Nature* 486, 382 (2012).

[62] X. F. Xu, W. H. Jiao, N. Zhou, Y. K. Li, B. Chen, C. Cao, J. H. Dai, A. F. Bangura, G. Cao, Electronic nematicity revealed by torque magnetometry in $EuFe_2(As_{1-x}P_x)_2$, *Phys. Rev. B* 89, 104517 (2014).

[63] S. H. Liang, A. Moreo, E. Dagotto, Nematic State of Pnictides Stabilized by Interplay between Spin, Orbital, and Lattice Degrees of Freedom, *Phys. Rev. Lett.* 111, 047004 (2013).

[64] A. E. Böhmer *et al*, Nematic Susceptibility of Hole-Doped and Electron-Doped $BaFe_2As_2$ Iron-Based Superconductors from Shear Modulus Measurements, *Phys. Rev. Lett.* 112, 047001 (2014).

[65] E. P. Rosenthal *et al*, Visualization of electron nematicity and unidirectional antiferroic fluctuations at high temperatures in NaFeAs, *Nature Physics*, 10, 225232 (2014).

[66] X. G. Lu *et al*, Nematic spin correlations in the tetragonal state of uniaxial-strained $BaFe_{2-x}Ni_xAs_2$, *Science* 345, 657 (2014).

[67] S. Avci *et al*, Magnetically driven suppression of nematic order in an iron-based superconductor, *Nat. Commun.*5, 3845 (2014).

[68] L. Fang *et al*, Huge critical current density and tailored superconducting anisotropy in $SmFeAsO_{0.8}F_{0.15}$ by low-density columnar-defect incorporation, *Nat. Comm* 4, 2655 (2013).

[69] S. Yeninas *et al*, Upper critical field of isoelectron substituted $SrFe_2(As_{1-x}P_x)_2$, *Phys. Rev. B* 87, 094503 (2013)

[70] L. Fang *et al*, High, magnetic field independent critical currents in $(Ba,K)Fe_2As_2$ crystals, *Appl. Phys. Lett.* 101, 012601 (2012)

[71] J.-L. Zhang, L. Jiao, Y. Chen, H.-Q. Yuan, Universal behavior of the upper critical field in iron-based superconductors, *Front. Phys*, 6(4), 463–473 (2011)

[72] W. Meissner, R. Ochsenfeld: *Naturwiss*. 21, 787 (1933).

[73] U. Gottlieb, J. C. Lasjaunias, J. L. Tholence, O. Laborde, O. Thomas, R. Madar, Superconductivity in $TaSi_2$ single crystals, *Phys. Rev. B* 45, 4803 (1992).

[74] L.D. Landau, *Electrodynamics of Continuous Media* 8. Butterworth-Heinemann (1984).

[75] A. A. Abrikosov, *Zh. Eksp. Teor. Fiz.* 32, 1442 (1957) [English trasl.: *Sov. Phys. JETP* 5, 1174 (1957)]

[76] F. London, H. London, The Electromagnetic Equations of the Supraconductor. *Proceedings of the Royal Society A* 149 (866): 71 (1935).

[77] V.L.Ginzburg and L.D.Landau, *Zh. Eksperim. I. Teor. Fiz.* 20, 1064 (1950)

[78] M. Tinkham. *Introduction to superconductivity*. McGraw-Hill, New York, second edition, 1996.

[79] L. N. Cooper, Bound Electron Pairs in a Degenerate Fermi Gas, *Phys. Rev.*, 104, 1189 (1956).

[80] J. Bardeen, L. N. Cooper, and J. R. Schrieffer, Microscopic Theory of Superconductivity, *Phys. Rev.*, 106, 162 (1957).

[81] J. Bardeen, L. N. Cooper, and J. R. Schrieffer, Theory of Superconductivity, *Phys. Rev.*, 108, 1175 (1957)

[82] Emanuel Maxwell, Isotope Effect in the Superconductivity of Mercury, *Phys. Rev.*, 78, 477 (1950)

[83] C. A. Reynolds, B. Serin, W. H. Wright, and L. B. Nesbitt, Superconductivity of Isotopes of Mercury, *Phys. Rev.*, 78, 487 (1950)

[84] H. Frohlich, Interaction of Electrons with Lattice Vibrations, *Proc. R. Soc. Lond. A*, 215, 291 (1952)

[85] K. H. Bennemann and J. B. Ketterson, *Superconductivity: Volume 1, Conventional and unconventional superconductors*, edited by K. H. Bennemann and J. B. Ketterson (Springer) (2008)

[86] L. P. Gor'kov, Microscopic derivation of the Ginzburg-Landau equations in the theory of superconductivity, *Zh. Eksp. Teor. Fiz.*, 36, 1918 (1959); *Sov. Phys. JETP*, 9, 1364 (1959)

[87] P. Chandra, P. Coleman, and A. I. Larkin, Ising transition in frustrated Heisenberg models, *Phys. Rev. Lett.* 64, 88 (1990)

[88] Q. Si and E. Abrahams, Strong Correlations and Magnetic Frustration in the High T_c Iron Pnictides, *Phys. Rev. Lett.* 101, 076401 (2008)

[89] N. W. Ashcroft and N. D. Mermin, *Solid State Physics*, Thomson Learning, 1976

[90] A. Schilling, R. A. Fisher, N. E. Phillips, U. Welp, W. K. Kwok, and G. W. Crabtree, Anisotropic Latent Heat of Vortex-Lattice Melting in Untwinned $YBa_2Cu_3O_{7-\delta}$, *Phys. Rev. Lett.* 78, 4833 (1997)

[91] J.-P. Castellan, S. Rosenkranz, R. Osborn, Q. Li, K. E. Gray, X. Luo, U. Welp, G. Karapetrov, J. P. C. Ruff, and J. van Wezel, Chiral Phase Transition in Charge Ordered *1T*−$TiSe_2$, *Phys. Rev. Lett*. 110, 196404 (2013)

[92] F. Bouquet, Y. Wang, R. A. Fisher, D. G. Hinks, J. D. Jorgensen, A. Junod and N. E. Phillips, Phenomenological two-gap model for the specific heat of MgB_2, *Europhys. Lett.* 56 856 (2001)

[93] S. Tagliati, Development and characterization of a membrane-based nanocalorimeter for low temperatures, *Thesis submitted to Stockholm University*, 2010

[94] E. Gmelin, Modern low temperature calorimetry, *Thermochi. Acta* 29, 1 (1979).

[95] http://www.netzsch-thermal-analysis.com/de/homepage/general.html

[96] O. M. Corbino, *Phys. Z.* 12, 292 (1911)

[97] N. Birge and S. Nagel, Wide-frequency specific-heat spectrometer, *Rev. Sci. Intrum.* 58, 1464 (1987).

[98] P. F. Sullivan and G. Seidel, Steady-state, ac-temperature calorimetry, *Phys. Rev.* 173 (3), 679 (1968).

[99] P. Sullivan and G. Seidel, A.C. temperature measurement of changes in heat capacity of beryllium in a magnetic field, *Phys. Lett. A* 25A (3), 229 (1967).

[100] Y. A. Kraftmakher and P. G. Strelkov, The energy of formation and the density of vacancies in tungsten, *Sov. Phys.-Solid State* 4 (8), 2271-2274 (1962).

[101] P. Handler, D. E. Mapother, and M. Rayl, AC measurement of the heat capacity of nickel near its critical point, *Phys. Rev. Lett.* 19 (7), 356-358 (1967).

[102] C. Chaparro, Micro-Calorimetric Study of Iron-Based Superconductor $BaFe_2(As_{1-x}P_x)_2$, *Thesis submitted to University of Notre Dame*, 2013

[103] A. Rydh, U. Welp, and W. K. Kwok, Proposal: Ultra High-Sensitive Miniature Calorimeter for Studies of Confinement Effects of Bio-Organic Structures, (2003-2006).

[104] R. Xie, Transformation of a three dimensional first order vortex matter transition with induced disorder, *Thesis submitted to University of Notre Dame*, 2008.

[105] T. H. Geballe and W. Giauque, The heat capacity and entropy of gold from 15 to 300 degrees K, *J. Am. Chem. Soc.* 74, 2368-2369 (1952).

[106] S. Tagliati, V. M. Krasnov, and A. Rydh, Differential membrane-based nanocalorimeter for high-resolution measurements of low-temperature specific heat, *Rev. Sci. Instrum.* 83, 055107 (2012)

[107] L. Shan, Y.-L. Wang, B. Shen, B. Zeng, Y. Huang, A. Li, D. Wang, H. Yang, C. Ren, Q.-H. Wang, S. H. Pan and H.-H. Wen, Observation of ordered vortices with Andreev bound states in $Ba_{0.6}K_{0.4}Fe_2As_2$, *Nature Physics* 7, 325331 (2011).

[108] S. Ishida, T. Liang, M. Nakajima, K. Kihou, C. H. Lee, A. Iyo, H. Eisaki, T. Kakeshita, T. Kida, M. Hagiwara, Y.Tomioka, T. Ito, and S. Uchida, Manifestations of multiple-carrier charge transport in the magnetostructurally ordered phase of $BaFe_2As_2$, *Phys. Rev. B* 84, 184514 (2011).

[109] C. R. Rotundu, B. Freelon, T. R. Forrest, S. D. Wilson, P. N. Valdivia, G. Pinuellas, A. Kim, J.-W. Kim, Z. Islam, E. Bourret-Courchesne, N.E. Philips and R. J. Birgeneau, Heat capacity study of $BaFe_2As_2$: Effects of annealing, *Phys. Rev. B* 82, 144525 (2010).

[110] C. R. Rotundu and R. J. Birgeneau, First- and second-order magnetic and structural transitions in $BaFe_{2(1-x)}Co_{2x}As_2$, *Phys. Rev. B* 84, 092501 (2011).

[111] A. Junod *et al*, A study of the magnetic transitions in CuO: specific heat (1-330 K), magnetic susceptibility and phonon density of states, *J. Phys.: Condens. Matter* 1, 8021 (1989).

[112] L. J. de Jongh, and A. R. Miedema, Experiments on simple magnetic model systems, *Advances in Physics* 23, 1 (1974).

[113] J.-H. Chu, J. G. Analytis, D. Press, K. De Greve, T. D. Ladd, Y. Yamamoto and I. R. Fisher, In-plane electronic anisotropy in underdoped $Ba(Fe_{1-x}Co_x)_2As_2$ revealed by partial detwinning in a magnetic field, *Phys. Rev. B.* 81, 214502 (2010).

[114] J. P. C. Ruff, J.-H. Chu, H.-H. Kuo, R. K. Das, H. Nojiri, I. R. Fisher and Z. Islam, Susceptibility Anisotropy in an Iron Arsenide Superconductor Revealed by X-Ray Diffraction in Pulsed Magnetic Fields, *Phys. Rev. Lett*. 109, 027004 (2012).

[115] For annealed $BaFe_2As_2$, a Curie-type paramagnetic background, possibly coming from precipitates of Fe or Fe related compound introduced during annealing, was subtracted. Similar background subtraction was also done on the magnetization of as grown $BaFe_2As_2$, although the magnitude of the background is almost negligible.

[116] X. F. Wang, T. Wu, G. Wu, H. Chen, Y. L. Xie, J. J. Ying, Y. J. Yan, R. H. Liu and X. H. Chen, Anisotropy in the Electrical Resistivity and Susceptibility of Superconducting $BaFe_2As_2$ Single Crystals, *Phys. Rev. Lett.*, 102 117005 (2009).

[117] F. Ronning, T. Klimczuk, E. D. Bauer, H. Volz, and J. D. Thompson, Synthesis and properties of $CaFe_2As_2$ single crystals, *J. Phys.: Condens. Matter* 20, 322201 (2008).

[118] R. Klingeler *et al*, Local antiferromagnetic correlations in the iron pnictide superconductors $LaFeAsO_{1-x}F_x$ and $Ca(Fe_{1-x}Co_x)_2As_2$ as seen via normal-state susceptibility, *Phys. Rev. B* 81, 024506 (2010).

[119] J.-Q. Yan *et al*, Structural transition and anisotropic properties of single-crystalline $SrFe_2As_2$, *Phys. Rev. B* 78, 024516 (2008).

[120] D. C. Johnston, Magnetic Susceptibility Scaling in $La_{2-x}Sr_xCuO_{4-y}$, *Phys. Rev. Lett.* 62, 957 (1989).

[121] G. M. Zhang, Y. H. Su, Z. Y. Lu, Z. Y. Weng, D. H. Lee and T. Xiang, Universal linear-temperature dependence of static magnetic susceptibility in iron pnictides, *Europhys. Lett*, 86 37006 (2009).

[122] M. M. Korshunov, I. Eremin, D. V. Efremov, D. L. Maslov, and A. V. Chubukov, Nonanalytic Spin Susceptibility of a Fermi Liquid: The Case of Fe-Based Pnictides, *Phys. Rev. Lett.* 102, 236403 (2009).

[123] S. L. Skornyakov, A. A. Katanin, and V. I. Anisimov, Linear-Temperature Dependence of Static Magnetic Susceptibility in LaFeAsO from Dynamical Mean-Field Theory, *Phys. Rev. Lett.* 106, 047007 (2011).

[124] R. M. Fernandes, A. E. Böhmer, C. Meingast and J. Schmalian, Scaling between Magnetic and Lattice Fluctuations in Iron Pnictide Superconductors, *Phys. Rev. Lett.* 111, 137001 (2013)

[125] C. Chaparro, L. Fang, H. Claus, A. Rydh, G. W. Crabtree, V. Stanev, W. K. Kwok, and U. Welp, Doping dependence of the specific heat of single-crystal $BaFe_2(As_{1-x}P_x)_2$, *Phys. Rev. B* 85, 184525 (2012)

[126] A. E. Böhmer, F. Hardy, L. Wang, T. Wolf, P. Schweiss, C. Meingast, Superconductivity-induced reentrance of orthorhombic distortion in $Ba_{1-x}K_xFe_2As_2$, arXiv: 1412.7038 (2014)

[127] S. Aswartham *et al*, Hole doping in $BaFe_2As_2$: The case of $Ba_{1-x}Na_xFe_2As_2$ single crystals, *Phys. Rev. B* 85, 224520 (2012)

[128] L. Civale, Vortex pinning and creep in high-temperature superconductors with columnar defects, *Supercond. Sci. Technol.* 10, A11–A28 (1997)

[129] L. Civale, A. D. Marwick, T. K. Worthington, M. A. Kirk, J. R. Thompson, L. Krusin-Elbaum, Y. Sun, J. R. Clem and F. Holtzberg, Vortex confinement by columnar defects in $YBa_2Cu_3O_7$ crystals: Enhanced pinning at high fields and temperatures, *Phys. Rev. Lett.* 67, 648 (1991)

[130] L. Civale and L. Krusin-Elbaum, Comment on "Upper Limit of the Bose-Glass Transition in YBa2Cu3O7 at High Density of Columnar Defects", *Phys. Rev. Lett.* 78, 1829 (1997)

[131] U. Welp, R. Xie, A. E. Koshelev, W. K. Kwok, H. Q. Luo, Z. S. Wang, G. Mu, and H. H. Wen, Anisotropic phase diagram and strong coupling effects in $Ba_{1-x}K_xFe_2As_2$ from specific-heat measurements, *Phys. Rev. B* 79, 094505 (2009).